Silicon Photonics Building Blocks for PDM-MDM Optical Interconnects

Heming Xu

Department of Electrical & Computer Engineering

McGill University

Montréal, Québec, Canada

December, 2022

A thesis submitted to McGill University in partial fulfillment of the requirements of the degree of

Master of Science

Abstract

Silicon Photonics (SiPh) technology has been used to address the challenges of optical interconnection in integrated photonic circuits for over a decade. Its application has gradually expanded to the fields of communications and data centers. Compared with traditional complementary metal-oxide-semiconductor (CMOS), SiPh technology not only retains the characteristics of small size, low power consumption, low cost, and high integrations in microelectronics, but also integrates multi-channel, large bandwidth, high speed, and high integration from optoelectronics. Advanced modulation formats combined with various multiplexing techniques are extensively used in current fiber optic communications to meet the rapidly growing demands of transmission capacities of optical networks. Indeed, the transmission capacity has increased by using multiple multiplexing techniques including wavelength division multiplexing (WDM), mode division multiplexing (MDM), and polarization division multiplexing (PDM). Consequently, the building blocks for optical interconnects utilizing these multiplexing technologies are necessary to handle multiple wavelengths, modes, and polarizations.

This thesis provides a comprehensive study of MDM-PDM interconnects in SiPh technologies. Several state-of-the-art building blocks of the MDM-PDM interconnect have been developed over the recent years such as mode multiplexers, phase shifters, and optical switches, as well as polarization beam splitters and polarization filters. We first analyze different MDM-PDM systems in SiPh exploiting two multiplexing technologies. This thesis then theoretically and experimentally demonstrates a PDM-MDM 3-dB coupler for optical power splitting/combining. This 3-dB coupler works for the first two transverse electric (TE) modes and the first two transverse magnetic (TM) modes. Over an optical bandwidth of 70 nm (1500 nm to 1570 nm), the coupler exhibits at most 0.7 dB insertion loss with a maximum crosstalk of -15.7 dB and a power imbalance not worse than 0.9 dB. As a potential application for the 3-dB coupler, a multimode photonic space switch matrix is proposed simultaneously exploiting WDM, PDM, and MDM. Based on the experimental measurements of the 3-dB coupler and the proposed application, the switching loss is estimated to be 6.0 dB with crosstalk mainly limited by the MDM (de)multiplexing circuit. Another optical mode switch for eight modes is also proposed by combining MDM and PDM techniques. The switching topology provides more data channels and 24 combination possibilities for transmission and consists of six Y-branch structures and six phase shifters. According to simulation results, the eight-mode switch has considerable insertion loss estimated to be 15.5 dB (1500 nm to 1600 nm).

Sommaire

La technologie photonique sur silicium (SiPh) est utilisée dans les interconnexions optiques depuis plus d'une décennie. Elle s'étend aux domaines des communications et des centres de données. Par rapport au métal-oxyde-semi-conducteur complémentaire (CMOS) traditionnel, la technologie SiPh conserve non seulement les caractéristiques de petite taille, de faible consommation d'énergie, de faible coût et d'intégration élevée en microélectronique, mais intègre également multiple canaux, une large bande passante, une haute vitesse et une haute intégration de l'optoélectronique. Pour répondre aux demandes croissantes de capacités de transmission des réseaux optiques, les formats de modulation avancés combinés à diverses techniques de multiplexage sont largement utilisés dans les communications actuelles par fibre optique. La capacité de transmission a été mise à jour de plus en plus en utilisant plusieurs techniques de multiplexage, notamment le multiplexage par répartition en longueur d'onde (WDM), le multiplexage par répartition en mode (MDM) et le multiplexage par répartition en polarisation (PDM). Par conséquent, les blocs pour les interconnexions optiques utilisant ces technologies de multiplexage sont nécessaires pour gérer plusieurs longueurs d'onde, modes et polarisations.

Dans cette thèse, une étude approfondie de la revue de la littérature sur l'interconnexion MDM-PDM est fournie. En outre, nous avons analysé l'état de l'art des éléments constitutifs de l'interconnexion MDM-PDM, tels que le multiplexeur de mode, le déphaseur et le commutateur optique dans le système MDM, ainsi que les séparateurs de faisceau de polarisation et les filtres de polarisation dans le système PDM. Les structures des systèmes MDM-PDM combinant deux technologies de multiplexage sont également analysées. Cette thèse démontre théoriquement et expérimentalement un coupleur PDM-MDM 3-dB pour la séparation et la combinaison de puissance optique. Ce coupleur de 3 dB fonctionne pour les deux premiers modes transversaux électriques (TE) et les deux premiers modes transversaux magnétiques (TM). Sur une bande passante optique de 70 nm (1500 nm à 1570 nm), le coupleur présente au plus 0,7 dB de perte d'insertion avec une diaphonie maximale de -15,7 dB et un déséquilibre de puissance ne dépassant pas 0,9 dB. Pour une application ultérieure de ce coupleur 3-dB, une matrice de commutation spatiale photonique multimode est proposée exploitant simultanément le multiplexage par répartition en longueur d'onde (WDM), le multiplexage par répartition en polarisation (PDM) et le multiplexage par répartition en mode (MDM). Sur la base des mesures expérimentales du coupleur de 3 dB et du système MDM correspondant, la perte de commutation est estimée à 6,0 dB avec une diaphonie limitée par le circuit de (dé)multiplexage MDM. De plus, un autre commutateur de mode optique pour huit modes est également démontré en combinant les techniques MDM et PDM. Cette structure offre plus de canaux de données et 24 possibilités de combinaison pour la transmission. Selon les résultats de la simulation, le commutateur à huit modes a une taille plus intégrée mais une plus grande perte d'insertion qui est estimée à 15,5 dB dans une bande passante plus large

(1500 nm à 1600 nm).

Acknowledgments

It has been such a long journey, and after enduring great hardship, I have finally presented this thesis here. My deepest and sincerest gratitude goes to my supervisor, Prof. Odile Liboiron-ladouceur, for funding me to be part of this fantastic research group. She always supports me in focusing on my interested field, respects my ideas and gives me practical guidance to improve my knowledge and research abilities. Besides, she gives me many opportunities to exercise my presentation and speech skills. It is her encouragement that helped me become confident in expressing myself. She shares her understanding and future direction of my research with me and is very patient in helping me with paper revisions and guidance. Her patience, constant support and encouragement became the primary motivation for me to complete my master's degree.

All the members in McGill's Photonic Systems Groups are gentle, kind, and energetic. Two years' experience here is warm and memorable. Together we struggled, supported each other, and moved forward with new challenges. I appreciate everyone in the Photonic Datacom team: Dusan Gostimirovic, Shanglin Li, José Garcia Echeverria, Ajaypal Singh Dhillon, S. Mohammad Reza Safaee A., Rifat Nazneen, Sunami Morrison, Rebecca Rogers, Hasan Houji and Md Mahadi Masnad. We explore amazing ideas, progress together, and encourage each other to face all the difficulties. Special thanks to Hassan Rahbardar Mojaver, Rebecca Roger and Guowu Zhang for their enormous support and great contribution. Hassan

Rahbardar Mojaver provided lots of guidance during my experiment and suggested me how to write a comprehensive and organized paper. Rebecca Rogers patiently and meticulously helped me revise this thesis's presentation and grammar. Guowu Zhang was always there throughout my whole master's studies, sharing his experience and giving guidance during my simulation and experiment work. Besides, he helped me improve my analytical skills by explaining the logic behind the problem and increased my confidence by walking me through the challenges I encountered.

I am very grateful to my parents. They support me to pursue my targets unconditionally. They have been of incredible love and caring for me.

I also want to express my gratitude to my academic peers and friends. We had a beautiful time together. They witnessed my laughter and tears. These include Yu Wu, Weijia Li, Yixiang Hu, Zixian Wei, Deng Mao, Jinsong Zhang, Linwei Yuan, Dan Jiang, Jingyi Xi, Sijie Chen, Chao Yao, Xinwei Tong, Yizhen Pan.

Finally, to all of the above: we will all have bright futures, in various ways.

Contents

List of Figures

List of Tables

List of Acronyms

ADC Adiabatic Couplers

ANT Applied Nanotools

BPM Beam Porpagation Method

CMOS Complementary Metal-Oxide Semiconductor

CPU Computer Processing Units

CWDM Coarse Wavelength Division Multiplexing

DC Directional Coupler

DGD Differential Group Delay

EBL Electron Beam Lithography

EIM Equivalent Refractive Index Method

EME Eigenmode Expansion Method

FDM Finite Difference Method

FDTD Finite Difference Time Domain

FEM Finite Element Method

FOG Fiber Optic Gyroscope

FSR Free Spectral Range

GaAs Gallium Arsenide

GC Grating Coupler

ICP-RIE Inductively Coupled Plasma - Induced Reactive Ion Etching

IL Insertion Loss

IP Internet Protocol

LNOI Lithium Niobate On Insulator

LS Laser Diode

MB Multichannel Branching

M2M Machine To Machine

MDM Mode Division Multiplexing

MMI Mutlimode Interference

MRR MicroRing Resonator

Mux Mutliplexer

MWG Multimode Waveguide Grating

MZI Mach-Zehnder Interferometer

PBC Polarization Beam Controller

PBS Polarization Beam Splitter

PDL Polarization Dependent Loss

PDM Polarization Division Multiplexing

PECVD Plasma-Enhanced Chemical Vapor Deposition

PIC Photonics Integrated Circuits

PIOF Polarization Insensitive Optical Filters

PR Polarization Rotator

PRBG Polarization Rotating Bragg Grating

PS Power Splitter

SiPh Silicon Photonics

SOI Silicon On Insulator

SWG Subwavelength Grating

TE Transverse Electric

TiW Titanium-Tungsten

TM Transverse Magnetic

VCSEL Vertical Cavity-Surface-Emitting Lase

WC Waveguide Crossing

WDM Wavelength Division Multiplexing

XT Crosstalk

Chapter 1

Introduction

Internet traffic is one of the key metrics used in telecommunications systems such as data centers and high-performance computing. Internet Protocol (IP) traffic is often used to measure the amount of data sent over the Internet [1]. In Fig. 1.1, the IP traffic application is illustrated. M2M (Machine to Machine) communication is forecasted to be the prominent area for continued technological advancements. Fig. 1.2 shows the global mobile data traffic forcasted by ITU (International Telecommunication Union).

With applications such as artificial intelligence, data centers are also moving towards data interconnection based on optical communication [4]. The main reason is that applications

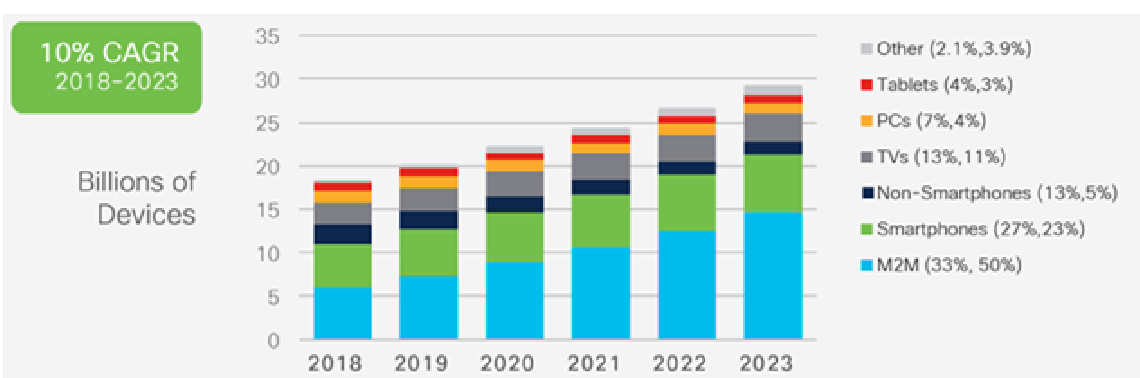

Fig. 1.1: IP traffic application (2018-2023) from Cisco annual report [2].

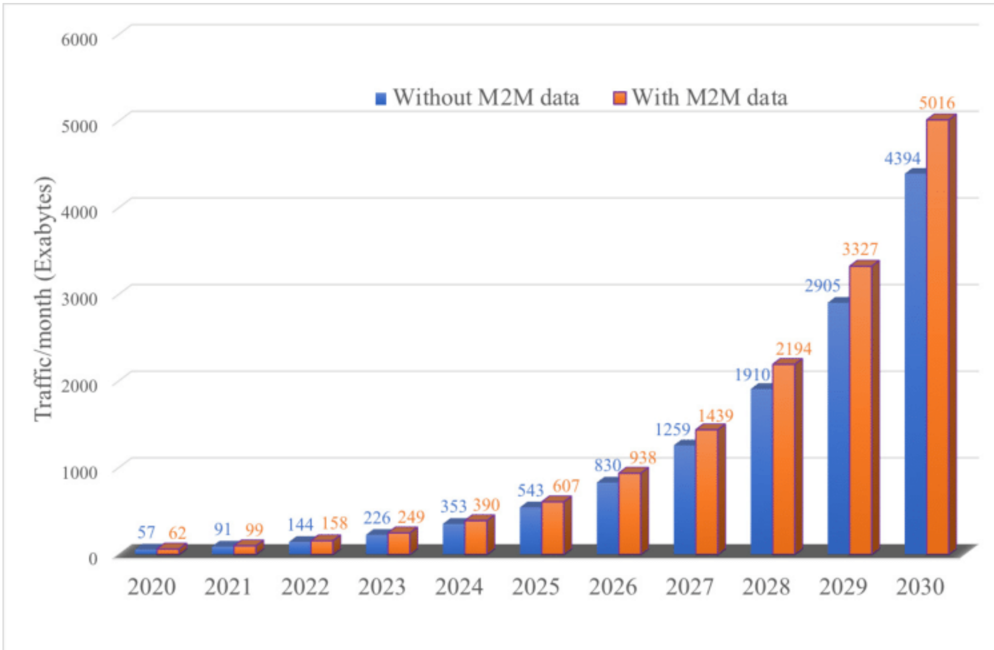

Fig. 1.2: Global mobile data traffic forecast by ITU [3].

such as artificial intelligence significantly increase the demand for high data interconnection bandwidth, while conventional copper cable interconnection fails to meet this demand. For example, data centers often require a large amount of distributed computing. In distributed computing, frequent and significant data exchanges are required between different servers, and the bandwidth of data interconnection often limits the performance of the overall task. As the scale of the algorithm becomes increasingly large, the occasions that require the use of multiple servers for distributed computing become increasingly important. High-speed data interconnection between servers has become a critical core technology, and this has become the main reason for data centers to use ultra-high-bandwidth silicon photonics-based data interconnection [5].

1.1 Silicon Photonics For Optical Interconnects

The concept of on-chip optical interconnection was first proposed by J.W. Goodman *et al.* in 1984 [6]. As a new interconnection method, optical interconnection has many incomparable advantages to electrical interconnection, such as high bandwidth, high parallelism, interference-free, and low loss [7]. As opposed to electrical interconnects, optical interconnect has become the preferred technology in high-performance CPUs, high-performance computers, and high-speed information processing systems [8].

Among various optical interconnection solutions, silicon-based optical interconnection technology is regarded as the most promising one [9]. Silicon materials have been widely used with CMOS integrated circuits, and their fabrication process is mature and can be mass and cost efficiently produced. In addition, silicon materials have excellent optical properties in the optical communication band (wavelengths around 1310 nm or 1550 nm) such as shallow absorption loss and high refractive index contrast. For these reasons, silicon-based optical integration is an ideal platform for inter-chip and on-chip optical interconnects due to its small size, low power consumption, compatibility with CMOS processes, high integration, and low cost. Moreover, since the fabrication is compatible with integrated circuits, a silicon-based integrated circuit can be introduced into electrical chips to achieve tight integration of optical communication circuits with control and driver circuits [10].

Communication systems have been widely developed in recent years, and the application areas of information technology have gradually become more widespread. The fiber optic backbone network that spreads worldwide, the fiber optical network connects thousands of homes to the large-scale data centers and computer central processing units (CPUs), all of which are facing the pressure of increasing massive data, information transmission, and processing. The optical fiber, invented by Nobel laureate Dr. Charles Kao, has excellent performance and can meet the challenge of information transmission capacity [11]. The main problems of fiber optic transmission lie in the optical-to-electrical conversion, various multiplexing/demultiplexing, and optical switching. Traditional optoelectronics technology is limited in integration and batch production due to material diversity, process complexity, high cost, large size, and high power, which to some extent constrain the development of optical transmission, especially optical interconnection technology [12]. Silicon-based optoelectronics integration technology developed from the late 20th century to the early 21st century has moved forward the development of optoelectronic devices [13].

Photonic integrated circuits (PICs) have gradually developed into a mature and robust technology in recent years. As opposed to electronic circuits that integrate transistors, capacitors, and resistors, PICs integrate various optical or optoelectronic devices, such as lasers, electro-optic modulators, photodetectors, optical attenuators, optical multiplexers/demultiplexers, and optical amplifiers. PICs have unparallel advantages in the field of information transmission and processing, so they are widely used in optical fiber communication, spectral sensors and quantum information processing, along with various other applications [14].

The material of integrated circuits is relatively simple. The typical semiconductor materials include the first-generation semiconductor material silicon emerged in 1950 and is a mature technology with high integration capability. The second-generation compound semiconductor material is gallium arsenide (GaAs) which has a high mobility and direct band gap for optical communication and radio frequency circuits [15]; and the third-generation semiconductor materials are silicon carbide (SiC) [16] and gallium nitride (GaN) [17] which are currently being developed for power semiconductor devices, with high mobility, good thermal conductivity, and high voltage resistance. For photonic integrated circuits, PICs can be divided into monolithic and hybrid integration according to whether integrated components are made on the same material abstract or not. Hybrid integration uses different materials to implement multiple devices and then confines these different functional components to a suitable substrate. The advantage of hybrid integration is that each device is made of the most suitable material for its function and performs better. Thus, materials for PIC are more complex, and different devices often use different materials. In contrast, the monolithic integrated PIC implements the design of various active and passive optical devices through one material, so there is no problem of adaptation between various different materials. Monolithic PICs have significant advantages over hybrid PICs, both in terms of energy efficiency and reliability, etc.

However, PICs still have some drawbacks. Since it was first proposed 40 years ago, PIC has advanced at a very slow rate. Only large-scale monolithic PICs have achieved breakthroughs. The inherent technical reason is how to integrate active and passive optical devices on a single chip has always been a difficult problem. Besides, the cost of developing an integrated optical path process is quite high. Overall, the excellent characteristics obtained prove that this expense is worthwhile.

Silicon-on-insulator (SOI) is a structure widely used in integrated circuits. It has the advantages of high integration, high speed, high-temperature resistance, high thermal conductivity, radiation resistance, and low power consumption, and is compatible with CMOS. It has a low processing cost and can realize large-scale production. Besides, the SOI structure has advantages that cannot be compared to silicon: it can achieve dielectric isolation of components in integrated circuits, eliminating the parasitic latch-up effect in silicon CMOS circuits. Thus, SOI is promising to become the mainstream technology for low voltage and low power consumption integrated circuits. The SOI structure is created by growing an insulating layer of silicon dioxide on a silicon substrate and then adding a silicon layer on top of the silicon dioxide to form a sandwiched structure confining the light. Silicon has lower loss in the near-infrared wavelengths in contrast with other semiconductor materials, and the refractive index of silicon (3.48 at the wavelength of 1.55 µm is much larger than that of silicon dioxide 1.44 at the same wavelength). The cross-sectional area of SOI waveguides is small under single-mode conditions. Additionally, because of the strong confinement of the optical field in the waveguide, the bending radius can be made small, achieving high integration of PIC. In addition to SOI, InP can also serve as an optional material for optical chips. A significant advantage of the InP system is that it can integrate lasers on a chip, including lasers that cannot be directly realized by SOI. However, the price of InP wafers is much higher than that of SOI wafers. Besides, InP optical chips are more complicated to fabricate. In summary, SOI is expected to be the primary direction of silicon photonics development in the future [18].

In the past few decades, advancements in microelectronics based on silicon (CMOS) has allowed for brilliant achievements and profoundly changed all aspects of society. However, CMOS technology is limited by Moore's Law. Moore's Law defines the decreasing size of semiconductor circuit transistors, which increases the number of transistors that can fit on a single chip. The number of transistors grows at an iterative rate of doubling every 18-24 months. In the past few decades, the development of the computer industry has followed Moore's Law for an extended period. More transistors translate into faster and more efficient processors. Hence the performance of same-size electronic products will double every 18-24 months. With the continuous development of chip technology, Moore's Law gradually encountered physical limitations. At present, the size of transistors has reached the nanometer level, and the possibility of continued shrinkage is gradually becoming highly improbable. Moore's law predicted development trajectory seems to have approached the limit [19]. However, the miniaturization of the transistor leads to more data being communicated, which is hardly met by CMOS. Consequently, there is an urgent need for a low-power, high-bandwidth interconnect technology for data exchange within future super-scale processors.

Silicon-based optoelectronic technology uses a large-scale semiconductor manufacturing process to integrate various photonic, electronic, and optoelectronic devices on insulator thin-film silicon wafers, including light sources, optical waveguides, modulators, *etc.* The development of photonics and microelectronics can complement each other. By 2020, microelectronics technology may advance from the current 5 nm process node to the 2-3 nm node. However, at this scale, the number of atoms that can be accommodated is less than 15. The growing impact of quantum effects has led to a significant increase in the unreliability of transistors, posing a major challenge to the further advancement of microelectronics technology. Despite the lag in microelectronics technology, the demand for high-speed information processing in modern society remains high, and the issue of information congestion has emerged as a critical challenge. To tackle this problem, researchers have recognized the potential of another information carrier - photons. As a medium for information transmission, photons offer several advantages over electrons, including stable and controllable modulation and reuse dimensions such as amplitude, phase, wavelength, polarization state, and mode. Additionally, photons have larger bandwidth, higher spectrum utilization rates, and greater communication capacity, making them a promising alternative for addressing the issue of information congestion. However,

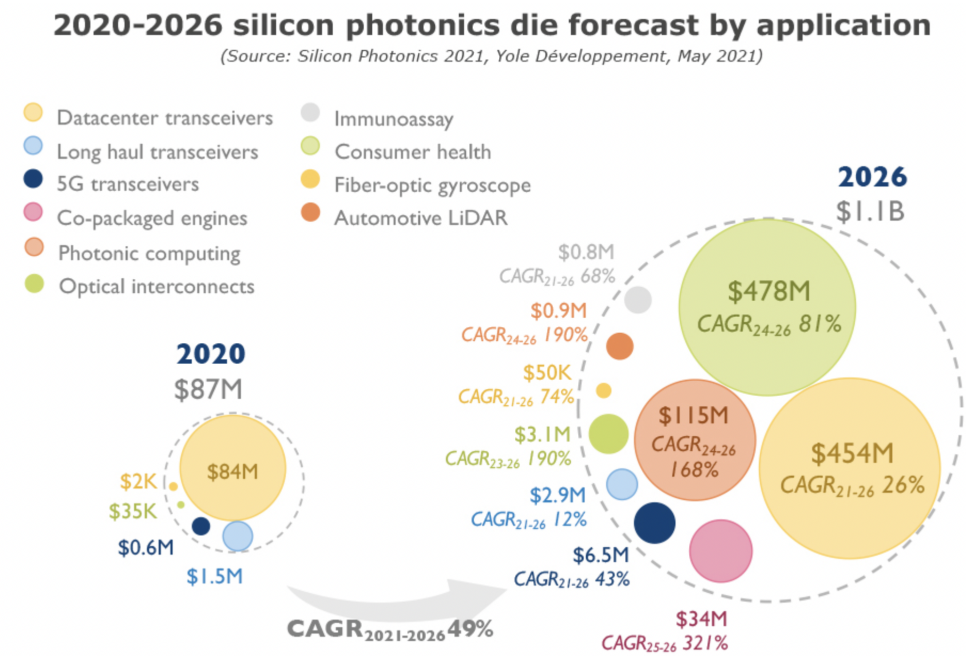

Fig. 1.3: Future application of silicon photonics. Source: Yole Development.

the mature process of microelectronics, the relatively cheap production cost, and the good performance shown is currently unattainable by silicon photonics. Optoelectronics and microelectronics are effectively integrated on a small chip [20]. Fig. 1.3 illustrates the future application in the following years. The main application of silicon photonics is optical communication. New applications have entered the market in 2020 such as immunoassays and fiber-optic gyroscopes (FOG). Novel silicon photonics applications, including LiDAR, consumer healthcare, and electronic sensors, are expected to reach the market in the coming years.

1.2 Division Multiplexing Technologies

In recent years, with the rapid development of cloud computing and data centers, optical interconnects have gained increasing attention due to their outstanding advantages in power consumption, speed, and bandwidth that are incomparable to electrical interconnects. To take full advantage of the optical interconnect bandwidth, the development of wavelength division multiplexing (WDM), polarization division multiplexing (PDM), and mode division multiplexing (MDM) technologies is an effective way. The combined use of multiplexing methods can form a multi-dimensional hybrid multiplexing technology, thereby significantly increasing the number of optical interconnection channels and transmission capacity. Given that on-chip integrated devices such as demultiplexers are essential to realizing multi-channel parallel transmission systems, the progress of ultra-small on-chip integrated devices based on silicon photonics technology, including WDM, PDM, MDM multiplexer-demultiplexer devices, and hybrid multiplexer-demultiplexer devices, is highlighted and summarized in this thesis. An example of the integrated chip concept with three multiplexing dimensions of mode, wavelength, and polarization is illustrated in Fig. 1.4 [21]. In this figure, the system enables the transmission of 12 different channels, including 3 different wavelengths $\times$ 2 polarization states $\times$ 2 mode orders. The input channel is converted into four channels of different mode orders and polarization status by mode demultiplexers and polarization splitters, and the wavelength division multiplexing of three wavelengths is achieved by ring resonators.

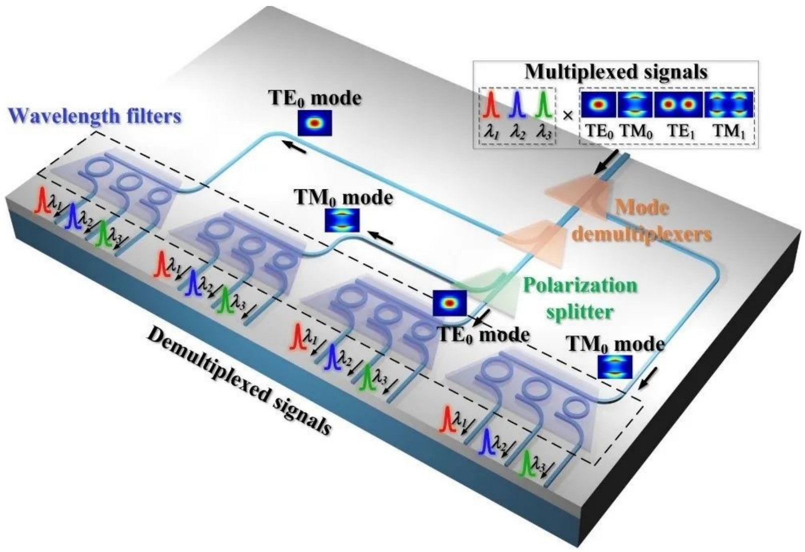

.

Fig. 1.4: Demonstration diagram of the integrated chip concept with three multiplexing dimensions of mode (TE_0, TM_0, TE_1, TM_1), wavelength (λ_1, λ_2, λ_2), and polarization (TE and TM) [21].

1.3 Thesis Motivation

Optical interconnect is a promising solution for future communication systems with large data capacity. Several multiplexing techniques are used to increase the data throughput, including WDM, MDM, and PDM. Although WDM is a straightforward technique and has been successfully developed, it requires multiple lasers, which translates into higher cost, packaging complexity, and power consumption. In recent years, MDM has gained significant attention for on-chip optical transmission systems. In this multiplexing technique, spatial and orthogonal modes are used as data channels carrying different signals to address the challenge of Shannon's limit regarding the limited data rate and capacity for error-free transmission over data channels. However, coupling between different modes occurs due to the simultaneous transmission of multiple mode orders. Low insertion loss (IL) and low crosstalk (XT) mode coupling is difficult to achieve in practice. Inter-mode crosstalk has also become the main challenge for MDM's continuous development. The silicon-based optical interconnection technology combining MDM and PDM can effectively solve this problem. Since transverse electric (TE) and transverse magnetic (TM) modes have different mode field distributions and transmission properties, there is almost no crosstalk between TE and TM modes. By converting the higher order modes that are initially in the same polarization state into two co-existing polarization modes that are in different states, the system's transmission efficiency is improved. The PDM-MDM system significantly reduces inter-mode crosstalk while maintaining the same number of data transmission channels. The silicon-based optical interconnection technology combining MDM and PDM can thus be a promising solution. Considering different modes and polarization states, it is necessary to consider the fundamental mode as well as high-order modes, TE and TM polarization states for MDM and PDM optical interconnects. Thus, improving the building blocks for silicon photonics PDM-MDM optical interconnects is of great importance.

Various MDM-PDM devices including mode multiplexer (mux) and demultiplexer (demux), multimode crossing, polarization beam splitter (PBS), 3-dB couplers, and switches realizing an MDM optical interconnect have been reported. Among these, PBS/PBC and multiplexer/demultiplexer are deemed essential building blocks to realize the implementation of PDM-MDM systems. The PBS/PBC building block enables the application of PDM technology. The PBS splits different polarization modes at the output port and the PBC has the exact same structure as the PBS and is used at the input of the system for the combinations of different incident polarization modes. The multiplexer/demultiplexer devices are designed to enable the application of MDM technology. As the input grating coupler generally excites the fundamental mode of the TE/TM polarization state, the multiplexer converts the fundamental mode into a higher order mode while the demux achieves the opposite: converting the higher order mode into a fundamental mode that can be detected. An optical coupler is used before the multiplexer and after the demultiplexer part to realize the splitting and combining of multiple modes. Optical switches are capable of exchanging payload information between different mode channels, which is essential to achieve functional on-chip PDM-MDM optical networks. The performances of reported MDM switches do not have yet the capability of meeting the transmission expectation. Indeed, excessive insertion loss and inter-modal crosstalk lead to errors, which will affect the quality and effectiveness of the switch. In this thesis, two PDM-MDM switches are proposed for high-performance interconnect with lower loss and crosstalk.

1.4 Thesis Overview

This thesis is organized into five Chapters. In Chapter 1, the need for optical interconnects was explained in the context of meeting the booming data transmission demand for capacity. The advantages of silicon photonics in the electronic industry were discussed for such applications. The three division multiplexings (WDM, MDM, and PDM) were then discussed and compared.

Chapter 2 provides a comprehensive literature review of the MDM and PDM systems. The main building blocks, including mode multiplexer, PBS, and optical mode filters with good performance, are summarized. The latest design topology and structure are also discussed in this chapter.

In Chapter 3, a four-mode polarization-mode insensitive 3-dB coupler based on an adiabatic coupler is designed and experimentally demonstrated. The proposed design works for the first two transverse electric (TE) modes and transverse magnetic (TM) modes as well. The optimization process, experiment setup, and measurement results are also discussed in this chapter.

In Chapter 4, two possible optical switch topologies are proposed. One is a four-mode optical space-switch based on the optimized designed 3-dB coupler discussed in Chapter 3. An 8×8 optical switch matrix consisting of 12 Mach-Zehnder interferometer (MZI) switches is proposed with improved transmission throughout. The other topology is an eight-mode optical mode switch which has the capability of switching the sequence of mode orders. This structure provides 24 possible switching combinations of data channels to meet the higher requests of the transmission system. The insertion loss and crosstalk performance are compared to find their potential applications.

The thesis concludes with Chapter 5, which includes a summary of the application fields and a brief discussion regarding the future research directions using inverse design methodology.

1.5 Claim Of Originality

The research works presented in this Master's thesis, including the concept, design, and experimental validation, were performed by the candidate, Heming Xu, and conducted under Prof. Odile Liboiron-Ladouceur's supervision. The design was fabricated by Applied Nanotools Inc. (ANT) in Canada. The measurement of the fabricated chip was validated in our lab located at McGill University. The majority of the contents of this thesis were written as a draft manuscript and are currently being finalized for submission to Optics Express.

Chapter 2

Background

In this chapter, the background on PDM-MDM optical interconnects is presented. Specifically, SOI waveguide numerical simulation algorithms are discussed in Section 2.1. The coupled mode theory and modal crosstalk are explained in Section 2.2. An overview of the reported building blocks for PDM interconnects are presented in Section 2.3. State-of-the-art MDM interconnects are reviewed and the progress in MDM silicon photonics is summarized in Section 2.4. Finally, approaches in combining PDM and MDM technologies are shown in Section 2.5, along with their related applications.

2.1 SOI Waveguide Numerical Simulation Algorithm

Silicon photonics devices are mainly divided into active and passive devices. Passive devices do not include any electro-optic functions but include the following building blocks: fiber-to-waveguide couplers; filters and wavelength division multiplexing/demultiplexing, polarization control devices, mode order converters, optical circulators, optical filters, and optical attenuators and isolators. Active devices incorporates electro-optic functions such as semiconductor lasers, optical switches, modulators, and photodetectors.

For passive optical waveguides, the theory is relatively straightforward using Maxwell's equations simplified into the Helmholtz equations in the form of partial differentials, adding specific boundary conditions, and the boundary continuity conditions of the electromagnetic field. According to the condition that the field oscillates defined by a trigonometric function in the core layer and decays exponentially in the cladding layer, the eigenequations for TE and TM modes (related to the waveguide structure, material, and wavelength) are obtained, and the propagation constant as well as the effective index of the eigensolution are solved.

For the two-dimensional waveguide structure, the approximate Macartelli approximation is generally used to solve Maxwell's equations, or the equivalent refractive index method (EIM) method is used to convert the two-dimensional waveguide structure into a one-dimensional structure to simplify the calculation. However, these two methods have specific errors, and the accuracy of the results is low for some structures (*e.g.*, ridge waveguide).

For a more accurate numerical simulation of optical transmission along the waveguide, there are beam propagation methods (BPM) and eigenmode expansion methods (EME). BPM uses paraxial approximation, ignoring the rapid changes of the light field, and the amount of calculation is relatively small. It calculates the scalar field but cannot calculate the polarization-related characteristics. It is mainly used to calculate the structure confined by weak waveguides and is sensitive to large angles and phases. EME calculates Maxwell's equations in the frequency domain with higher accuracy and quick calculation. It divides the device along the propagation direction and calculates the eigenmodes of each segment. When the length of the device changes, there is no need to recalculate, and the time it takes to scan the device is lessened.

The above two methods are mainly utilized to calculate relatively simple optical waveguide structures. EME can be solved by commercial computer aided design tools (CAD) such as Lumerical's Mode solution. Commercial CAD tools such as RSoft can solve BPM. In addition, there is also a 2.5D-finite difference time domain (FDTD) algorithm based on EIM, which converts the two-dimensional optical waveguide structure into a one-dimensional waveguide by the effective refractive index method, and solves the one-dimensional waveguide structure by FDTD. Its accuracy is between 2D-FDTD and 3D-FDTD.

For complex three-dimensional structures, three-dimensional simulation are generally used. The two methods that are mainly used are finite difference method (FDM) and finite element method (FEM). The corresponding commercial software are FDTD solution such as in Lumerical and COMSOL. The difference is that FDM uses a square grid and that FEM uses a triangular grid. However, these two methods are computationally expensive and time-consuming when analyzing large-area complex structures (such as AWG) and high-Q devices (such as microring resonators).

For active optical devices, the theoretical models are more complex, including optical waveguide theory, energy band theory, carrier migration theory, and high-speed radio frequency circuits. Both passive and active structures are investigated in this thesis.

2.2 Coupled Mode Theory

Mutual coupling between optical modes is essential in the design of integrated optic devices. The transfer of power from one mode to another mode in the same waveguide or the exchange of energy between two waveguides is referred as optical waveguide coupling. Coupled mode theory serves as the primary tool for designing optical couplers, switches, and filters. The theory of mode coupling is presented in this section based on the theory presented in [22].

First, we consider the coupling of two modes propagating in the same direction, say the forward direction in z, over a length L, as is shown in Fig. 2.1 below. In this case, β_a>0 and β_b>0. The coupled equations are shown in Eq. (2.1,2.2).

$$\frac{dA}{dz} = i\kappa_{ab} B e^{i2\delta z} \tag{2.1}$$

$$\frac{dB}{dz} = i\kappa_{ba} A e^{-i2\delta z} \tag{2.2}$$

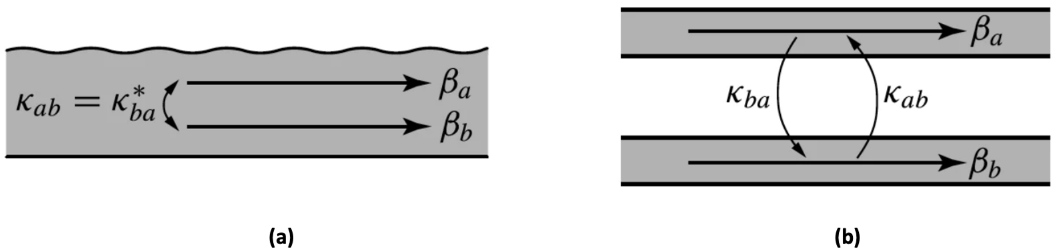

Fig. 2.1: Directional coupling between two modes of propagation constants β_a and β_b. (a) in the same waveguide and (b) in two parallel waveguides.The conjugate in (a) is to indicate the opposite direction of light transmission.

where A and B are the amplitudes of the two modes. κ_{ab} and κ_{ba} are the coupling coefficients. For most optical devices, κ_{ab}=κ_{ba} according to coupling reciprocity. The coupling coefficient are given by the Eq. 2.3.

$$\kappa_{ba,ab} = \frac{\omega\varepsilon_0}{4}\int_{-\infty}^{\infty}[n_c^2(x) - n_{a,b}^2(x)]E_a(x)E_b(x)dx \tag{2.3}$$

δ is the phase mismatch between the two modes and can be expressed as Eq. 2.4.

$$\delta = \frac{1}{2}(\beta_{ba} - \beta_{ab}) \tag{2.4}$$

These equations for coupling are generally solved as an initial-value problem with the initial values of A(z_0) and B(z_0) given at z=z_0 to find the values of A(z) and B(z) at any other location z.

A significant perturbation is required for directional coupling in either case [22]. If there are no perturbations in the waveguide, (for instance the dimensions of the waveguide do not change with position, and there are no changes in the dielectric constant) the modes will be completely independent from one another. However, any deviation from this well-defined waveguide structure perturbs the modes and couplers energy between them. Perturbations can arise through two mechanisms: either the dielectric constant of the structure is modified ($\Delta\varepsilon$) from what the mode expects to see, or an electric field from a second source appears in the waveguide, and excites a mode of the structure. The perturbation vector is the product of the change in the dielectric constant and the E-field which can be expressed as Eq. (2.5).

$$P_{pert}(x,t) = \frac{1}{2}\varepsilon_0[E_a(x)A(z)(n_c^2(x) - n_a^2(x))e^{-j(\beta_a z - \omega t)} + E_b(x)B(z)(n_c^2(x) - n_b^2(x))e^{-j(\beta_b z - \omega t)}] \tag{2.5}$$

$E_a(x)$ and $E_b(x)$ are the field distributions of the two waveguide, $n_a(x)$ and $n_b(x)$ are the refractive index distribution of the two waveguides. The total perturbation consists of perturbation on field B due to field in waveguide A and the perturbation on field A due to field in waveguide B. The coupling efficiency for a defined length L is expressed as Eq. (2.6).

$$\eta = \frac{P_b(L)}{P_a(0)} = \frac{{\kappa_{ba}}^2}{{\beta_c}^2} sin^2\beta_c L \tag{2.6}$$

where

$$\beta_c = (\kappa_{ab}\kappa_{ba} + \delta^2)^{\frac{1}{2}} \tag{2.7}$$

The optical power is exchanged periodically between two modes with a coupling length l_c where maximum power transfer occurs.

$$l_c = \frac{\pi}{2\beta_c} \tag{2.8}$$

Fig. 2.2 shows the periodic power exchange between the two coupled modes as a function of z. As can be seen, complete power transfer can occur only in the phase-matched condition when δ =0.

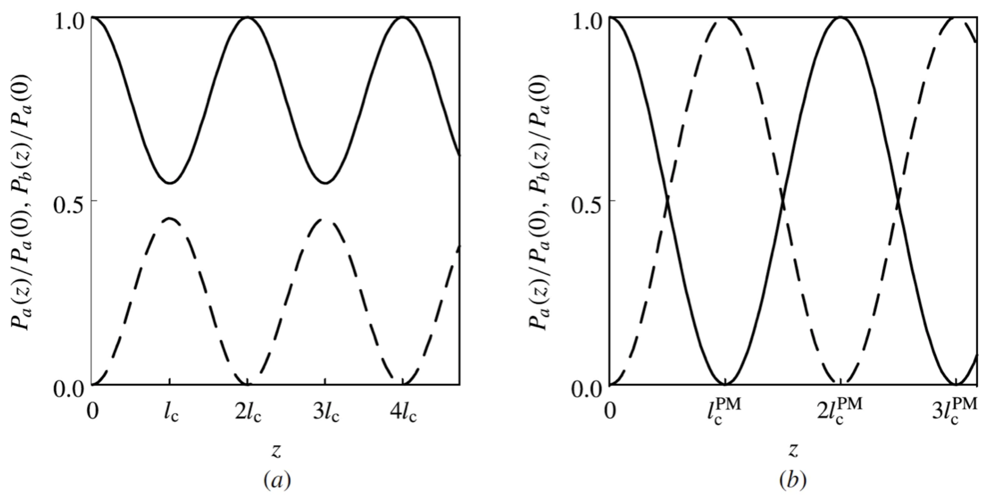

Fig. 2.2: Periodic power exchange between two coupled modes for (a) phase-mismatched condition $\delta \neq 0$ and (b) phase-matched condition $\delta = 0$. The solid curves represent $P_a(z)/P_a(0)$, and the dashed curves represent $P_b(z)/P_a(0)$ [22].

2.3 Key Building Blocks For MDM Silicon Photonics Optical Interconnects

Mode division multiplexing (MDM) refers to the technique in which multiple orthogonal optical modes with different paths and mode field distributions, carrying different information, propagate together in the same multimode optical waveguide. The concept of MDM dates back approximately 40 years ago [23]. In recent years, MDM has received renewed attention as Moore's law is reaching a limit in the field of electronics and integrated photonics is trying to keep up with growing demand.

Unlike Moore's Law in traditional microelectronics, the device density of photonic integrated circuits (PICs) is limited by the intrinsic properties of light waves; the wavelength size is not as compact and dense as in electronic devices. As a physical dimension that can carry information, mode multiplexing can further increase the number of channels while being compatible with wavelength multiplexing and reducing the number of lasers required while maintaining the number of channels. MDM can realize the propagation of multiple modes in a multimode waveguide to improve the channel density. In the MDM photonic integrated chip, the key devices for the generation, modulation, exchange, and processing of the multi-mode signal by the on-chip optical waveguide include the multimode optical interface coupling the chip to the off-chip optical fiber, the multimode passive devices (such as bending, crossing, power splitter, mode multiplexers) and multimode active devices (such as optical switches). Currently, the number of mode channels of an on-chip MDM is limited to 12 in practice. The main challenge for applying higher-order mode multiplexing technology is the inter-modal coupling which results in high crosstalk.

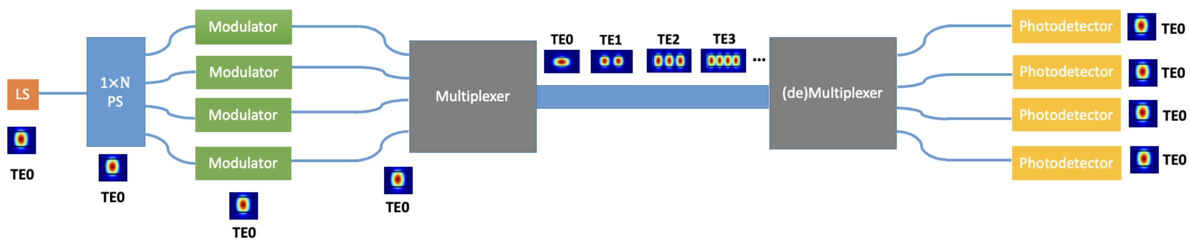

Fig. 2.3: Schematic diagram of a MDM integrated optical communication transmission system [24].

Fig. 2.3 from [24] shows the schematic diagram of an MDM integrated optical communication transmission system using N modes. The system consists of a laser source (LS), $1 \times N$ power splitter (PS), optical modulator, mode (de)multiplexers, multimode waveguide, and photodetector. The LS generates a continuous light source and is off-chip, and the PS is used to split a waveguide into N waveguides (N=4 in the figure). After the optical modulator, the modulated signal enters the mode multiplexer. Mode multiplexer converts the fundamental mode to higher order modes, the demultiplexer performs the opposite purpose. Different multimode devices can be added to achieve multiple functions, such as data exchanging ability of optical switches, and power splitting/combining capability of 3-dB couplers, in the middle of the MDM system between the multiplexer and demultiplexer. At the receiving end of the system, the mode demultiplexer recovers the fundamental modes for the photodetector to receive the signal. Finally, the optical signal is converted back to an electrical signal through the photodetector to achieve optoelectronic conversion.

2.3.1 Multiplexer and Demultiplexer

Mode multiplexing technology uses different modes in waveguides or optical fibers as channels for transmitting information. One of the critical devices is the mode multiplexer, which is used to realize the fundamental mode to high order mode conversion and load the excited modes onto a multi-mode waveguide. The mode multiplexer has become a popular research topic in the field of integrated photonic devices in recent years, and the primary implementation schemes reported so far are MMI structure [25], adiabatic coupler [26–29], asymmetric directional couplers (ADCs) [30–33], and Y-branch [34].

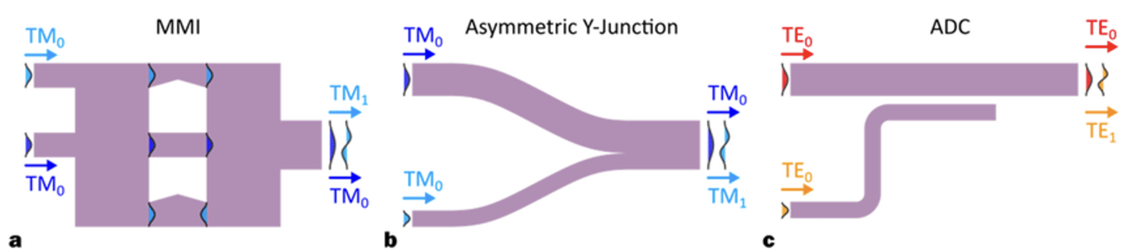

Fig. 2.4: The schematics for the silicon few-mode (de)multiplexers based on (a) multimode interference couplers (MMI), (b) asymmetric Y-junction and (c) asymmetric directional coupler (ADC) [30].

Table 2.1: Performance comparison for reported mode (de)multiplexers.

Reference	Year	L [µm]	IL [dB]	XT [dB]	BW [nm]	Modes	Structure	E/S
[25]	2012	80	1	-40	60 (C-band)	TM_0-TM_2	MMI	S
[26]	2013	300	0.5	-36	180 (C-band)	TE_0-TE_2	Adiabatic	E
[27]	2015	520	10	-11	200 (C-band)	TE_0-TE_2	Adiabatic	E
[35]	2017	310	0.2	-18	65 (C-band)	TE_0-TE_2	Adiabatic	E
[29]	2017	450	1.3	-20	100 (C-band)	TE_0-TE_3	Adiabatic	E
[36]	2017	500	0.2	-15	90 (C-band)	TE_0-TE_5 TM_0-TM_3	Adiabatic	E
[31]	2013	50	0.3	-16	100 (C-band)	TE_0-TE_1	ADC	E
[24]	2013	100	0.5	-23	70 (C-band)	TE_0-TE_3 TM_0-TM_3	ADC	E
[32]	2018	7.5	0.32	-30	100 (C-band)	TM_0-TM_1	ADC	S
[33]	2020	38.89	0.74	-24.88	100 (C-band)	TE_1-TE_4	ADC	S
[34]	2013	320	3.3	-9.7	25 (C-band)	TE_0-TE_2	Y-Branch	E
[34]	2021	75	1.2	-16	200 (O/C-band)	TE_0-TE_1	ADC	E

*L, Length; IL, Insertion Loss; XT, Crosstalk; BW, Bandwidth; E, Experiment; S, Simulation.

Table 2.1 summarizes the respectively reported multiplexers with their performances in the past 10 years. All the multiplexers can be divided into four types. The first type is based on MMIs which are typically suitable for a broadband wavelength operation. An N-fold self-imaging can be achieved by optimizing structure parameters including waveguide width and length. Of these four types, the MMI-type mode multiplexer structure is more complicated to expand the number of mode channels. The second type of mode (de)multiplexer is based on an adiabatic structure. The adiabatic mode evolution coupled mode multiplexer has exceptional flexibility in its design, and mainly contains structures such as slow-varying asymmetric Y-branch, slow-varying directional coupler, *etc.* Thus, according to the information in Table 2.1, the adiabatic structure is usually long but has certain advantages, such as large bandwidth [37]. The third type of mode (de)multiplexer is based on a cascaded ADC consisting of two asymmetric waveguides in the coupling region. The ADC-based structure has the advantages of a small footprint and simple design, making it easier to realize multi-channel mode multiplexers by cascading multiplexed devices. Moreover, it has the flexibility to extend to multiple mode channels [31]. In terms of performance, the mode multiplexer based on asymmetric coupling structure has low crosstalk, low insertion loss, and large bandwidth. Due to these multiple attributes, this multiplexer type has gained much attention from the photonics community [38]. The last structure type is a Y-branch-based multiplexer. The asymmetric Y-branch is long enough to combine/separate the different modes but has high crosstalk due to small gaps in the branch. Therefore, finer fabrication technology must be used to realize a small gap between waveguides. In addition, these structures can easily be cascaded in parallel [39] or in series [40] to provide more channels as shown in Fig. 2.5.

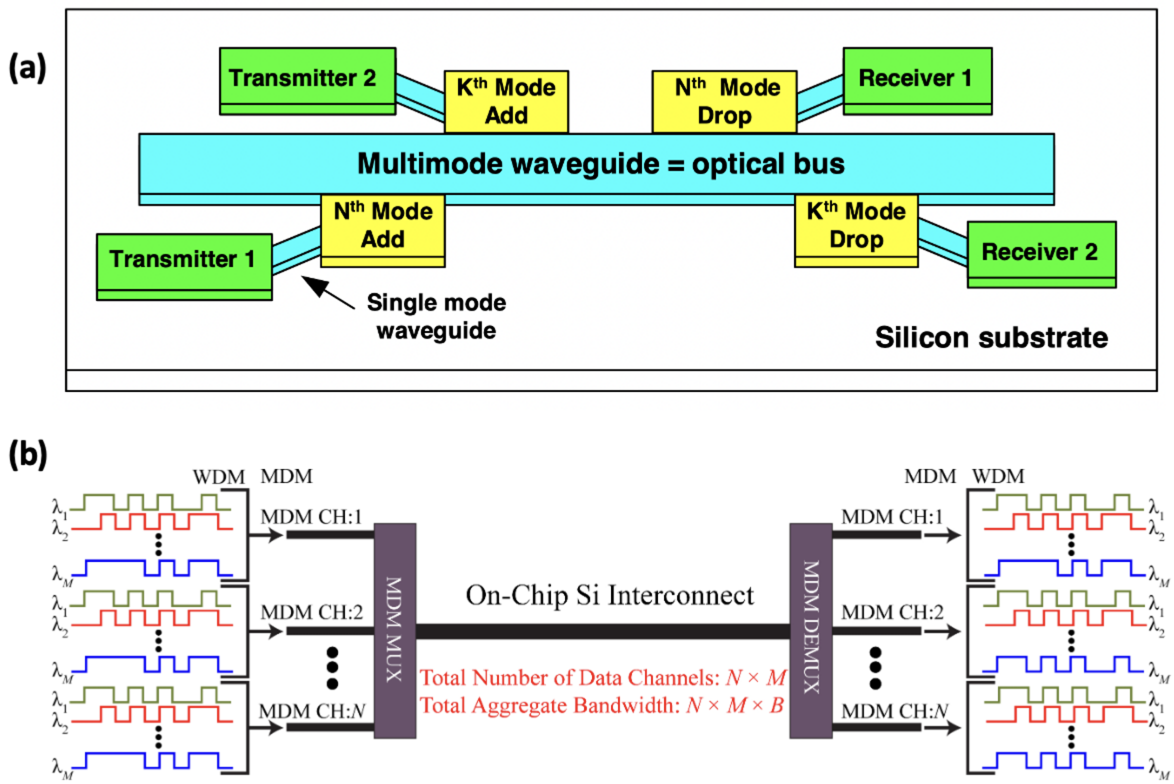

Fig. 2.5: (a) Multiplexer cascaded in parallel [39]; (b) Multiplexer system cascaded in series [40].

2.3.2 Mode Converter

In multimode systems, optical mode converters play an essential role because of the need for multiple orders of mode conversion. For example, mode multiplexing and demultiplexing at the receiver and input sides of the system implement conversion between fundamental and higher-order modes. Mode converters can effectively increase the flexibility and capacity of MDM systems.

Three main approaches to implement mode converters are phase matching, coherent scattering, and beam shaping. The extensive studies on mode converters include devices based on tapered directional couplers [31], asymmetric Y-branches [40–42], and multichannel branching waveguides (MB) [43, 44]. They have good performance, but the size of the devices is quite large. In contrast, directional couplers with asymmetric structures [24, 45] are able to optimize the device size but are very sensitive to the fabrication process. Grating-based couplers (GC) [46–49] similarly require a high resolution of the fabrication process. Given these limitations, MZI-based structures are a relatively promising method for mode conversion, being able to convert between fundamental modes and multiple higher order modes efficiently. Table 2.2 summarizes the respective performance of the reported mode converters with their performances over the past decade. According to Table 2.2, GC based mode converters have better performance in device length, IL and XT. ADC based coupler is a promising solution for accommodating higher order modes. Fig. 2.6 shows a mode converter to allow mutual conversion between TE_0, TE_1 and TE_2 using inverse design topology with a compact footprint (2.35×4.85 µm^2) [50].

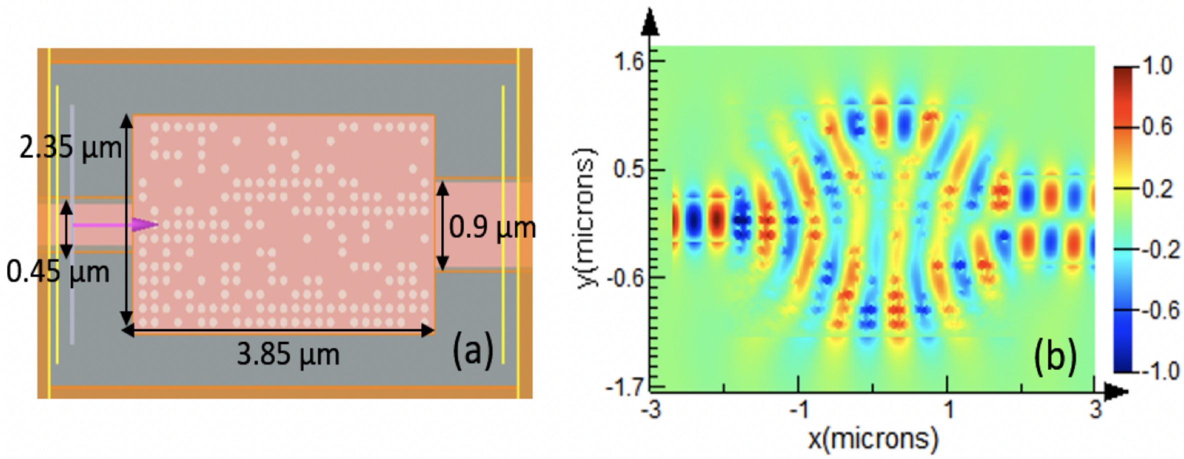

Fig. 2.6: Schematic of mode converter [50].

Table 2.2: Performance comparison for reported mode converts.

Reference	Year	L [µm]	IL [dB]	XT [dB]	BW [nm]	Modes	Structure	E/S
[31]	2016	50	0.3	-16	100 (C band)	TE_0-TE_1	DC	E
[40]	2014	1200	0.7	-21.8	100 (C band)	TE_0-TE_1	Y-Branch	E
[41]	2014	800	0.7	-22	300 (C band)	TE_0-TE_1 TM_0-TM_1	Y-Branch	S
[42]	2014	1100	0.13	-25.5	210 (C band)	TE_0-TE_3	Y-Branch	S
[43]	2003	4100	1.5	-10.2	100 (C band)	TE_0-TE_3	MB	E
[44]	2004	3140	1.2	-9.4	90 (C band)	TE_0-TE_4	MB	E
[24, 45]	2014	50	3.5	-20	100 (C band)	TE_0-TE_3 TM_0-TM_3	ADC	E
[46]	2013	250	0.34	-22.6	20 (C band)	TE_0-TE_3	GC	E
[47]	2005	7.5	0.32	-30	90 (C band)	TE_0-TE_3	GC	S
[48, 49]	2014	20	0.74	-23	40 (C band)	TM_0-TM_3	GC	S

*L, Length; IL, Insertion Loss; XT, Crosstalk; BW, Bandwidth; E, Experiment; S, Simulation.

2.3.3 Multimode Power Splitter

The multimode power splitter is of great importance for MDM optical interconnects. The power splitters are typically used before the multiplexers and after the demultiplexers to demultiplex single-mode signals into multimode signals or vice versa.

Recently, great achievements have been made for single mode optical 3-dB couplers with enhanced performance using multimode interference (MMI) [51–53], Y-branches [54], directional couplers (DC) [55, 56], and adiabatic couplers (ADC) [57]. As for multimode design, dual-mode insensitive 3-dB couplers have been demonstrated using a multimode interferometer (MMI) for the first two transverse electric (TE) modes [58] and a directional coupler for the first two transverse magnetic (TM) modes [55]. Further, an MMI power splitter using inverse design significantly improves the device size [59]. In [60], a 3-dB splitter that works for the first three TE modes and one TM mode was proposed and validated through simulation based on a 300 nm-thick SOI using a shallow etching process. Furthermore, an MMI-based dual-polarization and mode division multiplexed power splitter for four modes (TE_0, TE_1, TM_0, TM_1) was experimentally validated [61]. However, the device is implemented using a pixelated meta structure, which is difficult and expensive to fabricate. Table 1 compared the performance of the reported MDM power splitter and our work. Our design achieves improvements in IL, XT and PI performance. In Table 2.3, we report the respective performances of the power splitters over the past six years. As we can conclude from Table 2.3, the power splitters are able to accommodate up to four different modes. However, an increase in the number of modes results in a significant increase in device length.

Table 2.3: Performance comparison for reported Multimode Power Splitter.

Reference	Year	L [µm]	IL [dB]	XT [dB]	BW [nm]	Modes	Structure	E/S
[58]	2021	48	0.65	-17	100 (C band)	TE_0-TE_1	MMI	E
[55]	2016	15.2	0.7	-14.3	30 (C band)	TM_0-TM_1	ADC	E
[59]	2020	4.5	1.5	-15	40 (C band)	TE_0-TE_1	MMI	S
[60]	2018	800	0.12	-18.5	164 (C band)	TE_0-TE_2 TM_0	ADC	S
[61]	2021	6	4.5	-15	40 (C band)	TE_0-TE_1 TM_0-TM_1	MMI	S
[62]	2019	24.2	1.3	-15	60 (C band)	TE_1-TE_2	SWG	S

*L, Length; IL, Insertion Loss; XT, Crosstalk; BW, Bandwidth; E, Experiment; S, Simulation.

2.3.4 Mode Insensitive Switch

Silicon-based photonic switching is a promising candidate for realizing high-speed, ultra-bandwidth data communication with a small footprint and low power consumption. The MDM switch can function as an MDM space switch or an MDM mode switch.

Fig. 2.7 shows the architecture of an N×N multimode spatial optical switch [63]. The

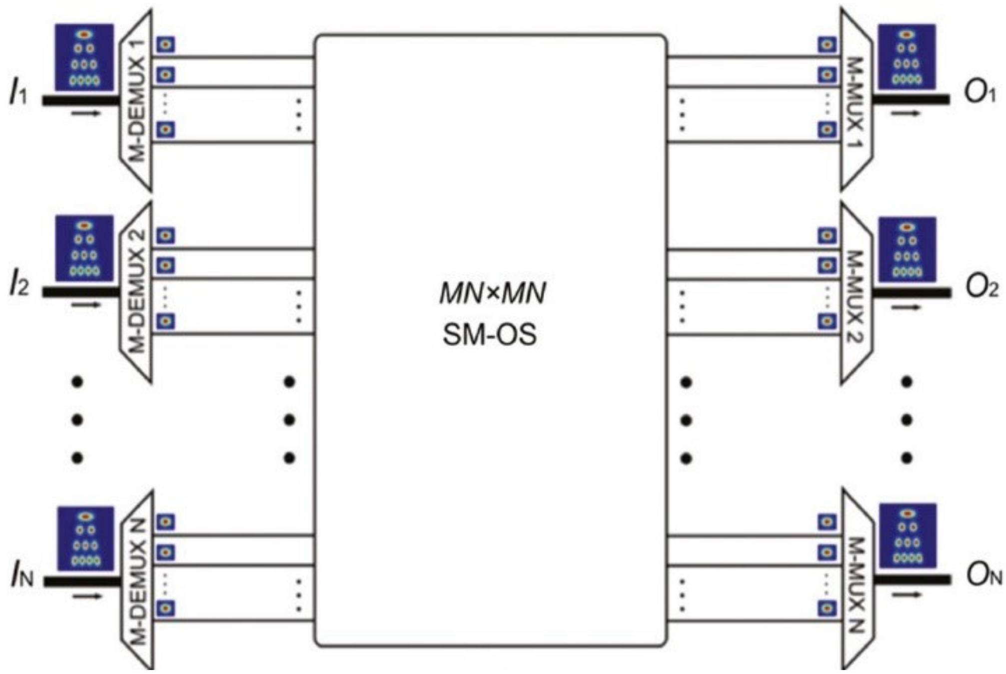

Fig. 2.7: An N×N multimode optical switch [63].

function of the optical space switch is to allow signal transmission between the input multimode waveguide and the output multimode waveguide. The transmitted signals from different input ports I_1, I_2, $\ldots I_N$ can be regarded as N mutually independent groups. Note that the spatial optical switch can only implement the data exchange between groups, not the signal transmission between modes within a group.

The function of the MDM optical mode switch is to transmit multiple mode signals from the input multimode waveguide to the output multimode waveguide, with the mode optical switch carrying out the mode order switching. The mode order optical switch enables switching from one mode order to another. In this optical mode switch, each mode carries its signal, and the i-th order mode of the input will be routed to the j-th order mode at

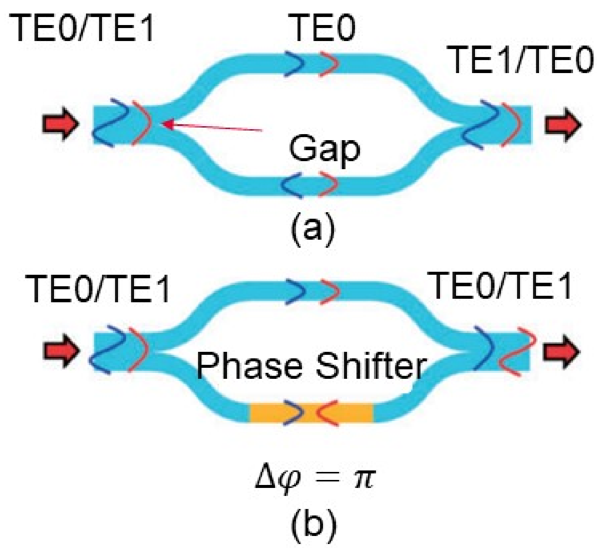

Fig. 2.8: Schematic view of optical mode switch for two modes. (a) OFF state and (b) On state [64].

the output port. In a practical optical interconnect system, the status of the MDM optical switch is electronically controlled to achieve dynamic data transmission between users.

Fig. 2.8 illustrates the two modes' schematic view of an optical mode switch. Using a modal switch that converts two TE modes, the mode switching is achieved by controlling the switching state of the phase shifter. When the phase shifter is on, the mode sequence is transformed, while the original sequence is retained when the switch is off. In recent years, the research on optical mode order switches shows that in order to be able to carry more modes, the length of the device will be increased. A Y-branch-based optical switch structure was proposed in [64], but this structure can only carry two modes and requires high robustness to fabrication errors for the narrow gap between waveguides. In addition, an

MMI-based structure for TM mode optical switch is provided in [25], but its structure has a larger size leading to more coupling and high crosstalk limiting its production application.

In recent years, various MDM optical switches have been demonstrated. Two-modes optical space switches were initially reported [62,65]. In [66], inverse design is used to improve the phase shifter performance. To achieve MDM interconnect systems, the (de)multiplexers are necessary to realize the mode conversion. However, that increases the length of the MDM device. A novel structure free of multiplexing is introduced in [67,68]. Meanwhile, the research on MDM mode order switch is still ongoing. MDM mode order switches are reported in [69]. For larger throughput, MDM is often combined with WDM [70, 71]. Table 2.4 summarizes the reported multimode optical switches with their performances in recent years. In conclusion, an MMI structure has a larger size while being compatible for higher order modes.

2.4 Key Building Blocks for PDM Silicon Photonics Optical Interconnects

Polarization-division multiplexing (PDM) is an effective method for multiplexing signals carried on electromagnetic waves. This allows for two channels of information to be transmitted on the same carrier frequency by using waves of two orthogonal polarization states. Both PDM and MDM are promising methods for signal multiplexing. They are

Table 2.4: Performance comparison for reported multimode switches.

Reference	Year	L [µm]	IL [dB]	XT [dB]	BW [nm]	Modes	Structure	E/S
[62]	2019	48	1.3	-15	60 (C band)	TE_1-TE_2	MZI	E
[65]	2017	243	1.9	-12	100 (C band)	TE_0-TE_1	MMI	E
[66]	2022	362	3.1	-14.9	40 (C band)	TE_0-TE_1	MZI	E
[67]	2018	443	1.2	-16.6	10 (C band)	TE_0-TE_1	MRR	E
[68]	2021	100	2.6	-20	100 (L band)	TM_0-TM_3	ADC	E
[69]	2021	800	1.1	-19.46	40 (C band)	TE_0-TE_2	MMI	E
[70]	2019	48	1.47	-14.02	30 (C band)	TE_0-TE_1	MRR	E
[71]	2019	500	0.4	-24.1	40 (C band)	TE_0-TE_1	MRR	E

*L, Length; IL, Insertion Loss; XT, Crosstalk; BW, Bandwidth; E, Experiment; S, Simulation.

often combined to maximize the transmission capacity of a system. MDM is for different order modes in the same polarization state, and PDM is for separating modes in the same order mode while in different polarization status. In this section, main building blocks of PDM system are discussed and compared with their applications and performance.

2.4.1 Polarization Beam Splitter

The polarization beam splitter (PBS) is key to solving the problem of polarization sensitivity of optical waveguide devices on silicon on insulator (SOI) platform. Grating coupler is sensitive to the polarization state due to the significant refractive index difference between the transverse electric mode (TE) and transverse magnetic mode (TM). The PBS can effectively solve this problem and enables the separation as well as a combination of different polarization states. Fig. 2.9 shows the structure and working principle of PBS [72]. The performance of PBS is compared in Table 2.5.

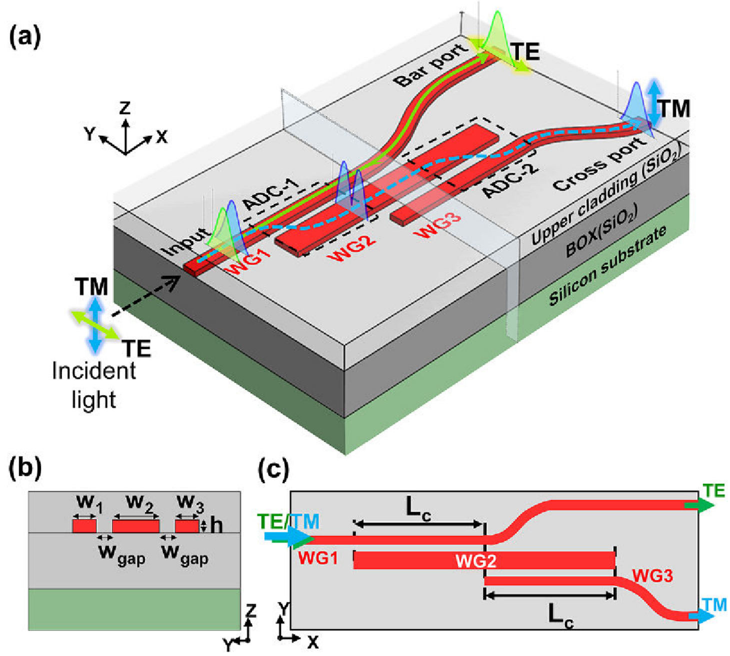

Fig. 2.9: Schematic configurations. (a) Schematic of the proposed PBS. (b) Cross-sectional view and (c) top view [72].

As we can see from the table, in recent years, the performance of PBS is improving, the size and insertion loss are gradually decreasing, and the operating bandwidth as well as the extinction ratio are increasing. Since the crosstalk between TE and TM modes is usually small, the extinction ratio has replaced inter-mode crosstalk as an important metric for PBS performance in most studies.

Table 2.5: Performance comparison for reported PBS.

Reference	Year	L [µm]	IL [dB]	XT (dB)	BW [nm]
[73]	2015	2.4	1.5	10	32 (C Band)
[74]	2016	1.4	2.1	15	100 (C Band)
[75]	2016	21	2	10	115 (C Band)
[76]	2016	6.8	1	18	81 (C Band)
[77]	2017	2	2.8	15	60 (C Band)
[78]	2019	71.5	2	20	77 (C Band)
[79]	2019	12.25	1	20	200 (C Band)
[80]	2020	7.2	2.5	10	150 (C Band)
[81]	2020	33.6	1	20	240 (C Band)
[82]	2020	14	1	15	72 (C Band)
[83]	2020	92.4	1	13	120 (C Band)
[84]	2020	14.5	0.6	20	30 (C Band)
[85]	2017	6.9	0.35	35	75 (C Band)
[86]	2022	15.5	2.5	20	70 (C Band)

*L, Length; IL, Insertion Loss; ER, Extinction Ratio; BW, Bandwidth;

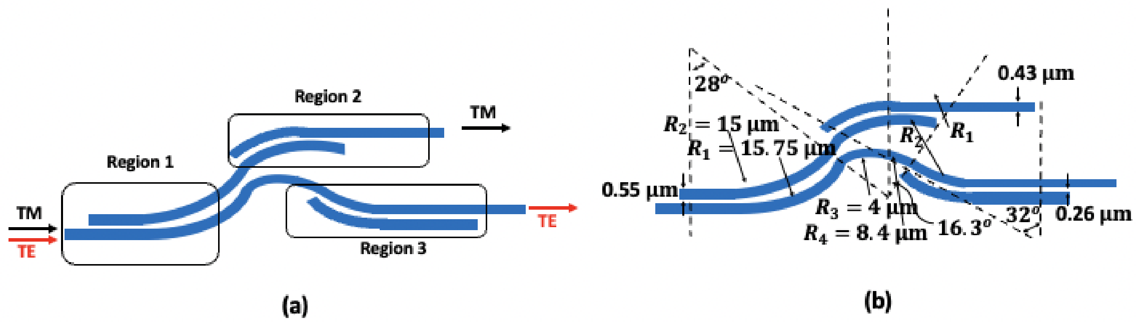

Fig. 2.10: Schematic configuration of the proposed PBS. (a) Working principle; (b) top view [85].

A high performance PBS is proposed and experimentally validated in [85]. In Chapter 3, we make use of an improved version. The working principle and simulation validation results are explained as follows. Fig. 2.10 shows the working principle and top view of this structure.

The width of the two waveguides in the directional coupler is optimized so that the effective refractive index of the TM_0 mode in the narrow waveguide is equal to that of the TE_0 mode in the wide waveguide. Thus, the phase matching condition is satisfied. The proposed PBS consists of three regions. The PBS is configured to make region 2 and region 3 work simultaneously as a part of the decoupling region 1. For the design of region 1 and region 2, the width of waveguides as well as R_1 and R_2 are determined according to the phase-matching condition of TM polarization status, so that an efficient coupling can be achieved by optimizing the value of θ_1 and θ_2. The region 2 is designed for TM polarization. Thus, for TE polarization, there is a large phase mismatch and the coupling of TE modes becomes weak. So when TE and TM modes are at the input port at the same time, only TM can propagate through region 2 and the output of the upper port, while most of the TE modes are filtered out via the optimized region 2. For the design of region 3, the parameters including R_3 and R_4 are designed for TE polarization status. TM polarization mode has a much shorter coupling length than TE polarization because of the weaker mode confinement. Therefore, by optimizing gap width and coupling length, the undesired power of TM polarization can be filtered out from the region 3.

2.4.2 Polarization Insensitive Power Splitter

A compact, low loss, broadband, and polarization-insensitive silicon-based power coupler is greatly needed for optical switches [87, 88], and (de)multiplexers [89]. Power splitters that work for both TE and TM fundamental modes are demonstrated using MMI based on subwavelength grating (SWGs) structures [90], silicon bent directional couplers [91], asymmetrical MZI [92] and Y junction [93]. Fig. 2.11 shows the structure and working principle of a 1×3 polarization insensitive power splitter for fundamental modes of both TE and TM [72].

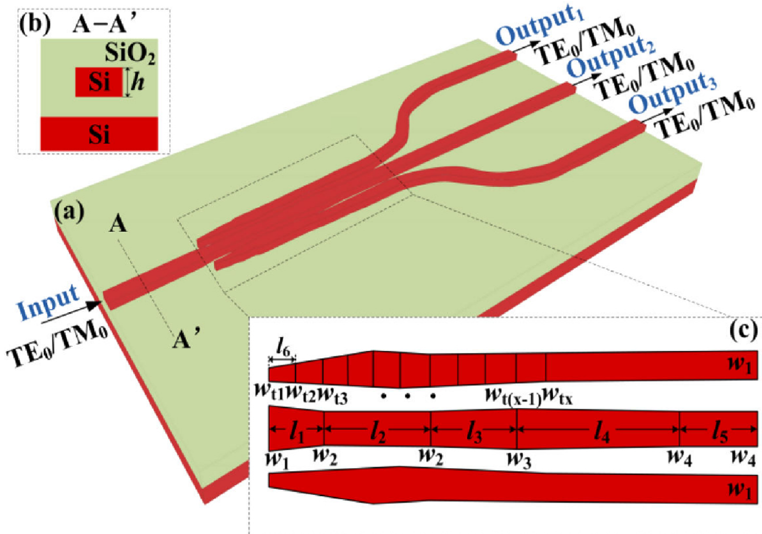

Fig. 2.11: (a) Three-dimensional structure of the proposed 1×3 polarization insensitive power splitter. (b) Cross-sectional view of the input waveguide. (c) Detailed drawing of the coupling regions [94].

The performances of polarization insensitive power splitters are summarized in Table 2.6 below. As we can see from Table 2.6, SWG is a promising solution for high performance polarization insensitive power splitter.

Table 2.6: Performance comparison for reported polarization insensitive power splitter.

Reference	Year	L [µm]	IL [dB]	XT [dB]	BW [nm]	Modes	Structure	E/S
[90]	2017	18.4	1	16	420 (C Band)	TE_0 TM_0	SWG	E
[91]	2017	50	1	15	110 (C Band)	TE_0 TM_0	DC	E
[92]	2012	160	2	10	165 (C Band)	TE_0 TM_0	MZI	E

*L, Length; IL, Insertion Loss; ER, Extinction Ratio; BW, Bandwidth; E, Experiment; S, Simulation.

2.4.3 Polarization Insensitive Optical Filter

Silicon-based optical filters provide fast linear photonic signal processing and are one critical device for realizing various optical interconnect applications. Therefore, it is quite important to realize polarization-insensitive optical filters (PIOFs) in the PDM system. Several approaches incorporate PIOF using square waveguides, MZIs, and phase-shifted polarization-rotating Bragg gratings (PRBGs). Deng *et al.* used MZIs for a PIOF which can ensure that both TE and TM modes have the same effective index [95]. However, MZI-based filters have a large footprint. A polarization-insensitive grating-based optical filter that consists of TE multimode waveguide grating (MWG) and TM MWG is schematically illustrated in Fig. 2.12 [96, 97]. Adiabatic dual-core taper is designed to drop TE_1 and TM_1, simultaneously.

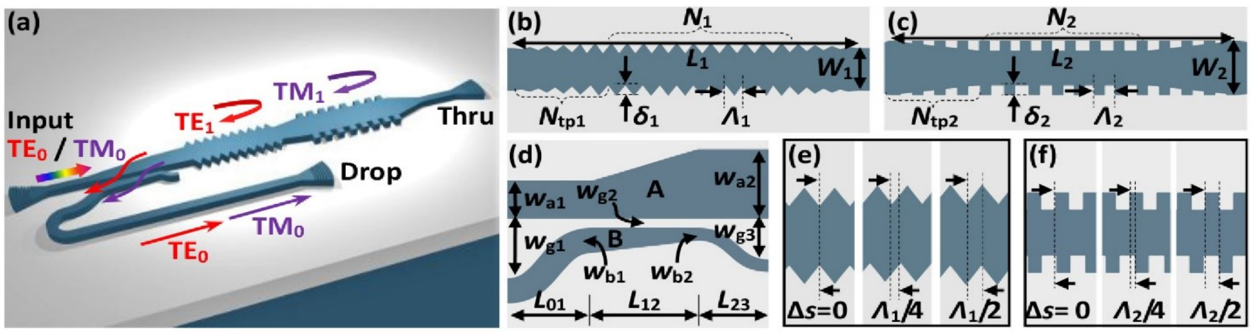

Fig. 2.12: Schematic configurations. (a) The proposed polarization-insensitive filter; (b) The MWG with triangular corrugations; (c) The MWG with rectangular corrugations; (d) The mode (de)multiplexer based on an adiabatic dual-core taper; (e) The longitudinal apodization for the grating with triangular corrugations; (f) The longitudinal apodization of the grating with rectangular corrugations [96, 97].

2.4.4 Polarization Insensitive Phase Shifter

The polarization insensitive phase shifter is another essential building block of the PDM optical switch. A polarization-insensitive phase shifter was first reported based on a couple of polarization rotators (PRs), as shown in Fig. 2.13. In this design, the differential group delay (DGD) of the phase shifter is said to be eliminated. The polarization state will be orthogonally flipped as the light propagates through each phase shifter [98]. Furthermore, specific materials are used for achieving polarization insensitive phase shifters including InGaAsP-InP [99]. In general, polarization-insensitive phase shifter needs to be explored further. A comprehensive introduction of two examples of polarization insensitive phase shifters are discussed in Section 4.2.1.

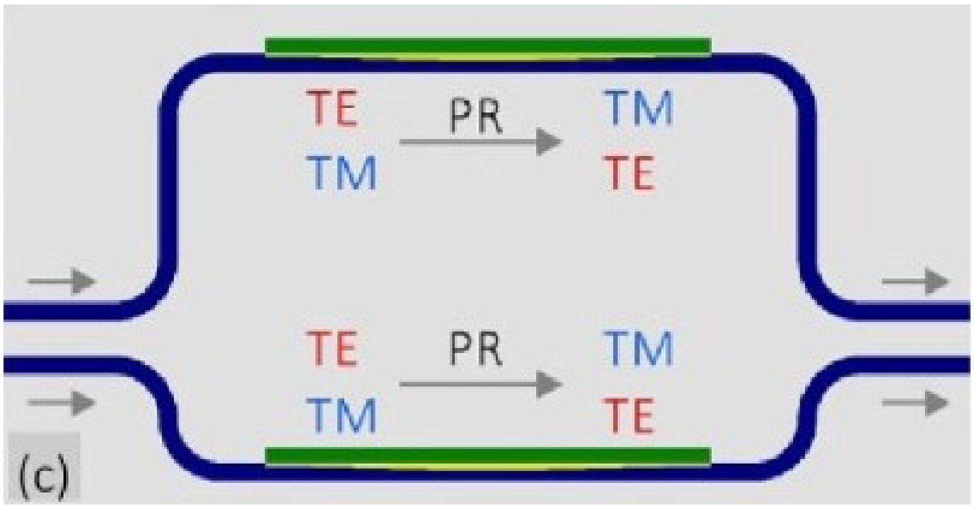

.

Fig. 2.13: Schematic of phase shifter with PRs [98]

2.4.5 Polarization Insensitive Optical Switch

Silicon waveguides achieve high compactness for optical devices by exploiting the high confinement factor due to the high refractive index contrast between Si (3.48) and SiO_2 (1.444). On the other hand, they introduce a significant polarization dependence for silicon photonic devices, including polarization mode dispersion, polarization-dependent loss (PDL), and polarization dependence of the operating wavelength, which is one of the remaining major challenges.

Thus, the optical switch based on SOI with a 220 nm thick Si layer is only designed for one specific polarization (TE/TM). Efforts have been made to minimize PDL, either through polarization diversity approaches [100, 101] or by making the components' polarization insensitive [91]. To realize the polarization insensitive optical switch, polarization-diversity technology is a promising choice. Based on this technology, 2×2 [100], 4×4 [102], and 8×8 [103] optical switches have been demonstrated. However, polarization diversity technology requires double the switching resources making the system more complex. A 2×2 thermo-optic polarization insensitive MZI switch consists of two MMI couplers [57]. In [104], a thermo-optic switch based on a symmetric directional coupler is designed with polymer materials. In [105], an optical switch using phase change material is demonstrated. Finally, a polarization insensitive MEMS switch based on couplers is reported in [106]. A polarization-insensitive MZI-based optical switch that works for TE and TM modes is schematically illustrated in Fig. 2.14 [57].

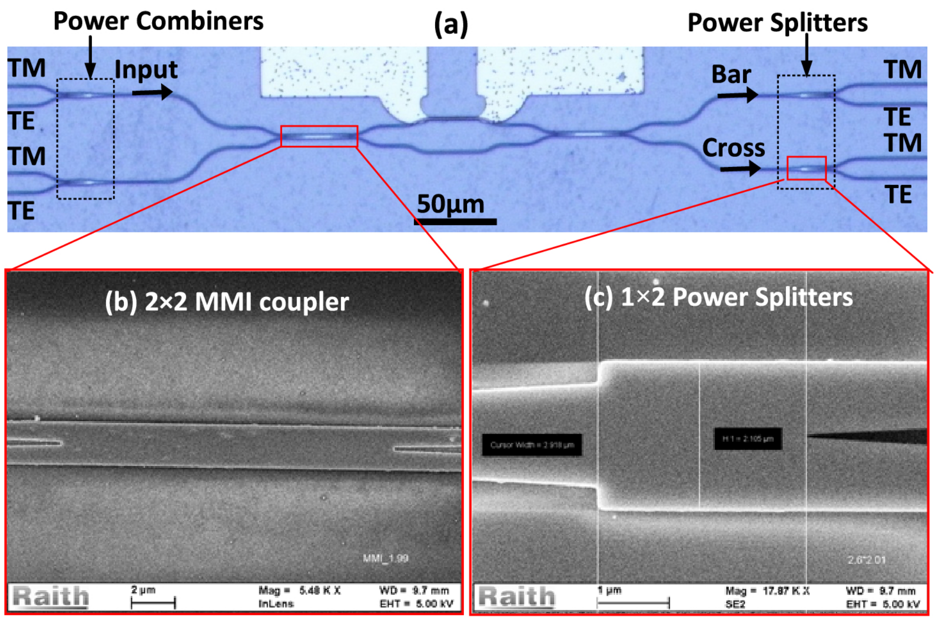

.

Fig. 2.14: (a) Microscope picture of the fabricated MZI based optical switch; (b) SEM picture of the 2 × 2 3-dB MMI coupler; (c) SEM picture of the 1 × 2 power splitter [57]

The performances of polarization-insensitive optical switches are summarized in Table 2.7. In the last five years, the performance of polarization-insensitive optical switches has been improving, and the table shows that MZI and DC based optical switches can decrease the device size. The MEMS structure sacrifices the device size but significantly improves the extinction ratio performance.

Table 2.7: Performance comparison for reported polarization insensitive switches.

Reference	Year	L [µm]	IL [dB]	XT [dB]	BW [nm]	Modes	Structure	E/S
[57]	2018	44.4	4	20	100 (C Band)	TE_0 TM_0	MZI	E
[104]	2019	22.5	10.2	12	40 (C Band)	TE_0 TM_0	DC	E
[105]	2021	160	1.37	13.5	100 (C Band)	TE_0 TM_0	DC	E
[106]	2016	300	1.2	60	100 (C Band)	TE_0 TM_0	MEMS	E

*L, Length; IL, Insertion Loss; ER, Extinction Ratio; BW, Bandwidth; E, Experiment; S, Simulation.

2.5 Key Building Blocks for PDM-MDM SiPh Optical Interconnects

Multiplexing technology provides optical interconnect systems with up to a hundred times the data throughput of the original base. As a result, these structures that can integrate WDM, MDM, and PDM into an integrated system have received much attention. Fig. 2.15 illustrates the working principle of an hybrid multiplexing system. All building blocks in this system need large bandwidth to achieve multiplexing of different wavelength bands.

WDM, MDM, and PDM are implemented by wavelength multiplexer, mode multiplexer, and polarization rotator, respectively. The hybrid signals that propagate in the multimode waveguide are demultiplexed in the reverse process.

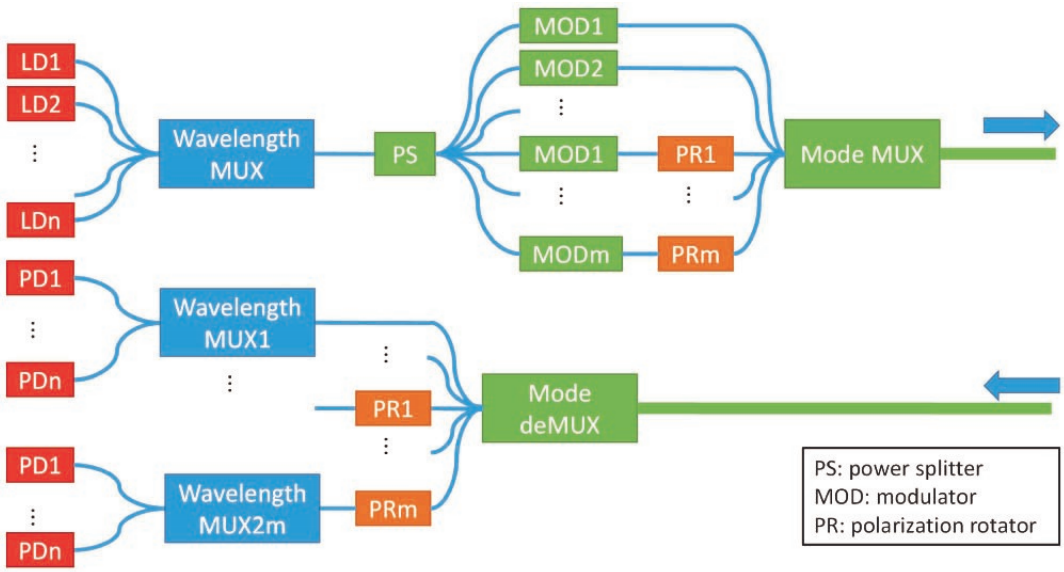

Fig. 2.15: Schematic diagram of integrated interconnect system hybrid multiplexed by WDM, MDM, and PDM [107].

2.5.1 The Polarization/Mode Hybrid (de)Multiplexers

The polarization/mode hybrid (de)multiplexers are able to handle multiple mode channels with dual polarizations. One straightforward scheme is to directly cascade the two groups of ADCs designed for TE and TM modes, respectively, as illustrated in Fig. 2.16.a [45]. However, the crosstalk is relatively high. This problem can be addressed by exploiting the cascaded adiabatic ADCs, as shown in Fig. 2.16.b [36].

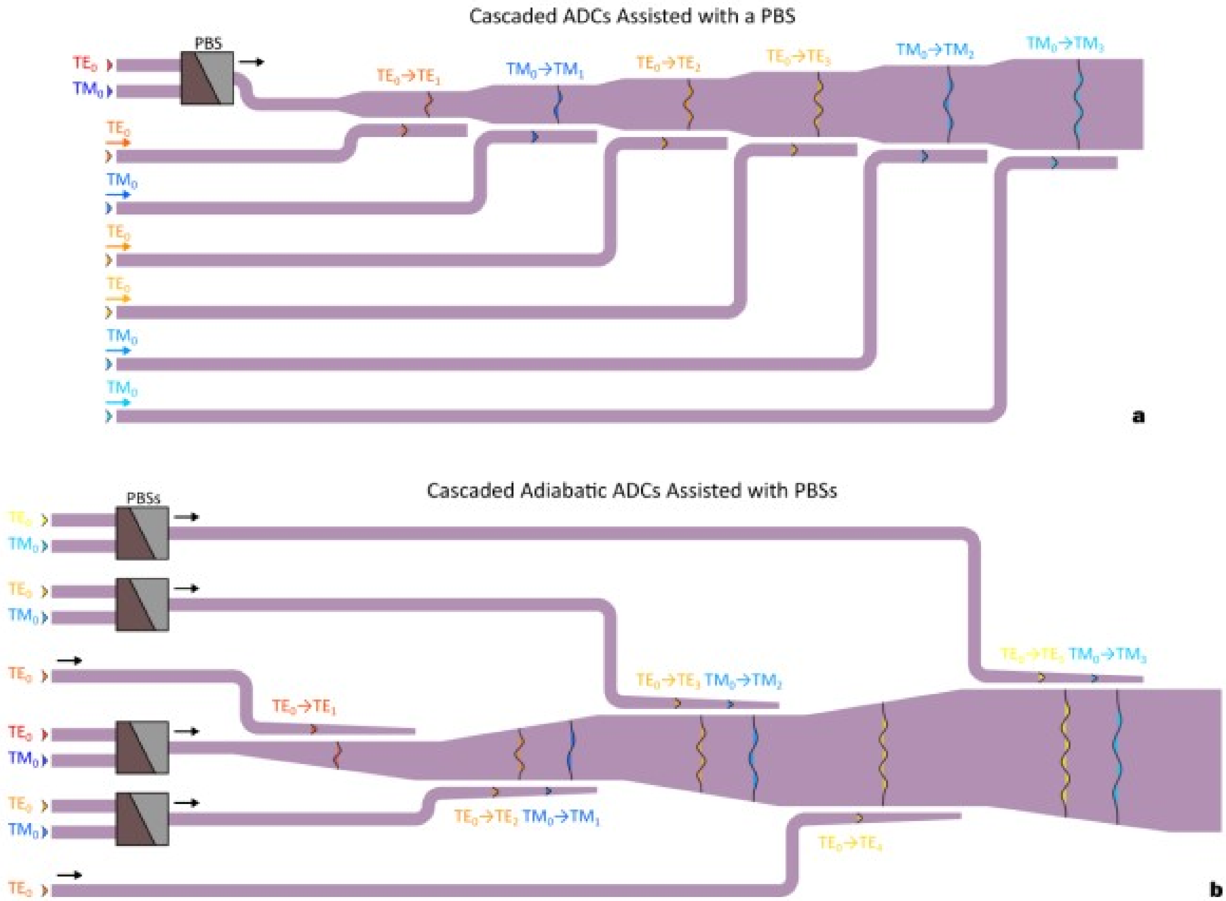

Fig. 2.16: The schematics for the silicon polarization/mode hybrid (de)multiplexers based on (a) cascaded ADCs [45] and (b) cascaded adiabatic ADC [36].

A design integrating multiplexer and PBS for six modes designed using a silicon nitride-loaded lithium niobate on an insulator (LNOI) platform [108]. Furthermore, 10 channels mode multiplexers including PR are also fabricated and measured in [36, 109]. Table 2.8 summarizes the reported silicon polarization/mode hybrid (de)multiplexers. As we can see, the PDM-MDM multiplexer can transmit up to 10 channels, and the ADC structure is the only structure currently available for this function.

Table 2.8: polarization/mode hybrid (de)multiplexers.

Reference	Year	L [µm]	IL [dB]	XT [dB]	BW [nm]	Modes	Structure	E/S
[88]	2021	700	1.49	-13	40 (C band)	TE_0-TE_3 TM_0-TM_1	ADC	E
[89]	2018	200	1.8	-15	90 (C band)	TE_0-TE_5 TM_0-TM_3	ADC	E
[36]	2018	74.75	0.78	-11.4	100 (C band)	TE_0-TE_4 TM_0-TM_4	ADC	E
[24]	2013	336	3.5	-20	120 (C band)	TE_0-TE_3 TM_0-TM_3	ADC	E

*L, Length; IL, Insertion Loss; XT, Crosstalk; BW, Bandwidth; E, Experiment; S, Simulation.

2.5.2 PDM-MDM 3-dB Coupler

3-dB couplers that work for both TE and TM fundamental modes have also been demonstrated using MMI based on Subwavelength Grating (SWGs) structures [90], silicon bent directional couplers [91], and asymmetrical Mach-Zehnder Interferometer (MZI) [92]. However, an optical coupler that works for both MDM and PDM still remains to be proposed and experimentally validated. By using a shallow etching process, a 3-dB splitter that works for the first three TE modes and one TM mode has been experimentally demonstrated based on a 300 nm-thick SOI [60]. This thesis reports on its experimental validation of this structure and improved the IL, XT performance.

2.5.3 WDM-PDM-MDM Optical Switch

To further improve the transmission capacity, a 2×2 MDM-WDM optical switch is reported to accommodate eight signal channels (2 modes $\times$ 4 wavelengths) in the input and output ports [70]. However, the XT between different modes limits the scalability of MDM-WDM switches. Thus, PDM is considered in conjunction with MDM-WDM. In [110], a WDM-MDM-PDM optical switch is first proposed and fabricated which requires 2 modes $\times$ 2 polarizations $\times$ 3 wavelengths MRRs. Fig. 2.17 illustrates the switching architecture for mode polarization and wavelength multiplexed signals based on MRRs. MDM, PDM, and WDM signals are injected from input ports and demultiplexed into fundamental mode signals by a mode demultiplexer and polarization beam splitter (PBS). Each signal is propagated in an individual channel and then switched to the output port by a 1×2 MRR. The routed signals are combined at the output by a mode multiplexer and a polarizing beam combiner (PBC). The wavelength multiplexing, switching, and mode multiplexing functions can be realized simultaneously by a tunable add-drop MRR. For this system, four modes (TE0, TE1, TM0, TM1) are injected into the input port. Using the demultiplexer and the PBS, the modes with different orders and different polarization states are converted into fundamental modes. All fundamental modes are passed through ring-based tunable switches, to achieve wavelength multiplexing and demultiplexing. The MMI coupler can be used to achieve power splitting. PBS combined with the multiplexer can also achieve mode multiplexing. The fundamental modes are finally converted into four order modes which are the same as the input. The measured insertion loss is below 9.4 dB, and the largest crosstalk is -11.3 dB over 40 nm bandwidth ranging from 1525 nm to 1565 nm.

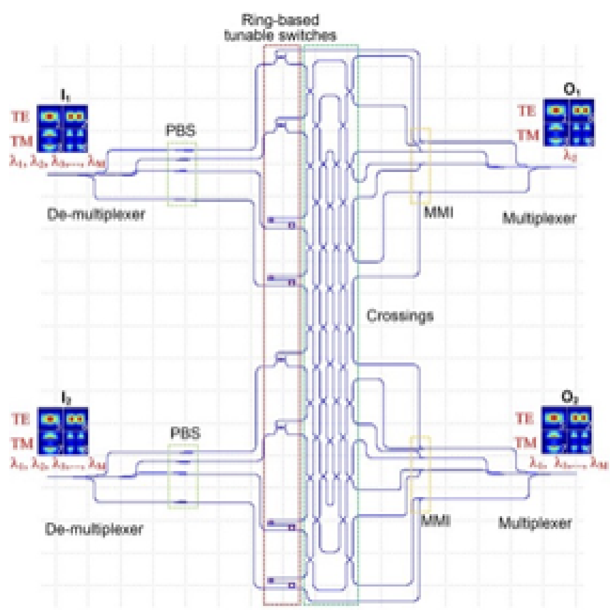

Fig. 2.17: Schematic configuration of the proposed silicon 2 × 2 mode-polarization-wavelength selective switch (MPWSS). As an example, the TE0, λ_2 and TM0, λ_2 channels of I1 and the TE1, λ_2 and TM1, λ_2 channels of I2 are routed to O1, and other channels are routed to O2 [110].

2.6 PDM-MDM Multimode Crossings

Various complex optical interconnection links will be implemented as a result of the rapid advancement of optical interconnection technology. Compared with circuit interconnection, optical waveguide interconnection has a unique feature, that is, it allows two or more multiple waveguide crossings on the same plane. Compared to electronic interconnected circuits, the optical waveguide crossing structure permits greater wiring flexibility on the optical printed plane, thereby enhancing the wiring density and complexity. Consequently, the research on multimode waveguide crossing has important application value.

MDM multimode waveguide crossings for either TE or TM are well-developed as a result of the development of MDM technology. Due to the refractive indices and optical power distributions between mode orders, waveguide crossings for single mode cannot be directly transferred to higher order modes. With the help of a mode splitter, the combined multiple modes can be separated into distinct propagation paths, allowing the single-mode waveguide crossing to be utilized in each optical path. Consequently, the multimode crossings for TE modes are demonstrated using MMI [111] and Y-branch structures [112]. For the PDM waveguide crossings, the highly structured birefringence of the SOI platform introduces a considerable effective refractive index difference and unbalanced performance of TE and TM polarisation in the previously proposed silicon waveguide crossing design. For the MMI silicon waveguide crossing design, the length of the MMI section is primarily determined by the optical beat length in relation to the effective refractive index of the optical mode. Unfortunately, the beat lengths for TE and TM polarisation are different, a trade-off needs to be made by extending the device length to achieve good transmission performance with dual polarisation, as shown in Fig. 2.18 [113].

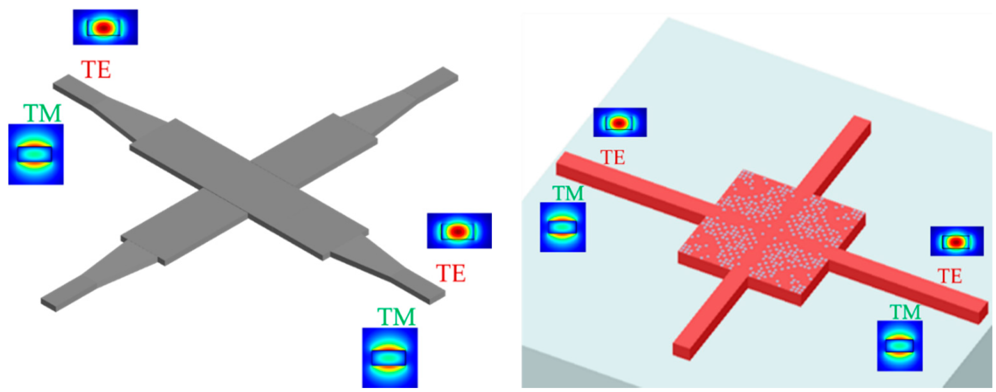

(a) (b)

Fig. 2.18: (a) Schematic of the polarization-multiplexed MMI silicon waveguide crossing; (b) top view of the polarization-multiplexed inverse-designed silicon waveguide crossing [113].

The research on PDM-MDM multimode crossings is still needed to be completed. Nonetheless, there is an MMI based multimode crossing for TM modes. This structure works for the first two TM modes (TM_0 and TM_1), as shown in Fig. 2.19. The same MDM crossing design is available for both TE0 and TE1 modes [113]. The largest measured insertion loss for the four modes (TE_0, TE_1, TM_0, TM_1) is 0.73 dB coming from TM_0, and the greatest crosstalk is approximately -35 dB.

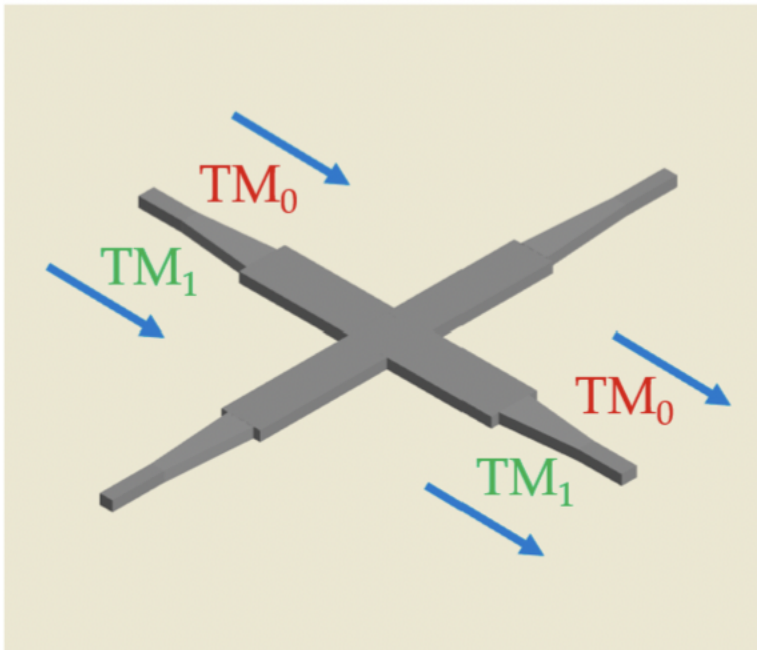

Fig. 2.19: top view of the mode-multiplexed silicon waveguide crossing with multimode interference structure for fundamental transverse-magnetic (TM_0) and first-order transverse-magnetic (TM_1) mode [113].

2.7 PDM-MDM Phase Shifter

As a fundamental control unit of an optical switching system, the optical phase shifter is one of the primary research areas in optical interconnection systems, optical signal processing, and silicon photonics. The predominant working mechanism of the current silicon-based optical waveguide phase shifters is to achieve phase modulation by modifying the effective refractive index of the waveguide structures. The phase shifter made of silicon is an important device. By changing the refractive index of the waveguide, it is possible to the control of the phase of the light wave, thereby enabling the functional modulation of the chip. The main silicon-based phase shifters in common use today are electro-optical phase shifters, thermo-optical phase shifters and nano-opto-mechanical phase shifters, among which thermo-optical phase shifters have received much attention due to their simplicity of fabrication, higher modulation efficiency, larger bandwidth. The main research directions for thermo-optical phasers are: 1. lower power consumption which can be achieved by reducing the wasted heat of surrounding materials [114] or taking advantages of power multiplexing [115]. 2. Lower loss and higher modulation speed which can be achieved by doping the same carrier on both sides [116].

The thermo-optical phase shifter relies on the thermo-optical effect of silicon materials. Due to the high thermo-optical coefficient, changing the temperature to change the optical properties of silicon waveguides is an important part of thermo-optical modulation. This is especially applicable for low-cost and low-frequency modulation, which are both very desirable. Silicon has a high thermo-optical coefficient of approximately 1.8×10^{-4} K^{-1} at room temperature, so that only a small temperature increase is required to achieve a significant change in waveguide refractive index. At the same time, the thermal conductivity of silicon is approximately 149 W/mK, a property that ensures that silicon-based thermo-optical phase shifters can have a quick response time, with switching times typically falling within a few tens of microseconds.

MDM optical switches are composed of two 3-dB couplers to build an MZI structure. A

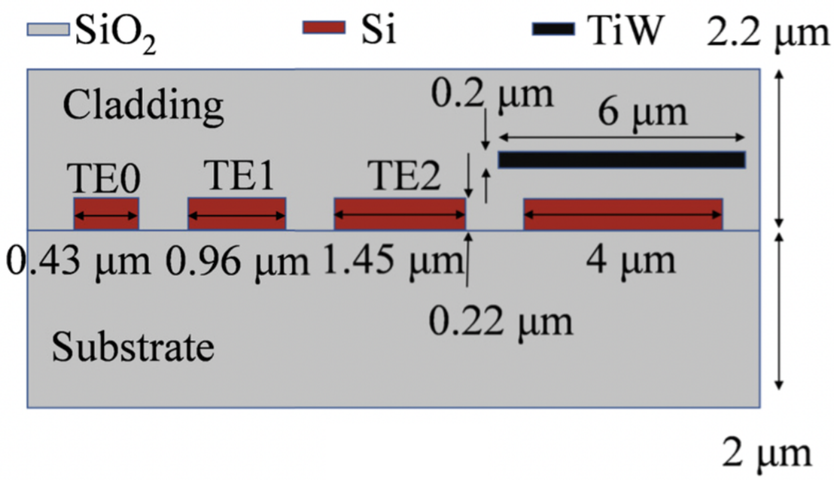

Fig. 2.20: Cross section of the fundamental mode (TE0), two-mode (TE0, TE1), and three-mode (TE0, TE1, and TE2) waveguides and phase shifter [117].

mode insensitive phase shifter is added in one of the two waveguide arms. By controlling the on/off state of the phase shifter, multimode switches are able to switch payload data between different spatial channels exploiting orthogonal optical modes. The main challenge of mode insensitive phase shifters is balancing different propagation constants of different modes. The design of the mode insensitive phase shifter is still under investigation. Our group has demonstrated a mode insensitive phase shifter for the first three TE modes with excellent performance [117] shown in Fig. 2.20. Through the simulation results discussed in [117], the change in the rate of the effective index with respect to the local temperature (d_{neff}/dT) converges toward almost the same value for the three different TE modes by increasing the phase shifter width. When the waveguide width exceeds 4 μm, the difference between the values of the d_{neff}/dT for the first three modes is small enough to be disregarded.

The high energy consumption of silicon photonics devices severely restricts their applicability. Currently, optimizing techniques typically impose constraints only on the device geometry and require many optimization iterations to converge to a compact size. As discussed in [118], more efficient energy constraints are promising to be achieved by invoking topology-based inverse design methods. Based on the mode insensitive phase shifter designed for three TE modes [117], topology-based inverse design methods hold promise for achieving more efficient energy constraints [66]. This design has been enhanced in three main aspects. 1. A tradeoff between mode insensitivity and high tuning efficiency. 2. A more accurate description of the temperature independence by defining an equivalent tuning efficiency as the rate of phase change with respect to the temperature change (dφ/dT). 3. A lower power consumption by optimizing the metal heater width above the phase shifter. As shown in Fig. 2.21, in order to eliminate the mode dependence of the tuning efficiency of the phase shifter, an inverse designed compact ME was inserted to maintain exact same phase shift in all modes with low insertion loss and modal crosstalk. The mode insensitive phase shifter is intended for the first two TE modes with improved tuning efficiency and decreased power consumption. The ME in the middle of the phase shifter transfers the input TE_0 and TE_1 modes, ensuring that both modes experience the same total phase accumulation.

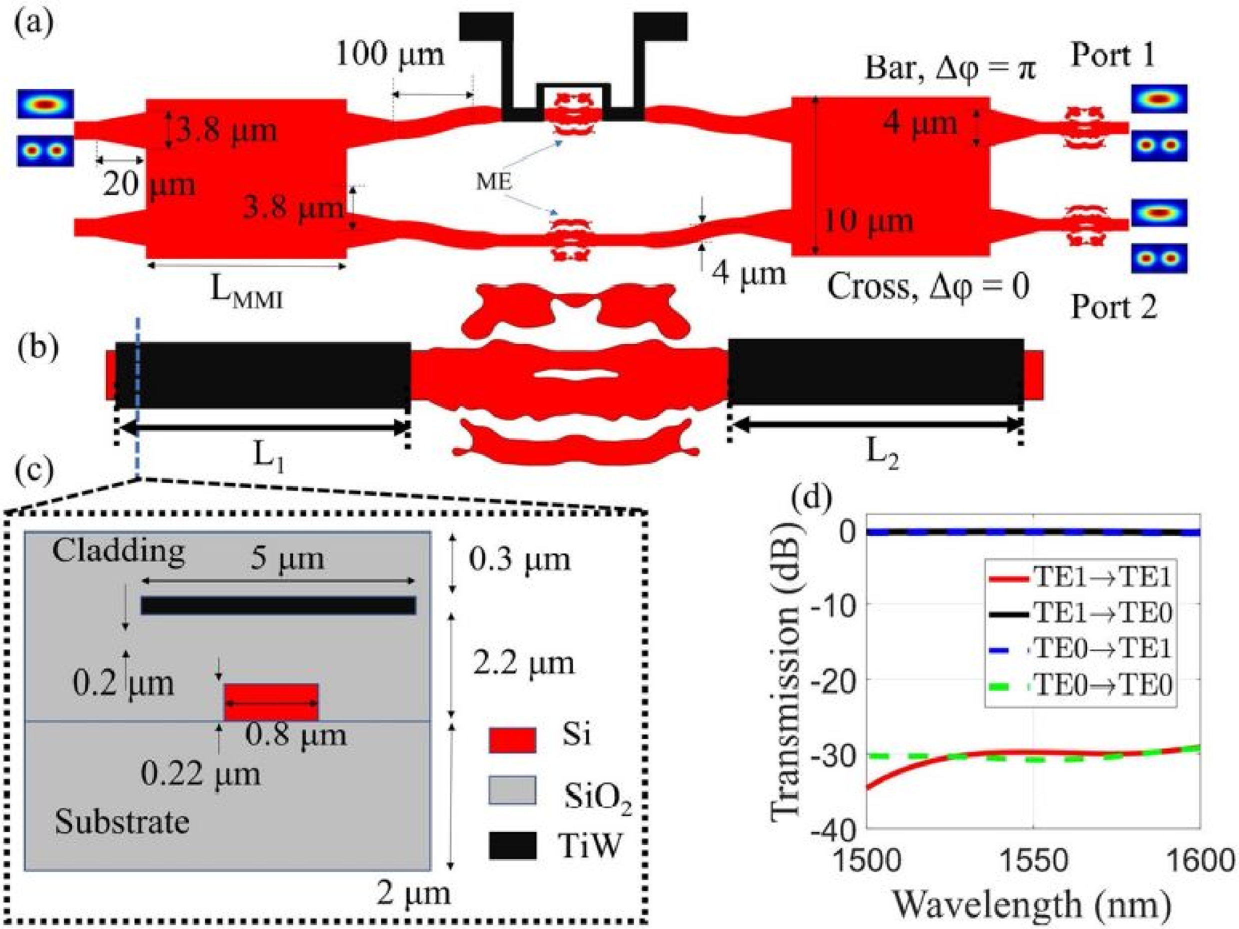

Fig. 2.21: (a) Schematic of the proposed mode insensitive switch; (b) Schematic of the proposed mode insensitive phase shifter; (c) Cross-section of the phase shifter; (d) Simulated transmission spectrum of the inverse designed ME [66].

Nevertheless, the structure illustrated in [117] is only designed for TE modes. Based on the large effective indices difference between TE and TM modes, these phase shifters are typically polarization sensitive and only for one specific polarization state. A promising method for polarization-diversity technology is presented in order to realize polarization-insensitive phase shifters [100]. In addition, a polarization-insensitive thermo-optic switch is experimentally validated in [57] as illustrated in Fig. 2.22. A polarization-insensitive phase shifter based on 340 nm $\times$ 340 nm square silicon nanophotonic waveguides have been introduced in this design with good experimental performance. Besides, as shown in Fig. 2.23, the design separates the propagating waveguide of TE and TM modes to two channels using PBS and PBC [119]. Thus, we could use our mode-insensitive phase shifter designed for either TE or TM modes in each channel separately. Furthermore, another possible implementation of polarization-mode insensitive phase shifter is proposed in this section. Implementing a subwavelength grating (SWG) structure based on a design proposed and validated by our group [117]. We have found that for the same polarization state (either TE or TM), dn_{eff}/dT of different mode orders converges to a specific value as the phase shifter width increases [117] as shown in Fig. 2.24. However, the converging value is different for TE and TM modes. Specifically, dn_{eff}/dT of TM is smaller than TE modes because TM modes have a field that exhibits more overlap with the oxide. The thermo-optic coefficient of oxide is one order of magnitude smaller than that of Silicon as shown in Fig. 2.25 [120]. Fig. 2.26 shows a method to adjust the value of dn_{eff}/dT. By implementing the SWG structure and adjusting its parameters, it is possible to decrease the dn_{eff}/dT value of TE modes and increase the value of TM modes, and finally make them converge to a specific point. Thus, the polarization-mode insensitive phase shifter can be realized.

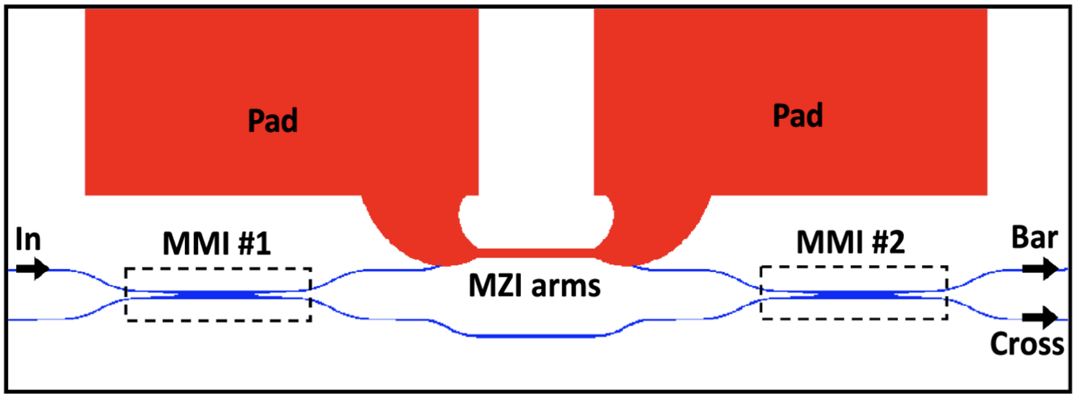

Fig. 2.22: Schematic configuration of the thermo-optic switch [100].

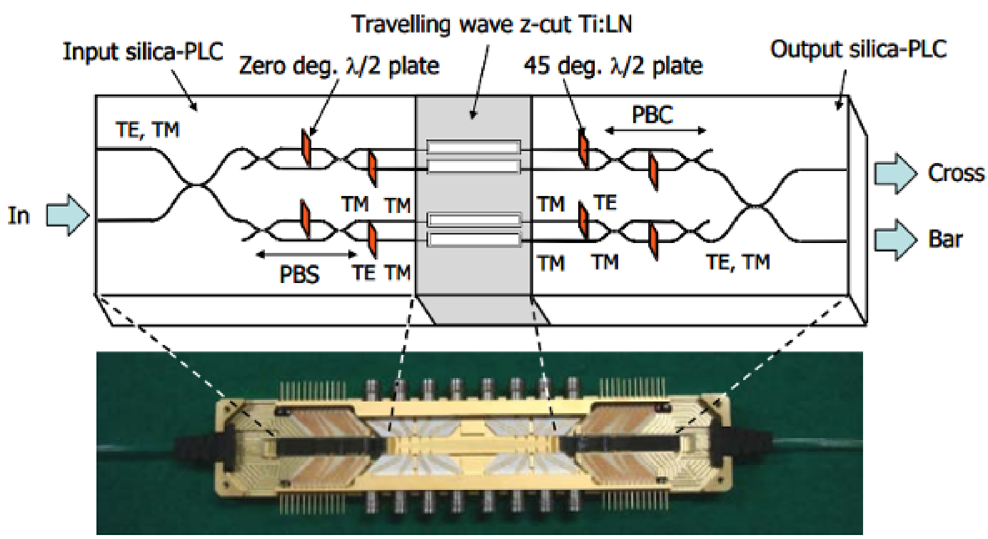

Fig. 2.23: Schematic configuration of a polarization-insensitive Mach-Zehnder interferometer consisting of an LN phase shifter array and silica-based PLCs with integrated polarization beam splitter/combiners [119].

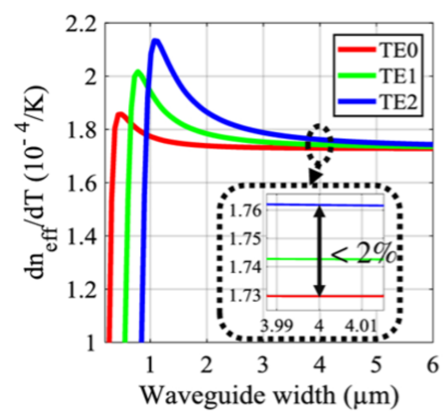

Fig. 2.24: Simulated dn_{eff}/dT as a function of the phase shifter width for the first three TE modes [117].

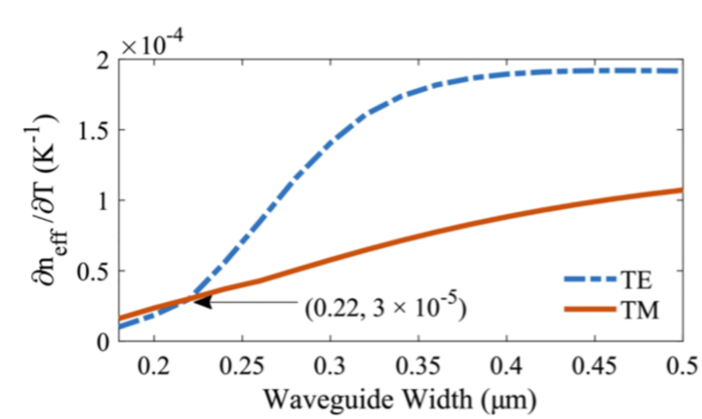

Fig. 2.25: dn_{eff}/dT as functions of waveguide width for the TE and TM modes at 1550 nm wavelength [121].

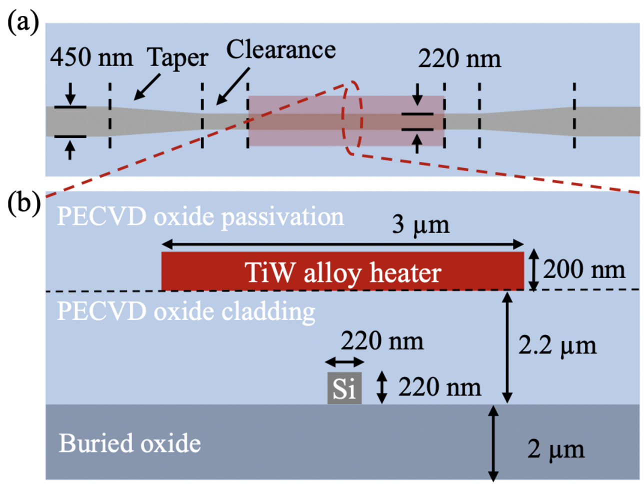

Fig. 2.27: (a) Top-down view of the phase shifter; (b) cross-section view of the structure in the dashed circle labeled in (a) (not to scale).

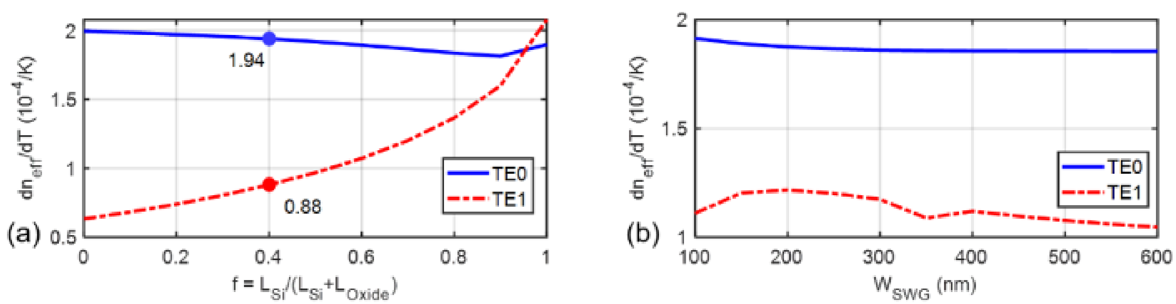

Fig. 2.26: (a) Thermo-optic coefficient versus duty ratio for a mode sensitive TOPS with W_{SWG} = 500 nm. (b) Thermo-optic coefficient versus W_{SWG} for f = 0.7 [120].

Recently, a polarization-insensitive thermo-optic switch is reported in [121]. The top and cross section view of the phase shifter is illustrated in Fig. 2.27. In this design, waveguides with a cross-section of 220 nm × 220 nm are utilized for polarization independence. The insertion loss of this phase shifter is calculated to be less than 1 dB over the 100 nm bandwidth ranging from 1500 nm to 1600 nm.

A polarization and mode insensitive phase shifter based on the free carrier dispersion effect is demonstrated in [122]. Currently, there are three main structures for phase modulation based on the free carrier dispersion effect: MOS capacitors, forward biased PIN junction diodes and reverse biased PN junctions. Our group developed a single mode phase shifter based on a forward-biased PN junction for achieving high switching speed. Compared to the conventionally adopted PN junction structure, a forward-biased PN junction structure is used for shortening the length of PN junction [123]. The Cross-sectional view of the phase shifter is shown in Fig. 2.28.

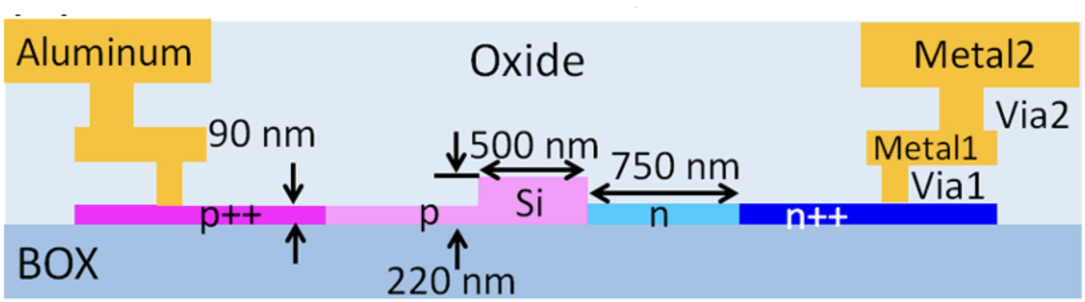

Fig. 2.28: A phase shifter based on a lateral PN junction [123].

However, phase shifter modulation based on PN junctions is generally inefficient, necessitating longer device lengths to achieve π phase difference. Of the three structures based on carrier dispersion effect modulation, the modulation efficiency based on the forward pin structure is substantially higher than the other two types. A trench pin structure is designed for accommodating the first two TE and TM modes (TE_0,TE_1,TM_0,TM_1) as shown in Fig. 2.29. This is the first mode and polarization insensitive phase shifter which has already been experimentally validated.

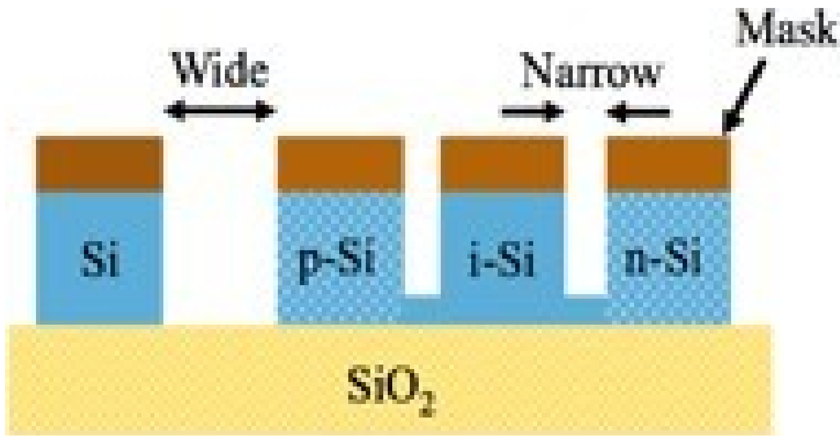

Fig. 2.29: PIN trench structure [122].

PIN is a special structure in which the intrinsic layer is located between a heavily doped p-type layer and a heavily doped n-type layer. As the resistivity decreases as impurities increase and vice versa, the p and n layers have relatively low resistivity, whereas the I layer has relatively high resistivity. The PIN-PS can be easily integrated with other optical components because of its simple component formation. The carrier plasma effect induces an optical phase shift when a forward bias is applied to a Si pin diode, causing a large number of free-carries to congregate in the intrinsic region. Due to the fact that both PIN and conventional PN phase shifters use the carrier plasma effect to create an optical phase shift, the amount of electric charge required for the same optical modulation is comparable between these two types of phase shifters. However, due to a significantly larger capacitance, even when operated with a small voltage swing produced by a high-speed CMOS inverter-type driver, PIN-PS is capable of producing a larger optical phase shift. Among various etching processes of Si pin, a trench pin structure is used to simplify the fabrication process into a single-step dry-etching process. According to work [123], Titanium-tungsten (TiW) metal heater is utilized as a phase shifting element due to its high melting point and high resistivity, which prevents electro-migration incidence at a higher temperature. To realize a pin structure, a two-step dry etching process is needed. As the open space size decreases, the silicon etching rate decreases. The illustration of wide and narrow open spaces when digging a trench structure is shown in Fig. 2.29. In addition, the remaining amount of the Si-layer bridge between the p-doped region and the waveguide, as well as the n-doped region and the waveguide, is depicted for narrow open spaces. Thus, the pin structure is realized by this technique.

2.8 Conclusion

Multimode waveguides can propagate orthogonal modes simultaneously, increasing channel capacity by the number of corresponding modes. Both MDM and PDM have the potential to increase the flexibility and functionality of SiPh. MDM has been widely demonstrated for increasing channel capacity by the number of supported modes. While MDM components can leverage either TE or TM spatial-modes, simultaneously using both modes is challenging. Indeed, most MDM methods are polarization-sensitive, with deviations from ideal polarization resulting in a significant crosstalk. However, the development of multimode waveguide and recent SiPh polarization-diversity circuits have enabled on-chip

MDM-PDM systems. This chapter summarized the development of multiplexing technology, from the rise of mode-division multiplexing technology to the evolution of polarization state multiplexing in order to increase the transmission capacity, and finally the development of the combination of PDM-MDM technology. Additionally, switching and routing of data signals are basic optical signal processing functions required for reconfigurable PDM-MDM optical networks. A 3-dB coupler is the primary building block of the optical switch for power splitting and combining. Thus in the following chapters, we experimentally demonstrate a mode/polarization insensitive 3-dB coupler and propose two optical switches that works for PDM-MDM system. Besides, the multimode crossings as well as polarization and a mode insensitive phase shifter are discussed for the implementation of PDM-MDM switching system.

Chapter 3

PDM-MDM 3-dB Coupler

In this chapter, we provide the design details and experimentally demonstrate a four-mode polarization/mode insensitive 3-dB coupler based on an adiabatic coupler. The proposed design works for the first two TE modes and the first two TM modes. The 3-dB coupler was fabricated using an electron-beam lithography (EBL) by Applied Nanotools Inc. (ANT) and characterized in our lab. Over an optical bandwidth of 70 nm (1500 nm to 1570 nm), the coupler exhibits at most 0.7 dB insertion loss with a maximum crosstalk of -15.7 dB and a power imbalance not worse than 0.9 dB.

3.1 Design and Working Principle

The proposed four-mode dual polarization 3-dB coupler is based on the design first proposed in [60], showing large operating bandwidth and optimized simulation performance. However, in this study, an SOI wafer with a 300 nm-thick silicon core layer is considered as a fabrication platform that is not satisfied by most conventional fabrication processes. Besides, the minimum waveguide gap distance for this structure is 50 nm, which is difficult to achieve because the minimum fabrication limit is controlled above 60 nm. The main benefit is the fabrication process. The promotion is mainly from two aspects: 1. The thickness changed from 300 nm to 220 nm. The typical thickness of waveguide of a silicon optical chip is 220 nm. Therefore, the processing technology under this waveguide thickness is relatively mature and the loss is smaller. In addition, other components designed in the system also use 220 nm as the waveguide thickness, which makes the system have better processing matching. The main benefit is about the fabrication process. The promotion is mainly from two aspects: 1. The thickness changed from 300 nm to 220 nm. The typical thickness of waveguide of silicon optical chip is 220 nm. Therefore, the processing technology under this waveguide thickness is relatively mature and the loss is smaller. In addition, other components designed in the system also use 220 nm as the waveguide thickness, which makes the system have better processing matching. 2. Rib waveguide is replaced by a slab waveguide as the waveguide construction. Thus, single etch is used instead of shallow etch for manufacture. The cost is lower, and the fabrication process is simpler. The device length and accommodating modes number are the main drawbacks of this alteration. Larger width and propagation length are required for TM coupling in the narrower waveguide. Moreover, the higher TM modes (like TM_3 and TM_4) is not stable enough to be accommodated by the narrower waveguide, which results in increased insertion loss. In other words, for the design of four-mode devices, the increase of device size caused by narrow waveguide is acceptable. The 220 nm waveguide thickness is more suitable in terms of processing expense and general system homogeneity. Finally, the proposed work only provides simulation results that do not take the fabrication loss into consideration. Our ability to perform validation lacks. Fig. 3.1 illustrates the working principle of the PDM-MDM circuit with the main building blocks.

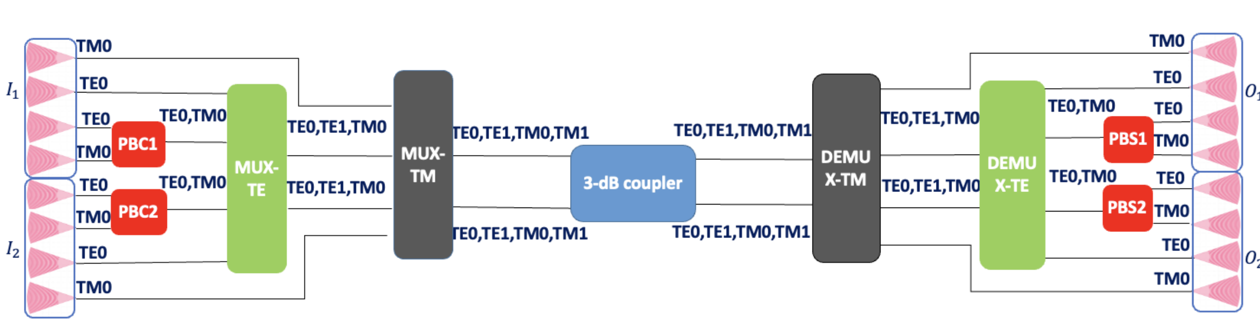

Fig. 3.1: Schematic of the PDM-MDM circuit.

The PDM-MDM circuit has two input ports (I_1 and I_2) and two output ports (O_1 and O_2) and consists of PBC and PBS, (de) multiplexer, and the optimally designed 3-dB coupler. At the input ports, vertical grating couplers excite either TE or TM fundamental mode at the input of the waveguide. After being combined through the PBC, both the TE and the TM fundamental modes propagate in the same waveguides to the TE and TM multiplexers. After going through the multiplexers, the four modes (TE_0, TE_1, TM_0, TM_1) are generated to evaluate the 3-dB coupler. At the output of the 3-dB coupler, the TM and TE demultiplexers and the PBS structures transform the higher order modes back to fundamental modes for off-chip photodetection.

The top view layout of the 3-dB coupler is schematically shown in Fig. 3.2. Note that the dimensions are not to scale. This PDM-MDM 3-dB coupler consists of an adiabatic coupler (AC) of length L_1 and two S-bend waveguides over a length L_2. The idea of adiabatic transition in the field of integrated photonics was first defined in [124]. The AC does not require a precisely defined critical power-transfer length leading to smaller wavelength and polarization dependencies compared to other interference-based couplers. The adiabatic coupler works by converting the input mode in a single waveguide into an even or odd supermode over two waveguides separated by a small gap (Gap_{AC}). From the adiabatic tapering process, therefore, one input mode can be fully converted into its corresponding supermode at the output ports.

When the four input modes (TE_0, TE_1, TM_0, and TM_1) enter the coupler from the narrower waveguide of width W_1, they convert to odd supermodes while they convert to even supermodes when entering through the wider waveguide of width W_2. An even supermode consists of two in-phase modes, each confined in one of the two waveguides while the mode profiles in both waveguides remain similar to the input mode profile. In contrast, the odd supermodes contain two anti-phase parts. For all input modes, their profile is evenly distributed across the two output waveguides of width W_3 realizing the 3-dB optical power splitting.

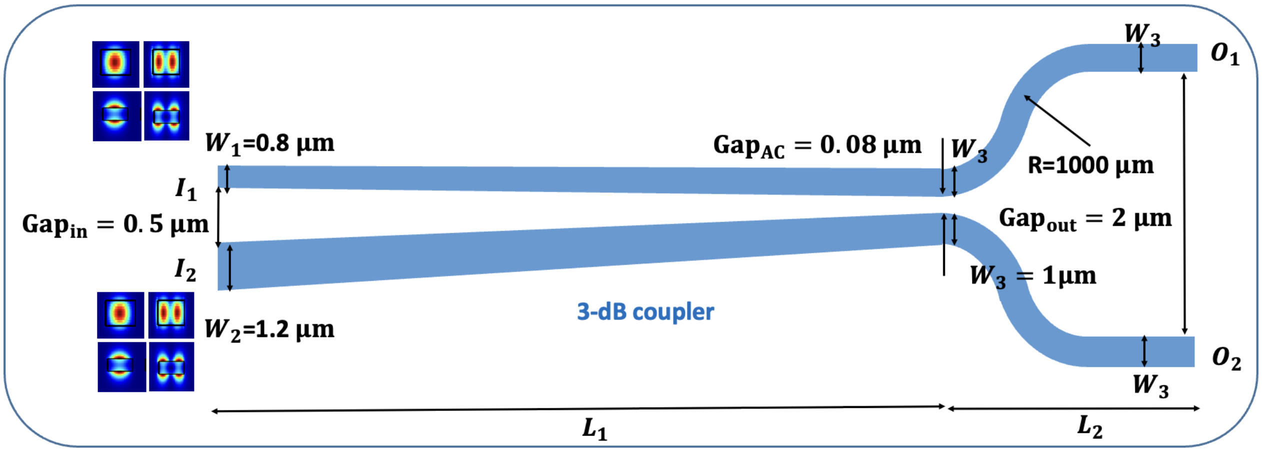

Fig. 3.2: Layout schematic of the PDM-MDM 3-dB coupler design (dimensions not to scale).

At the input and output of the coupler, two polarizations (TE and TM) and their respective higher order modes (TE_1 and TM_1) are enabled by the polarization beam combiners and splitters (PBC/PBS) (Fig. 3.3) and two adiabatic coupler–based mode multiplexers (Fig. 3.4). The working principle of PBS/PBC structure is explained in detail in Section 2.4.1. We validated the function of this design through simulation and experiment. The simulation results are similar to the ones shown in [85] (Fig. 3.3).

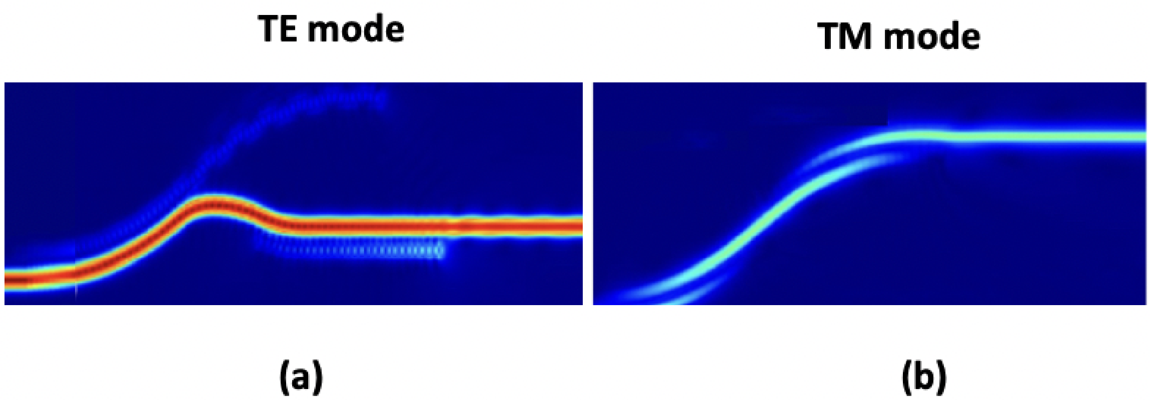

Fig. 3.3: Light propagation of the PBS structure (a) TE modes; (b) TM modes.

Devices building blocks were studied and reported by [36] where they were designed for a dual-polarization 10-channel mode (de)multiplexer on an SOI platform. Besides, the structural parameters of the TE multiplexers were optimized by our group [117]. As such, we reused these designs in our work. The parameters of the TM mode multiplexer were optimized based on the work demonstrated in [36]. In this work, we decrease the gap between the waveguides for stronger coupling leading to shorter coupling length. The narrowest waveguide gap is specifically narrowed from 0.5 µm to 0.1 µm to match the TE multiplexer's gap. As TE and TM multiplexers are connected to build an entire PDM-MDM structure. Two multiplexers with different gap structures have different output spacing. Thus, we need to add S-bend waveguides to satisfy the height difference between them. However, if the two gaps are the same, straight waveguides can be used instead of S-bend to reduce the transmission loss. Besides, the mode has a better transmission with a smaller gap as it contributes the stronger coupling effect. Afterwards, the device length is optimized for transmission using ANSYS/Lumerical FDTD solutions. As shown in Fig. 3.4, based on a tapered DC, the TE and TM mode multiplexers parallel-couple a narrow silicon waveguide (0.81 µm for TE and 0.78 µm) to a wide tapered waveguide (0.96 µm for TE and 1.15 µm) respectively. The multiplexer structure has four input ports with different waveguide widths, and fundamental modes excited by different arms will terminate in a different order. For example, the fundamental modes from the top and bottom waveguides are transformed into first order modes while the fundamental modes in the middle arms retain their mode order.

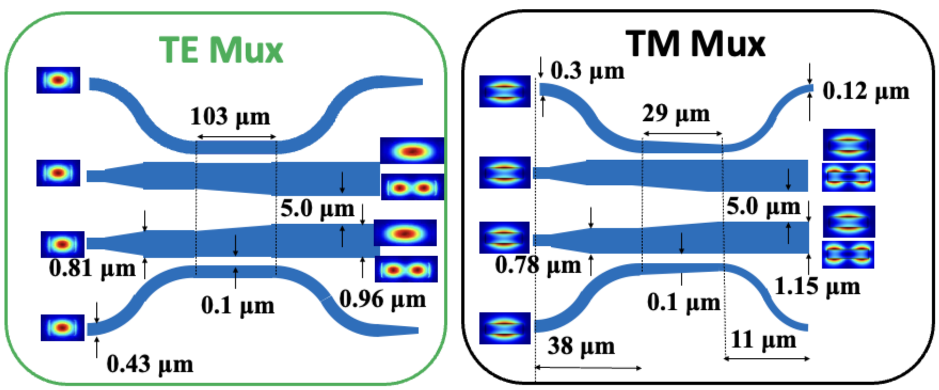

Fig. 3.4: Schematic of the mode multiplexer for TE mode and for TM mode.

3.2 Optimization and Simulation Results

The adiabatic coupler in Fig. 3.2 is first optimized by an eigenmode expansion (EME) method using ANSYS/Lumerical MODE solutions. The optimization is based on transmission with respect to propagation length. We optimized the width values (W_1, W_2,

W_3) and the adiabatic coupler lengths (L_1, L_2) for the lowest insertion loss (IL) and lowest modal crosstalk (XT) performance. For a PDM-MDM device, low crosstalk between modes is required to ensure proper operation. In the AC part, the modal crosstalk mainly comes from mode coupling between waveguides. The most direct solution to this problem is to ensure that the effective refractive index difference between modes is significantly large by optimizing the width of the waveguide. The device is designed for a 220 nm waveguide thickness SOI chip for fabrication at Applied Nanotools (ANT) in Alberta, Canada. Fig. 3.5 shows the simulated effective index as a function of the waveguide width. To support four modes, W_1 and W_2 should be larger than 800 nm. To support all four modes, the output waveguide width (W_3) is set to 1 µm. Based on Fig. 3.5, the effective index of TE_0 mode remains constant for waveguide width greater than 1.5 µm. The TM_1 mode only emerges for a width larger than 800 nm since its effective index is close to the silica cladding (1.44) for narrower width. Indeed, mode TM_1 only propagates if the effective index difference is sufficient relative to the cladding material. As such, a width of 0.8 µm is the cut-off condition for TM_1.

We set the upper limit of W_1 and W_2 to 1.2 µm to avoid excitation of higher order modes. For some waveguide widths, the effective index of one mode may correspond to another mode which leads to modal crosstalk. A more considerable width difference ensures that the effective index difference is sufficiently large to reduce modal crosstalk and, thus, coupling between the two waveguides.

The gap between the two input waveguides starts at 500 nm (Gap_{in}) and then gradually decreases to 80 nm (Gap_{AC}) as the waveguides taper to a width of 1 µm (W_3). Gap_{in} is set as 500 nm to make a trade-off between coupler length and coupling power. The asymmetric adiabatic coupler with varying widths (narrow waveguide W_1= 800 nm, and larger waveguide W_2=1200 nm) performs the optical power splitting. At the output of the coupler, two identical S bends of width W_3 (1000 nm) efficiently separate the output ports by 2 mm avoiding any further optical field overlapping. It is worthwhile to note that this design could be used to process higher order modes by increasing the waveguide width (W_1 and W_2) and the length of AC.

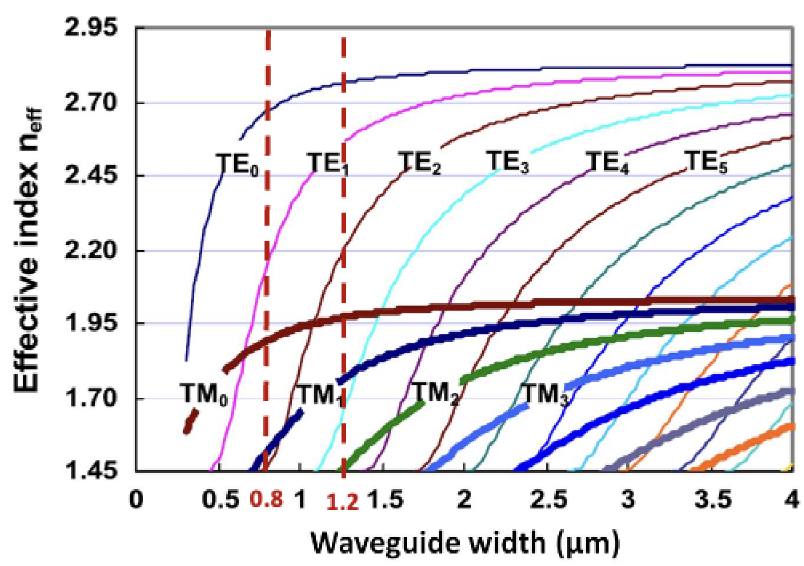

Fig. 3.5: Simulated effective index of TE and TM modes in a 220 nm thick silicon waveguide as a function of waveguide width.

Fig. 3.6 shows the coupling strength of the adiabatic coupler as a function of the gap between two waveguides. As expected, the coupling strength between the two waveguides decreases as the gap increases as the field overlaps less and less. The coupling strength converges after 500 nm which corresponds to the Gap_{in}. Thus, Gap_{in} is set as 500 nm. The gap at the output, Gap_{AC}, should be as small as possible to reduce propagation loss while meeting fabrication limitations. Gap_{AC} is set to 80 nm. The S-bend radius is 1000 µm to reduce loss. Indeed, Fig. 3.7 shows the effect of bend radius on the bend loss for TE and TM modes. The increase in bend radius reduces loss. Beyond 1000 µm, the bend loss converges to a low value of 0.1 dB for TE polarization and 0.2 dB for TM polarization.

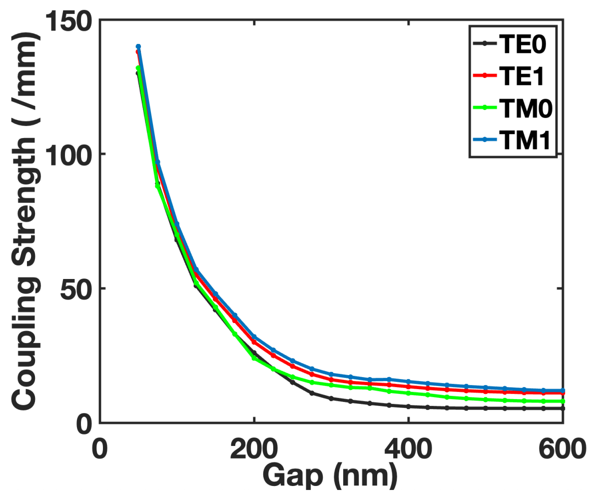

Fig. 3.6: Simulated coupling strength in a 220 nm thick silicon waveguide as a function of gap.

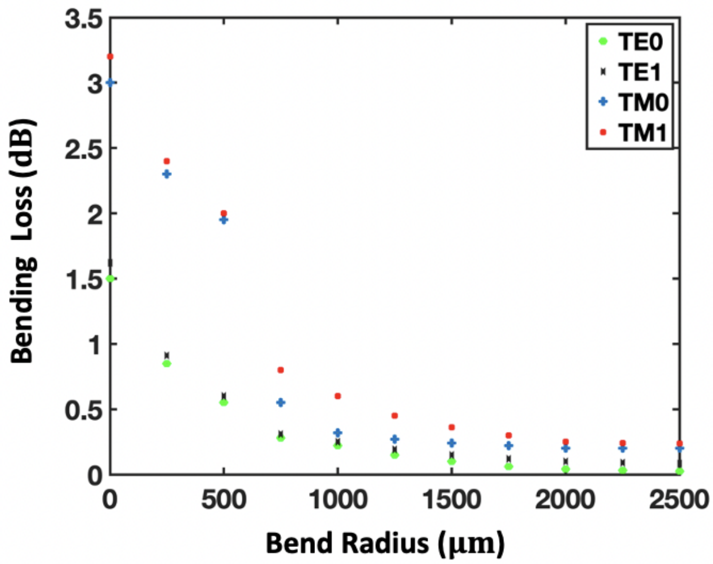

Fig. 3.7: Simulated bend loss as a function of bend radius for TE and TM modes.

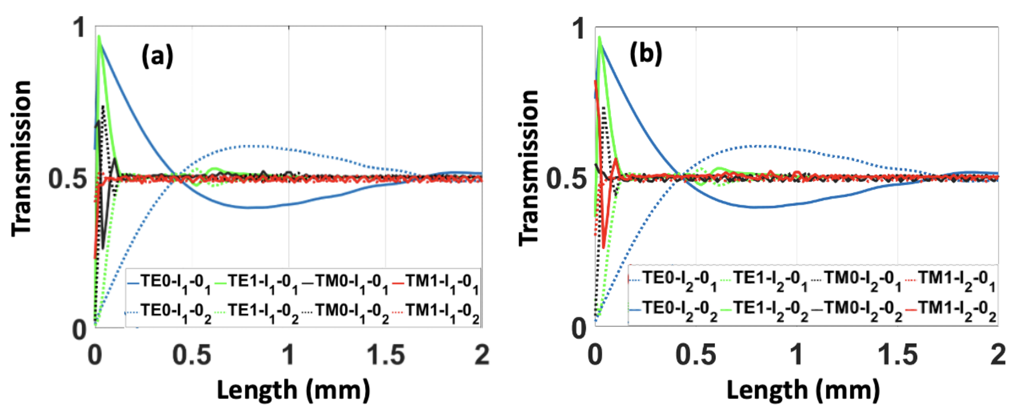

Fig. 3.8: (a) Normalized transmission for all four modes as a function of length (L_1) for (a) input port I_1 and (b) input port I_2.

The adiabiatic directional coupler has an adiabatically tapering structure that divides the optical input mode into its corresponding supermodes (odd or even) at the two output arms as first suggested in [60]. The gap between the input waveguides goes from 500 nm to 80 nm. For the determined widths and gaps, Fig. 3.8(a,b) show the normalized transmission in linear scale from input ports I_1 and I_2 to output ports I_1 and I_2 as a function of the ADC length L_1 (Fig. 3.8). It can be observed that as the length increases, the transmission at output O_1 decreases while the optical power at output O_1 increases for all the four modes. For the other three modes (TE_1, TM_0 and TM_1), their transmissions converge for shorter length. Indeed, the fundamental mode, TE_0, requires extended coupling length as its field distribution is strongly confined leading to weaker coupling efficiency. The fundamental mode needs a length of 1.6 mm to achieve an even distribution of the odd and even modes. Thus, the PDM-MDM 3-dB coupler length is determined by its lowest order mode (TE_0). A similar situation can be observed for the transmission from input port I_2 in Fig. 3.8(b). The length of the AC is optimized to 1.6 mm with a trade-off between the device length and conversion efficiency. Through a similar design methodology as for length L_1, L_2 is optimized to 60 µm for better transmission with an S-bend radius R of 1 mm to reduce bending loss and mode crosstalk. The normalized transmission as a function of the value of L_2 is shown in Fig. 3.9 .

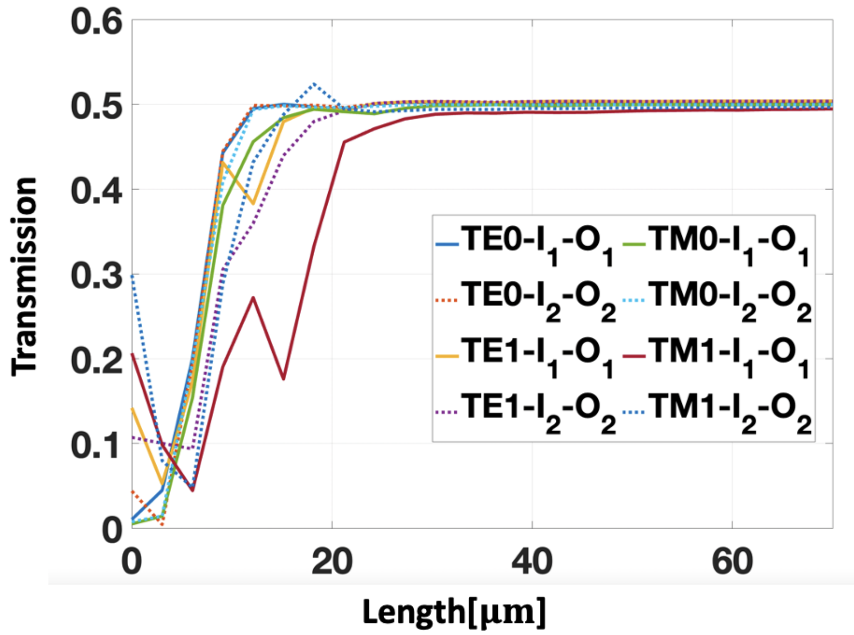

Fig. 3.9: Normalized transmission of L_2 in the PDM-MDM 3-dB coupler.

The simulated mode propagation for the overall 3-dB coupler structure for the four modes with the transmission value of O_1 and O_2 are shown in Fig. 3.10. All four input modes are split evenly at the two output ports with a nearly 50 % optical power splitting ratio. The corresponding mode profiles at the output ends of the coupler are also included. The power transmission at the output port reflects the performance parameters of the 3-dB coupler, including insertion loss and power imbalance, which are consistent with the simulation results shown below.

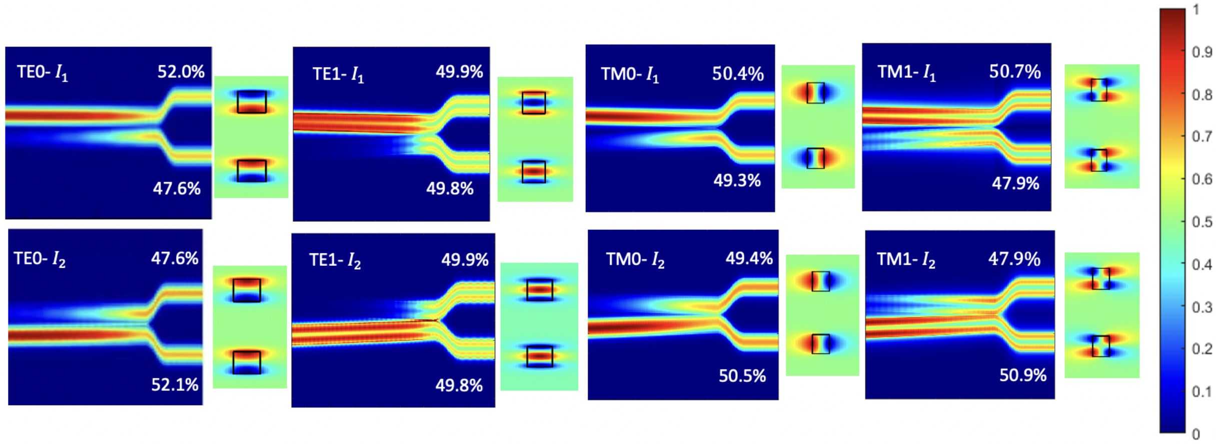

Fig. 3.10: Simulated mode propagation for the PDM-MDM 3-dB coupler at 1550 nm for the four modes (TE_0, TE_1, TM_0, and TM_1) launched at the input port I_1 or I_2. The output intensity field distribution is shown.

The insertion loss (IL), modal crosstalk (XT), and power imbalance (PI) are the three main parameters used for optimizing the coupler and are calculated using Eq. (3.1) - Eq. (3.3).

$$IL = -10 \times \log \frac{\mathrm{P}_{out_1} + \mathrm{P}_{out_2}}{\mathrm{P}_{in}} \tag{3.1}$$

$$PI = -10 \times \log \frac{\mathrm{P}_{out_1}}{\mathrm{P}_{out_2}} \tag{3.2}$$

$$XT = -10 \times \log \frac{\sum_{1,j\neq i}^{4} \mathrm{P}_{out-mode_j}}{\mathrm{P}_{out-mode_i}} \tag{3.3}$$

where P_{out_1} and P_{out_2} are the optical power at the output ports O_1 and O_2. P_{in} is the optical power launched in one of the two input ports, I_1 or I_2 (Fig. 3.3). Take the ith input mode as an example, $\mathrm{P}_{out-mode_i}$ is the total optical power of ith mode over both output ports and $\sum_{1,j\neq i}^{4} \mathrm{P}_{out-mode_j}$ is the sum of the optical power at the output ports from all other modes that were unintentionally converted from mode i. Fig. 3.11 describes the simulated performance of the 3-dB coupler including IL, XT, and PI over the 100 nm bandwidth ranging from 1500 nm to 1600 nm.

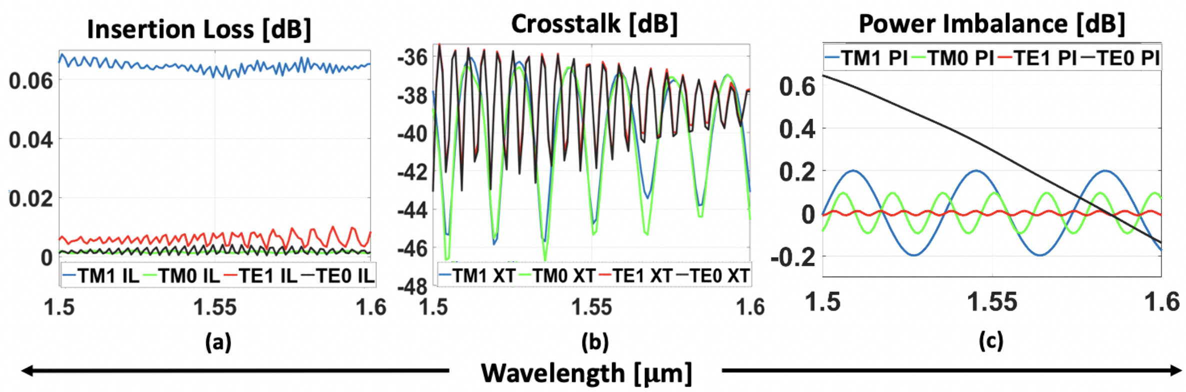

Fig. 3.11: Simulated performance of the 3-dB coupler over 100 nm optical bandwidth from 1500 nm to 1600 nm. (a) Insertion loss in dB; (b) modal crosstalk in dB; (c) power imbalance in dB.

In the simulation, TM1 exhibits the largest insertion loss (0.07 dB) which occurs at 1500 nm. The 3-dB coupler exhibits less than -35 dB of crosstalk for the four modes over 100 nm. The power imbalance varies between -0.2 dB to 0.6 dB within the same optical bandwidth range.

3.3 Experimental Setups

The design was fabricated by Applied Nanotools Inc. (ANT). The silicon device layer is patterned using a 100 KeV electron-beam lithography (EBL) followed by an inductively coupled plasma-induced reactive ion etching (ICP-RIE) process. A 2.2 µm thick SiO_2 cladding is deposited by plasma-enhanced chemical vapor deposition (PECVD). The GCs can either be TE or TM designed with similar structure but different parameters. The design of GCs are from the SiEPIC EBeam PDK library which is designed for ANT fabrication. An optical microscopic image is shown in Fig. 3.12 labeled with all the corresponding structures, including the 16 grating couplers (GCs) which correspond to the four modes at the two input and two output ports.

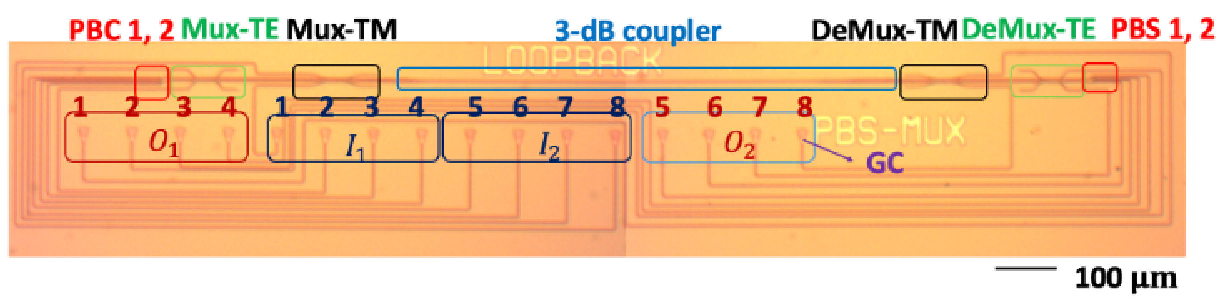

Fig. 3.12: Optical image of the 2 × 2 MDM system which includes the PBC, PBS, TE and TM (de)multiplexers, and PDM-MDM 3-dB coupler.

The two PBCs and two PBSs transform modes between TE and TM. The four (de)multiplexers enable higher mode generation. The 3-dB coupler is in the middle. For continuous wave (CW) measurements, a tunable C-band laser is first regulated to a specific polarization status (TE or TM) by a polarization controller (PC) and injected into the chip via one GC. On the output side, light is first coupled by another GC to a fiber. The optical output is measured by an optical power meter (FPM-8200 by manufacturer Artisan Technology Group) which delivers precise optical power measurement from 800 nm to 1600 nm with over 75 dB of dynamic range. The power meter is an important device for measuring transmission performance (including insertion loss and crosstalk) and is capable of accurately measuring the power of light. The power meter used in the experiments has a resolution of up to 0.01 dB. Two different GCs were used to excite TE or TM modes since GCs are polarization sensitive. To experimentally test both TE and TM modes simultaneously, test structures corresponding to all the building blocks, i.e., the PBC/PBS and the (de)multiplexers for TE and TM modes, are first measured to obtain their inherent insertion loss and modal crosstalk performance. The worst measured values for these test structures for their IL and modal crosstalk are 0.9 dB and -15.4 dB, respectively, over the wavelength range from 1500 nm to 1570 nm. As shown in Fig. 3.12, when light is launched from any one of the input ports (GCs labeled 1-8 in blue colour), TM_1, TE_1, TM_0, TE_0, TM_0, TE_0, TM_1, TE_1 are excited, respectively. Similarly, for the output ports (GCs labeled 1-8 in red colour). TM_1, TE_1, TM_0, TE_0, TM_0, TE_0, TM_1, TE_1 are detected by the optical power meter, respectively. We can only excite one input port and one output port at a time in the measurement. When we choose the same mode order ($\text{Input}_{GC_1} \rightarrow \text{Output}_{GC_1}$, I_1-O_1 : TM_1 - TM_1 for example), that is how we evaluate the IL performance.

After normalizing to the I_1-O_1 : TM_1 - TM_1)transmission curve of the test structure, the IL values are obtained (Fig. 3.17). When the mode orders are different between the input and output ports ($Input_{GC_1} \rightarrow Output_{GC_{2-4}}$, I_1-O_1 : TM_1 - TE_1, TM_1 - TM_0, TM_1 - TE_0), the measurement curves indicate the XT performance as well, i.e., the transmission from one optical mode to another optical mode. These transmission curves are normalized to the input mode straight-through case (I_1-O_1 : TM_1 - TM_1) as a reference to show the XT value. The XT is labeled with a vertical arrow in the first spectrum of Fig. 3.16 for clarification. All measurements are normalized to loopback structures which consist of a waveguide length varying from 176 µm to 1115 µm and two GCs. In the design, 12 GCs were designed, ranging from a waveguide connecting GCs 1-9 to a waveguide connecting GCs 4-5. Consequently, this permits normalization according to various structures. Fig. 3.13 shows the loopback structure drawn in klayout.

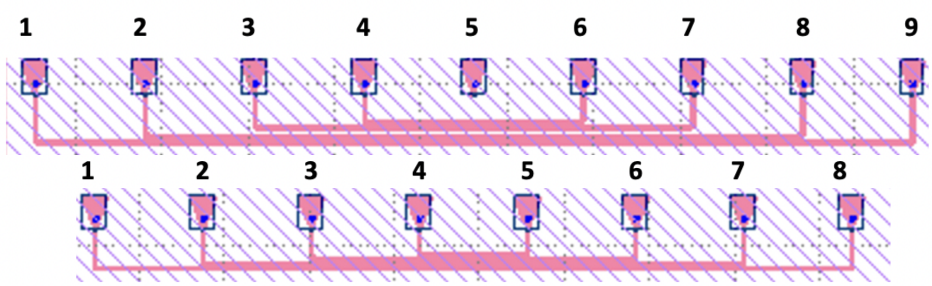

Fig. 3.13: Loopback structure in Klayout.

Fig. 3.14 shows the measurement results of the loopback structure. The propagation loss of TE and TM GCs are -10.4 dB and -16.2 dB at the wavelength of 1520 nm, respectively. As we can see from Fig. 3.14, the measurement spectrum shows prominent Fabry-Perot fringes for wavelengths larger than 1570 nm. These fringes, which have approximately 2 nm free spectral range (FSR), result from the cavity generated in-waveguide reflection between the two grating couplers. The characterization is limited by these fringes to wavelength from 1500 nm to 1570 nm.

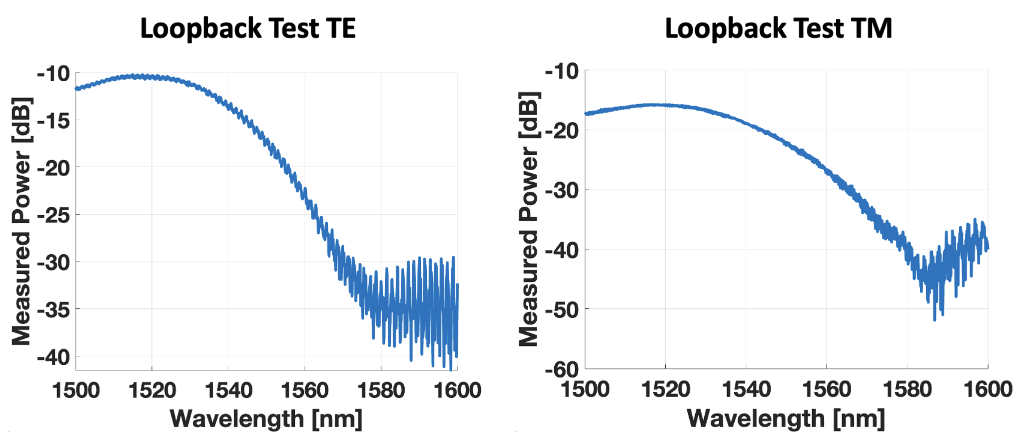

Fig. 3.14: Loopback measurement result for TE and TM GCs.

3.4 Measurement Results

Fig. 3.16 shows the corresponding measured and normalized spectrum for the four modes through the coupler. The PDM-MDM 3-dB coupler is defined by its two input ports by two output ports (2×2). Thus, for each mode, there are four diagrams showing the transmission from 1) the upper input to the upper output ($\mathrm{I}_1 \rightarrow O_1$), 2) the upper input to the lower output ($\mathrm{I}_1 \rightarrow O_2$), 3) the lower input to the upper output ($\mathrm{I}_2 \rightarrow O_1$), and 4) the lower input to the lower output ($\mathrm{I}_2 \rightarrow O_2$). To test both the TE and TM modes simultaneously, test structures corresponding to the PBC/PBS and the (de)multiplexers for TE and TM modes are tested to obtain their insertion loss and modal crosstalk (Fig. 3.15). We can conclude from Fig 3.15 that the worst values of the test structure IL and modal crosstalk measured are -0.9 dB and -15.4 dB, respectively.

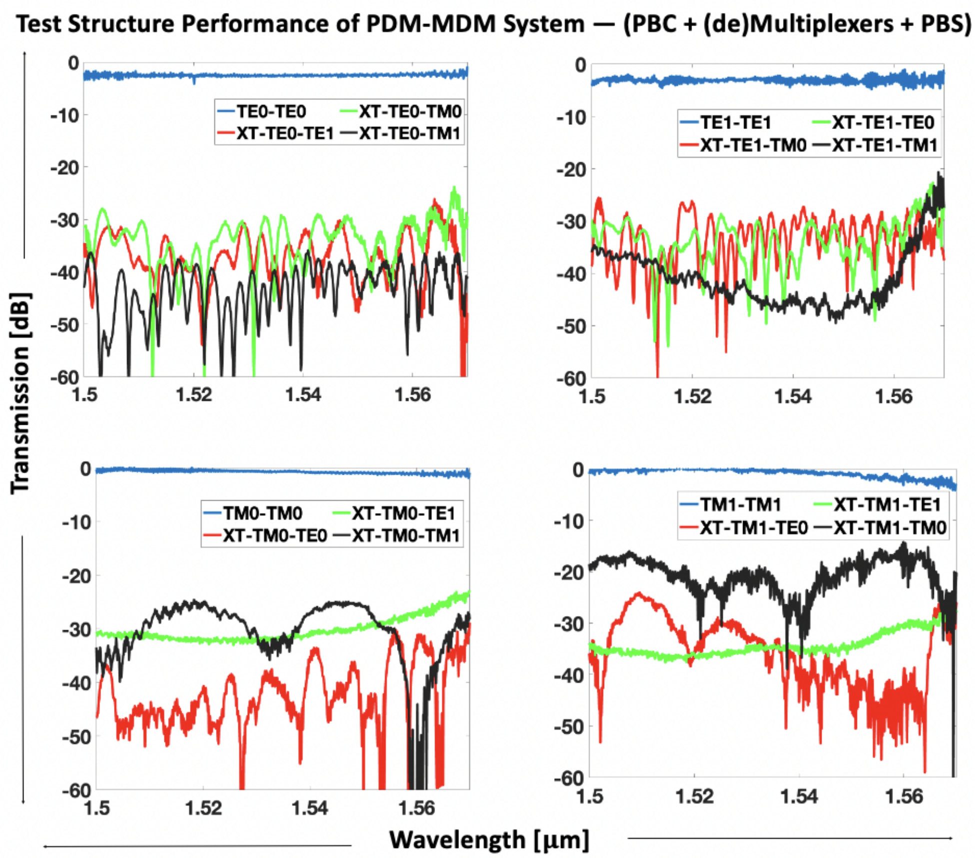

Fig. 3.15: Measured transmission spectrum as a function of wavelength for the test structure (including PBS/PBC and (de)Multiplexers).

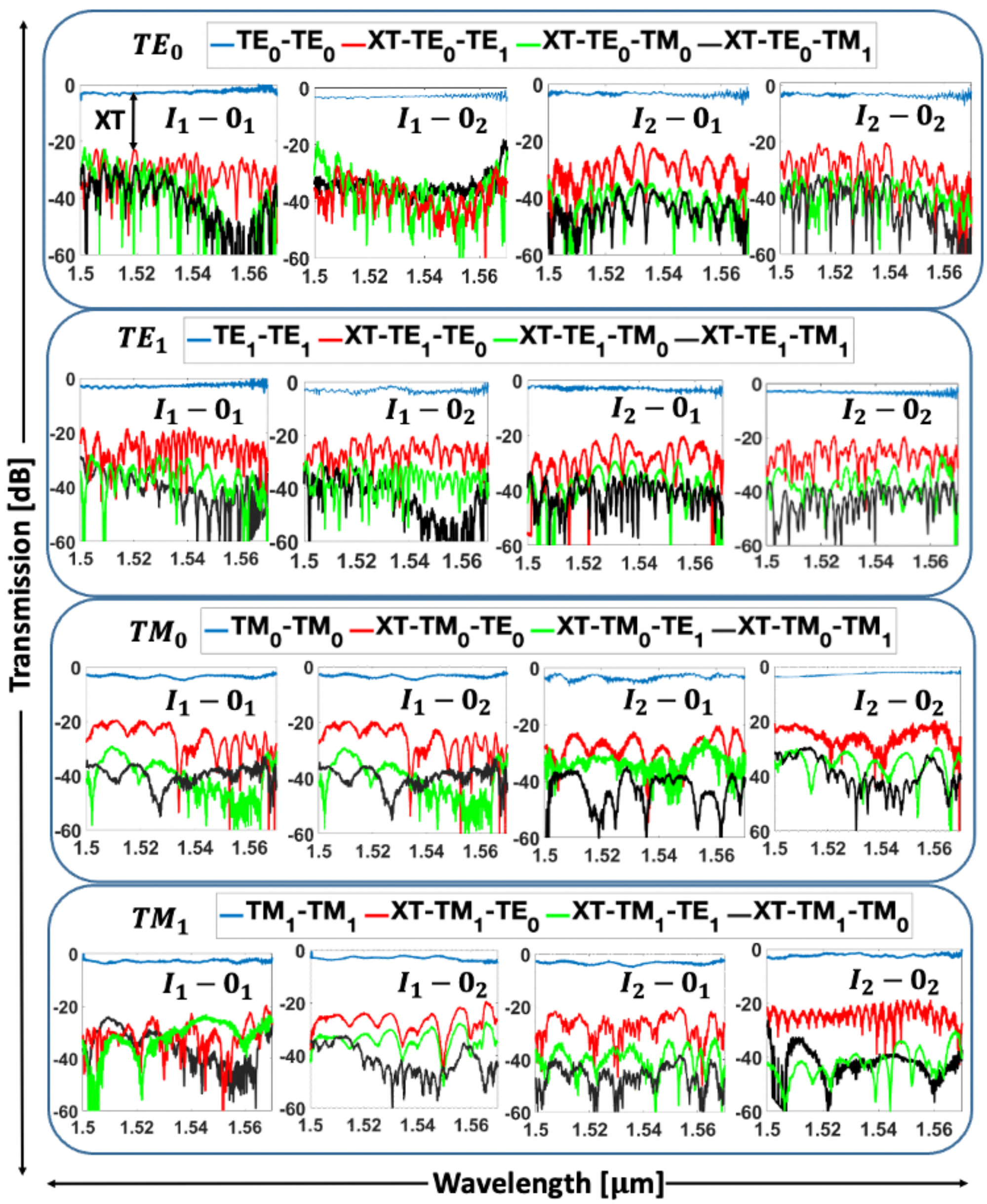

Fig. 3.16: Measured transmission spectrum as a function of wavelength for the PDM-MDM 3-dB optical coupler.

Fig. 3.17 shows the transmission curves of the 3-dB splitting. Measurement results below 1570 nm are presented as the measurement spectra showed prominent Fabry-Perot fringes for wavelength larger than 1570 nm. These fringes come from the cavity generated by in-waveguide reflection between the two grating couplers which was also observed by our previous measurement [125]. It is worth noting that the grating coupler used in this work is provided by the ANT PDK [126]. According to the test results, the 3-dB bandwidths of the GCs are 30.6 nm (TE) and 47.5 nm (TM) around the central wavelength of 1550 nm. Thus, we have used a moving average smooth filter algorithm (Polyfit in Matlab) to obtain an outline of the test results. The IL and PI performance are calculated based on these Polyfit curves.

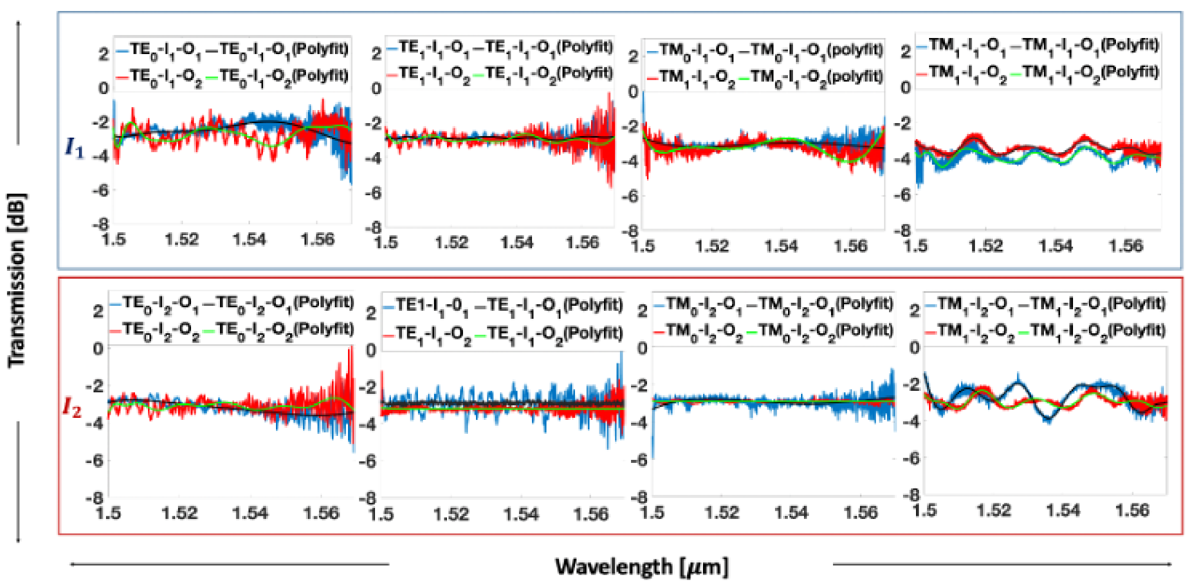

Fig. 3.17: Measured transmission (I_1-O_1) for the four modes.

The experimental results of the optical coupler show that the measured insertion losses for the four modes vary from 0.06 dB to 0.68 dB. The largest IL comes from the TM_1 mode transmission from input port I_1 to output port O_2 ($I_1 \rightarrow O_2$). This could be explained by the fact that the width of the AC input is relatively small and close to the cut off condition of TM_1 mode. The XTs for all four modes range from -31.71 dB to -15.66 dB over the 70 nm optical bandwidth range. The largest XT is between TE_0 and TE_1. That is mainly because these two modes have similar effective index properties, propagation constant and normalized frequency. For two modes of the same polarization state, their effective indices are more similar. With process variations leading to waveguide width changes, the two modes are more likely to coupler with each other. On the other end, there is a large effective index difference between TE and TM modes. Thus the XT between the same polarization status is significantly larger than between different polarization modes.

According to the measurement results shown in Fig. 3.16, the power imbalance caused by the asymmetry of the AC is also significant and should be noticed ranging from -0.47 dB to 0.91 dB. Table 3.1 summarizes the experimental results for the 3-dB coupler within 70 nm of bandwidth range from 1500 nm to 1570 nm with the worst performance indicated by bold fonts. The tunable laser can only excite the fundamental mode, to implement an on-chip MDM system interfacing with an off-chip single mode optical fiber, the (de)multiplexer is an essential part for exciting higher order modes. The experimental structure shows that the MDM circuit has a similar XT level (-15.7 dB) to the (de)multiplexer test structure (-15.4 dB). Therefore, it can be concluded that the XT performance of the MDM is mainly due to the (de)multiplexers. The modal crosstalk can be improved by further optimizing the mode (de)multiplexers. To further improve the crosstalk performance of the multiplexer and then improve the performance of the whole MDM circuit, decreasing the smallest distance between waveguides (gap) is a promising solution. The gap between waveguides is 100 nm. It can be reduced to 80 nm for stronger coupling strength. According to the experimental results shown in Fig. 3.16, we note that the dominant crosstalks come from TM0 and TM1. An improved 8-channel hybrid demultiplexer with low crosstalk was demonstrated by introducing TE-type or TM-type grating polarizer at the output ends, which can be utilized instead [45].

Table 3.1: Experimental results of the 3-dB PDM-MDM optical coupler

Mode	IL [dB] Min/Max	XT [dB] Min/Max		PI [dB] range
TE_0	0.089/0.336	TE_0-TE_1	**-19.57 / -15.66**	**-0.53 to 0.91**
		TE_0-TM_0	-30.38 / -16.54	
		TE_0-TM_1	-31.71 / -24.01	
TE_1	0.063/0.669	TE_1-TE_0	-17.05 / -15.82	-0.47 to 0.75
		TE_1-TM_0	-28.82 / -24.39	
		TE_1-TM_1	-30.11 / -26.05	
TM_0	0.108/0.402	TM_0-TE_0	-28.87 / -20.83	-0.35 to 0.85
		TM_0-TE_1	-31.15 / -24.23	
		TM_0-TM_1	-21.16 / -17.08	
TM_1	**0.198/0.684**	TM_1-TE_0	-29.07 / -21.05	-0.39 to 0.79
		TM_1-TE_1	-38.33 / -26.50	
		TM_1-TM_0	-17.05 / -16.22	

Considering the possible performance degradation caused by fabrication variations, the fabrication tolerance of the designed optical coupler is investigated. In simulation, only Gap_{AC} is changed and the other parameters remain constant. In reality, all parameters are affected by fabrication tolerance. While not exhaustive of an investigation, four optical couplers with widths ± 20 nm from the originally designed widths (W_1= 0.8 µm, W_2=

1.2 µm, W_2= 1.0 µm, first row of Table 3.2) are measured to assess the coupler's tolerance to fabrication variations. The experimental results of these structures are compared in Table 3.2 over 70 nm of optical bandwidth range from 1500 nm to 1570 nm. The worst results occur for a narrower width (last row in bold). A fabrication error leading to a narrower width by up to 20 nm results in a 0.39 dB increase in IL (from 0.68 dB to 1.07 dB), 1.4 dB increase in XT (from -15.66 dB to -13.92 dB), and 0.41 dB increase in PI (from 0.91 dB to 1.32 dB). This worst degradation is primarily due to the waveguide width being insufficiently large to support a stable transmission for TM_1, particularly when W_1 is lower than 0.8 µm.

Table 3.2: Experimental results of the optical coupler with varying waveguide widths

Widths [μm]	IL [dB] Min/Max	XT [dB] Min/Max	PI [dB] range
W_1=0.8 (design) W_2=1.2 (design) W_3=1.0 (design)	0.06/0.68	-38.33/-15.66	-0.53-0.91
W_1=0.8 (±0.0) W_2=1.0 (-0.2) W_3=0.9 (-0.1)	0.07/0.78	-36.88/-14.86	-0.67-1.12
W_1=0.9 (+0.0) W_2=1.1 (-0.1) W_3=1.0 (±0.0)	0.07/0.72	-38.05/-15.32	-0.55-0.95
W_1=0.75 (-0.05) **W_2=1.0 (-0.2)** **W_3=0.9 (-0.1)**	**0.09/1.07**	**-36.09/-13.92**	**-0.72-1.32**

3.5 Summary

In summary, we proposed and experimentally demonstrated a mode and polarization insensitive four-mode 3-dB coupler for the MDM system. The four-mode 3-dB coupler consists of an adiabatic coupler. The footprint of the designed structure is 3.88 µm $\times$ 1660 µm. The measurement shows low insertion loss (< 0.7 dB) and low modal crosstalk (< -15.7 dB) over 70 nm bandwidth ranging from 1500 nm to 1570 nm. The power imbalance of the device is less than 0.7 dB. The device is optimized for TE_0, TE_1, TM_0, TM_1 and has significant performance improvement over past published works. According to the literature review in Section 2.5.2 on PDM-MDM 3-dB coupler, the existing studies are limited and most of them are accommodating only three modes. This design is successfully compatible with four modes. Existing 3-dB couplers with four modes require special fabrication processing (shallow etch or less conventional silicon thickness: 300 nm), this design avoids the complicated process and is suitable for more conventional fabrication processing. In addition, this design has improved the experimentally validated insertion loss (below 0.7 dB) and crosstalk (below -15.66 dB) performance. By further optimizing the mode (de)multiplexers, the modal crosstalk can be improved further.

Chapter 4

Proposed PDM-MDM Optical Switches

In this chapter, we demonstrate two alternative PDM-MDM switch implementations. Using the optical coupler from Chapter 3, a multimode photonic switch matrix is developed that simultaneously exploits WDM, PDM, and MDM. First, a four modes × four CWDM switching system utilizing PDM-MDM multiplexing technologies is introduced. The working principle and estimated performance are analyzed in Section 4.1. On the basis of experimental coupler measurements, the switching loss is expected to be 10.6 dB with crosstalk limited by the MDM (de)multiplexing circuit. A PDM-MDM mode switch accommodating eight modes is then presented in Section 4.2. The proposed design under consideration is compatible with the first four TE modes and the first four TM modes. The building blocks and working principles are discussed in Section 4.1. Optimization of the switch is shown in Section 4.2, with simulation results (including insertion loss and crosstalk) compared. Over an optical bandwidth of 100 nm (1500 nm to 1600 nm), the optical mode switch exhibits at most 5.6 dB insertion loss with a maximum crosstalk of -25 dB in the simulation results.

4.1 A PDM-MDM-WDM Space Switch

4.1.1 Building Blocks and Working Principle

The 3-dB coupler introduced in the previous chapter serves as one of the MDM building blocks for a four-mode × four coarse wavelength division multiplexed optical switching system, as depicted in Fig. 4.1. Wavelength-division multiplexing (WDM) systems fall into three categories: Dense Wavelength Division Multiplexing (DWDM), the wavelength interval is less than 8 nm, with an average of 0.8 nm; Coarse Wavelength Division Multiplexing (CWDM), the wavelength interval is less than 50 nm. The typical wavelength interval is 20 nm (recommendation of the International Telecommunication Union); Wide wavelength division multiplexing (WWDM) with wavelength intervals above 50 nm. The broadband switching system with a bandwidth of 70 nm has the potential to accomplish four coarse wavelength division multiplexing. The switching system accommodates four modes with varying mode sequences and polarization states (TE_0, TE_1, TM_0, and TM_1). Four CWDM wavelengths spaced by 18 nm in the wavelength range from 1500 nm to 1570 nm. The WDM-MDM-PDM switching circuit is based on an 8 × 8 banyan topology validated by our group [127]. The 8 × 8 optical switch matrix is comprised of 12 Mach-Zehnder interferometer (MZI) switches (S1 to S12), each utilizing two 3-dB couplers as designed in Chapter 3 and a mode/polarisation-insensitive phase shifter as designed in [127].

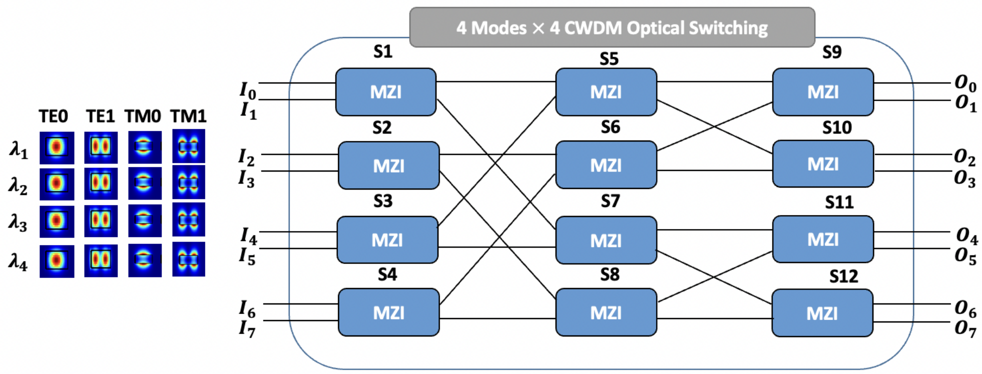

Fig. 4.1: The schematic structure of the 8 × 8 optical switch supports four modes.

The MZI-based optical switch has two states, as shown in Fig. 4.2: 1) bar state and 2) crossbar state. The MZI structure consists of two 3-dB couplers and a phase shifter. The phase shifter generates a phase difference between the two interfering signals, enabling thermally changing states. When the phase shifter is disabled, the optical switch is in the bar state. In the bar state, the two inputs are directly connected to two corresponding outputs. The optical switch is in the crossbar state when the phase shifter is enabled by applying a phase shift thermally of 180 degrees. Each input is routed to the opposite output in the cross state.

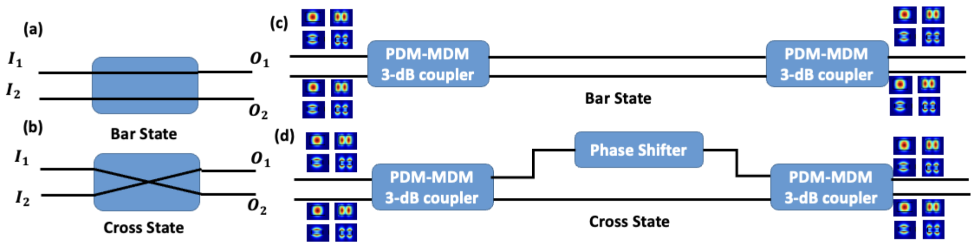

Fig. 4.2: Working principle of the optical switch. (a) optical switch in bar state; (b) optical switch in cross state; (c) MZI-based optical switch (bar state); (d) MZI-based optical switch (cross state).

The space switching function for the four modes is realized by adjusting the state of each MZI optical switch. The estimated IL varies for different optical paths and depends on the number of waveguide crossings and the state of the switch. Each routing path contains three stages (MZI elements) to realize the optical switching process. Stage 1 of the 4 Modes × 4 CWDM consists of four MZI structures labeled S1 to S4 in Fig. 4.1, each comprising two optimized 3-dB couplers as designed in Chapter 3 and a mode insensitive phase shifter based on the architecture described in [117]. Without any design change in the 3-dB coupler, the estimated footprint of the switching system is 16 × 7400 µm^2, making its implementation challenging. By shortening the PDM-MDM 3-dB coupler from 1.6 µm to 1 µm, the overall size of the switching system is 16 × 6300 µm^2, which consists of 4×3 MZI structures (3.88 × 2100 µm^2). According to the experimental results shown in Fig. 4.3, the insertion loss of 1 µm length 3-dB coupler is 1 dB and the crosstalk performance is still limited by mode multiplexers.

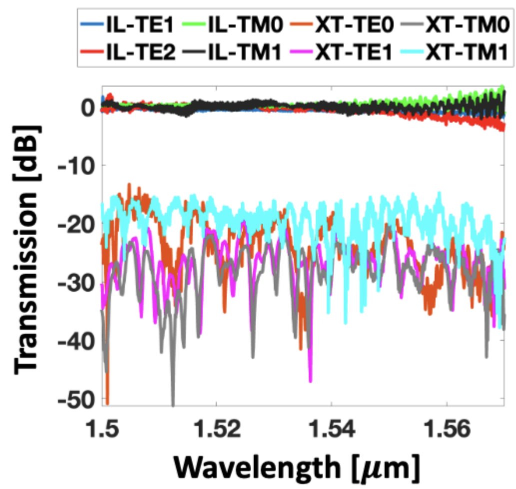

Fig. 4.3: Expermiental performance of 1 μm length 3-dB coupler.

The total insertion loss of the MZI structure over the 70 nm bandwidth (1500 nm to 1570 nm) is estimated to be 2.2 dB. This accounts for a phase shifter loss of 0.2 dB [117], but mainly comes from the two 3-dB couplers (2 × 1 dB). By taking advantage of the mode insensitive phase shifter, the switch exhibits low power consumption, since all the modes share the same phase shifter. Stage 2 also consists of four MZI structures (S5-S8). The propagation loss of multimode crossing was compared in Section 2.6. That crossing has at most 0.3 dB optical insertion loss and a crosstalk of less than -61 dB. A waveguide crossing is experimentally validated in [127]. While this crossing was for a single mode, the design needs to be modified to support the four modes of this switch. Four mode crossings were recorded in [113] with a similar loss of 0.7 dB and -35 dB of crosstalk. The MDM-WDM optical signal coming from Stage 2 propagates through the final stage with four MZIs labeled

S9 to S12.

The total switch loss is the smallest for the most direct paths (e.g., I_0-O_0, I_8-O_8), with no MZI in crossbar state and no crossing. The worst loss occurs for the optical paths which include all three MZIs in their crossbar state (e.g., I_0-O_7, I_7-O_0). As such, the largest IL of the 8×8 optical switch for those optical paths is estimated to be 9.0 dB with four waveguide crossings employed. This loss is estimated according to the loss of three MZI structures in the crossbar stage (3×2.2 dB), four waveguide crossings (4×0.7 dB), and the propagation loss from the waveguides between the MZIs. It is estimated that the switch modal crosstalk would be limited by the (de)multiplexers based on the experimental measurements of the 3-dB coupler in Chapter 3. As we can see, the multiplexer has the largest crosstalk (-15.66 dB) among all the building blocks in this switching system. The propagation loss in the internal part of the switching system is anticipated to be negligible, i.e., 0.21 dB for TM modes and 0.15 dB for TE modes (assuming the optical path length is estimated to be 1000 µm). Table 4.1 shows the approximate value of the optical loss estimated from the building blocks. The worst insertion loss is estimated to be 9.0 dB for the whole switching system.

Table 4.1: Optical loss estimation of the 8×8 switching system.

Building blocks	Unit loss (dB)	Shortest path loss (dB)	Longest path loss (dB)
Waveguide crossings	0.7	no waveguide crossings	2.8
MZI (bar)	2.0	6.0	no MZI in bar state
MZI (cross)	2.2	no MZI in cross state	6.6
Waveguide length (mm)	0.2	0.8	1.2
Total on-chip loss	—	6.8	10.6

4.2 Proposed For MDM-PDM Mode Based Switch

In this section, an eight-mode optical mode switch is designed. The structure was first proposed in [64], where a simulation of four-mode optical switch was performed. We modified the structure to polarisation-insensitive capability in order to produce an eight-mode optical switch with modes TE_0, TE_1, TE_2, TE_3, TM_0, TM_1, TM_2, and TM_3. The optical mode switch is more compact in size than the optical space switch described in Section 4.1. Typically, the space switching system consists of four input and four output ports, with each port requiring a fiber array connection. This requires more S bending regions to open the input and output ports to a 127 µm adjacent spacing for the fiber array. The mode switch requires only one input port and one output port; thus, only a single fiber connection is required. Therefore, the matrix size limitation that space switches have is alleviated. The overall size is smaller and estimated to be 5 $\times$1000 µm^2. The simulation results in this chapter show less than -25 dB mode crosstalk with less than 5.6 dB insertion loss for an eight-mode optical switch.

4.2.1 Building Blocks and Working Principle

Instead of switching information between output ports, the mode switch switches data solely between several optical modes. Due to the fact that each mode is orthogonal, the output can be incorporated onto a single port that can accommodate eight mode orders. Fig. 4.4

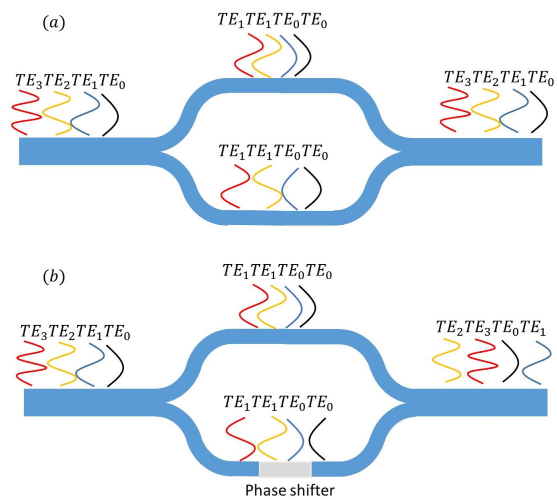

Fig. 4.4: Schematic view of optical mode switch for four TE modes. (a) Off state; (b) On state which mode conversion is illustrated by the color.

(a,b) shows the schematic view of the optical switch for four TE modes. The structure is a simple MZI, which includes two 3-dB couplers and a phase shifter region. In this design, the two 3-dB couplers work as a power splitter and a power combiner. The refractive index in the phase shifter region is thermally changeable and can be controlled by injecting current into the metal layer above (as in section 2.7). If no current is present, the phase shifter is considered disabled (or off). With an external current, the phase shifter is in enabled or in the on state and will change the mode phases by π. The Y-junction is employed because its structural symmetry allows for completely equal partition of the mode profiles. On the basis of this characteristic, the Y-junction may perform a mode-switching function that is difficult to achieve with conventional optical couplers that modify the intensity only, such as in a power splitter. As shown in Fig. 4.4, when TE_0 is excited at the input port, the

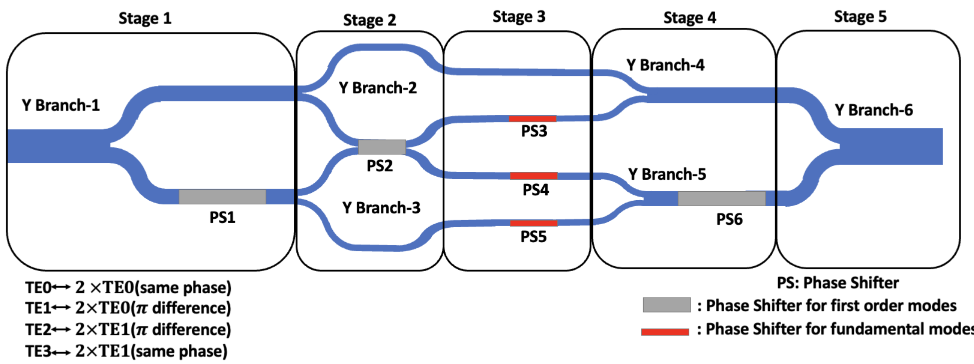

Fig. 4.5: Schematic view of the eight modes switch.

Y-junction splits it into two TE_0 modes in the two arms with the same phase. When TE_1 is injected, it splits into two TE_0 modes in the two arms with a phase π difference from each other. Similar to higher order modes, when TE_2 is the input, it splits the mode into two TE_1 modes in the two arms with a relative phase difference of π. Regarding TE_3, it splits into two TE_1 modes in each arm with the same phase. Essentially, this structure transforms the four modes of the input into two modes with no relative phase difference or a relative phase difference of π. On the basis of the reversibility of the light, the 3-dB combiner is capable of achieving the opposite process, reconstructing two modes into their corresponding modes. According to Fig. 4.4a, the output modes are arranged in the same order as they appeared at the input ports when the phase shifter is off. However, when the phase shifter is activated, the sequence of output modes changes, specifically, from TE_0, TE_1, TE_2, and TE_3 to TE_1, TE_0, TE_3, and TE_2. We further develop the schematic structure to an integrated eight mode optical switch, with the schematic displayed in Fig. 4.5.

The research of mode and polarization insensitive phase shifter was summarized in

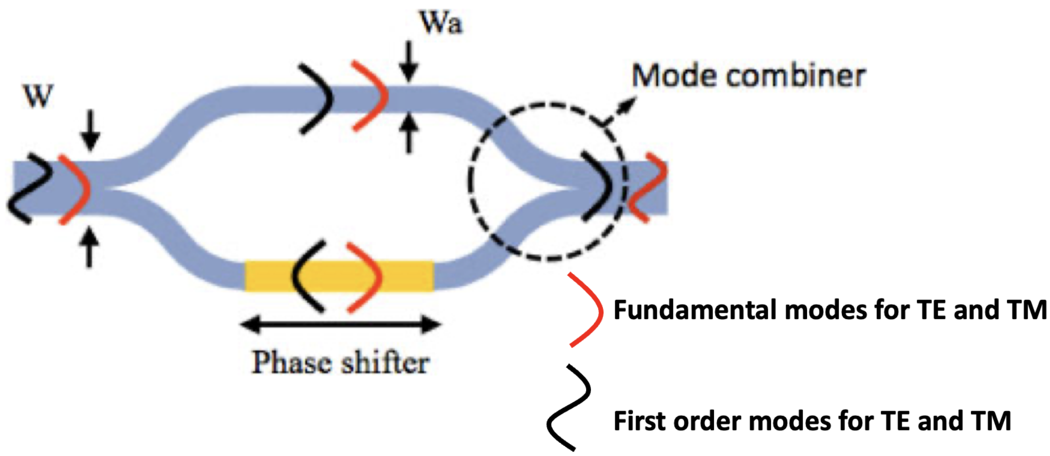

Fig. 4.6: Electrically-controlled optical mode switch configuration [122].

Section 2.7. Our group has demonstrated a mode insensitive phase shifter for three modes in [117]. However, it is polarization sensitive and is available for TE modes specifically. The only experimentally validated polarization and mode insensitive phase shifter is demonstrated in [122]. In this design, an electrically-controlled optical switch for fundamental and first order modes in both polarization status is demonstrated. The schematic of the optical switch is illustrated in Fig.4.6. This design implemented exactly the same structure as the example explained in Fig.4.5. Both fundamental and first order modes are injected into the input port of the implemented device. By injecting the electric current into the phase shifter region, the switching function is realized. Fig. 4.7 illustrates the transmission performance of the phase shifter for both fundamental and first order modes reported in [122]. The measurement was implemented with the MMI filter. The MMI mode filter was only utilized to distinguish between the fundamental and first-order

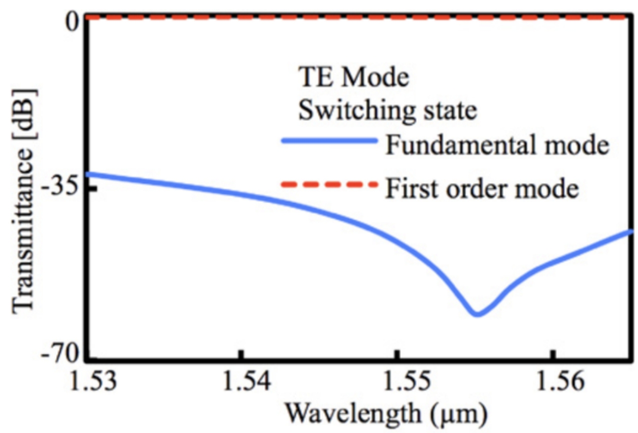

Fig. 4.7: Transmission of a phase shifter for both fundamental and first order modes [122].

modes. It was only used to aid in the investigation of crosstalk in this study. The experimental crosstalk between modes is approximately 45 dB. The IL of the phase shifter varies by no more than 0.5 dB.

By pumping currents into one arm of the optical mode switch to alter its refractive index, mode switching is achieved. Typically, a modification of at least in the order of 10^{-4} is necessary for the device to be practical at a sensible size. Fig.4.8 depicts the transmission with the phase shifter's injected current function for both TE and TM modes. When no current was injected into the device, the fundamental mode power was greater than the first-order mode with the crosstalk of 13 dB for TE and TM modes. At 42 mA current injection, both powers varied drastically, with a drop in the fundamental mode at 58 mA and a peak of in the first-order mode at 62 mA, indicating that the switching state occurred at around 60 mA (5.7 V), which shows that the π-phase shift was realized.

The device switches from one mode to another like a space crossbar switch among the

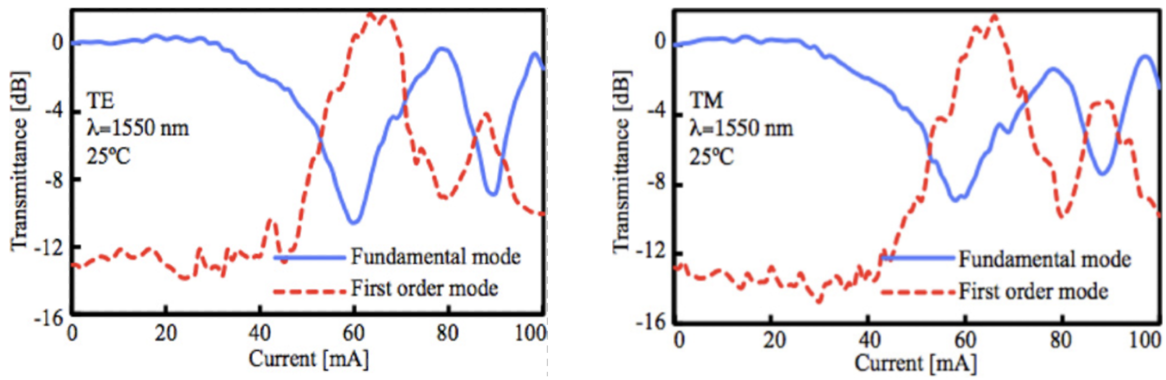

Fig. 4.8: Normalized power of electrically controlled mode switching for both TE and TM modes [122].

fundamental, first, second and third modes. Unlike the space switch discussed in Section 4.1 which has 8 × 8 configuration, the mode switching system consists of 1 input port × 1 output port. To realize the complete process of eight mode switching, it should consist of five stages. Stage 1: Y-Branch 1 with the largest width and length for accommodating higher order modes. The input port supports eight mode orders (TE_0, TE_1, TE_2, TE_3, TM_0, TM_1, TM_2, TM_3). After going through the 3-dB splitter, the divided light propagates up to second-order modes for both polarisation states in each arm, including TE_0, TE_1, TM_0, TM_1. The lower output arm of Stage 1 consists of a π phase shifter (PS1) designed for first order modes (TE_1 and TM_1). By regulating the injected current, the phase shifter is able to function for first order modes while maintaining the phase of fundamental modes. The IL in Stage 1 is estimated to be 1.2 dB, with Y-Branch 1 (0.7 dB) and PS1 contributing the majority (0.5 dB). Stage 2 consists of Y-Branch 2 and Y-Branch 3, which are intended for fundamental modes. A 3-dB splitter with narrower width divides the four modes into two fundamental modes (TE_0 and TM_0) as illustrated in Fig. 4.5. The width of the middle arm, which is shared by two 3-dB splitters, is double that of the upper and lower arms. The upper and lower arms contain only fundamental modes (TE_0 and TM_0). Nonetheless, the center middle arm working as the output port of the Y-combiner is shared by two Y-splitters and can accommodate both fundamental and first-order modes (TE_0, TE_1, TM_0, TM_1). In accordance with the principle of optical reversibility, the TE_0/TM_0 modes with phase difference from Y-branch 1 as well as Y-branch 2 are combined into TE_1/TM_1 modes in a shared output port. PS2, which only operates on first order modes (TE_1 and TM_1), is added to the center arm. The IL rose to 2.3 dB at the end of Stage 2. Y-Branch 2 and 3 (2 $\times$ 0.3 dB) and PS2 (0.5 dB) are the main causes of IL at this stage. In stage 3, all the modes are fundamental modes (TE_0 and TM_0). Three of the arms contain PS3, PS4, and PS5, which are phase shifters for fundamental modes (TE_0 and TM_0) and are denoted in red in Fig. 4.5. Because there are no additional mode orders at this stage, phase shifters are only built for fundamental modes. These phase shifters are polarization insensitive and provide more feasible sequence combinations in Stages 4 and 5 by modifying the phase condition of propagating modes. As we can conclude from Fig. 4.8, the injected current chosen for both TE and TM modes is the same (60 mA 5.7 V) [122]. The ILs in Stage 3 are primarily the result of three phase shifter (3 $\times$ 0.5 dB). In stage 4, a 3-dB combiner converts fundamental modes to both fundamental and first order modes existing simultaneously (TE_0, TE_1, TM_0, TM_1). PS6, a first-order modes phase shifter, is added in the bottom arm. Due to Y-Branch 4 and 5 and PS6, the IL accumulates to 4.9 dB. In stage 5, a wider Y-Branch 6 with a maximum 0.7 dB IL is employed for recovering eight modes on the input side (TE_0, TE_1, TE_2, TE_3, TM_0, TM_1, TM_2, and TM_3). Therefore, the IL of the entire switch is approximately 5.6 dB. Before reaching Stage 3, all incident modes are divided into four fundamental modes. The subsequent stages are for reorganizing the mode order. The optical loss estimation of the mode switch is concluded in Table 4.2.

Table 4.2: Optical loss estimation of the eight modes switching system.

	Stage1		Stage2			Stage3			Stage4			Stage5
Components	Y1	PS1	Y2	Y3	PS2	PS3	PS4	PS5	Y4	Y5	PS6	Y6
Unit loss (dB)	0.7	0.5	0.3	0.3	0.5	0.5	0.5	0.5	0.3	0.3	0.5	0.7
Total loss (dB)	5.6											

There are 24 possible switching permutations. Table 4.2 summarises all the possible switching combinations. Fig.4.9 is an illustration of a pattern. In this case, only PS3 and PS4 are enabled, mode switching is realized from TE_0/TM_0, TE_1/TM_1, TE_2/TM_2, TE_3/TM_3 to TE_3/TM_3, TE_2/TM_2, TE_0/TM_0, TE_1/TM_1.

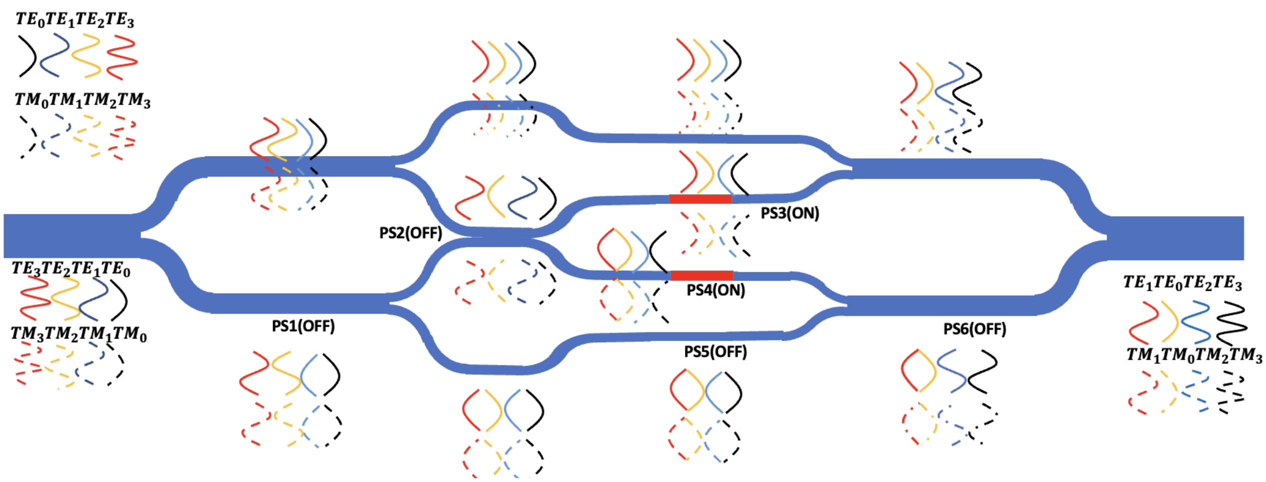

Fig. 4.9: Transmission of the phase shifter for both fundamental and first order modes.

The parameters of the Y-junction are shown in Table 4.3.

Table 4.3: Parameters of the eight mode optical switch.

	Y_1	Y_2	Y_3	Y_4	Y_5	Y_6
W_1	2.07 µm	1.0 µm	1.0 µm	1.0 µm	1.0 µm	2.07 µm
W_2	1.0 µm	0.465 µm	0.465 µm	0.465 µm	0.465 µm	1.0 µm
L_1	20 µm	10 µm	10 µm	10 µm	10 µm	20 µm
L_2	80 µm	40 µm	40 µm	40 µm	40 µm	80 µm
Gap_{in}	70 nm	70 nm	70 nm	70 nm	70 nm	70 nm
Gap_{out}	2.47 µm	1.2 µm	1.2 µm	1.2 µm	1.2 µm	2.47 µm

4.2.2 Optimization and Simulation Results

The Y-branch, which functions as a 3-dB power splitter and combiner, is schematically shown in Fig. 4.10 with a top view. The device is designed for fabrication on an SOI chip with a waveguide thickness of 220 nm. The distances between the two waveguide arms are Gap$_{in}$

Table 4.4: Switching pattern of optical mode switch for eight modes. "✓" means the phase shifter is enabled (phase shift of π),"×" means the phase shifter is disabled.

	π-phase shifter						Sequences							
	PS1	PS2	PS3	PS4	PS5	PS6	TE0	TE1	TE2	TE3	TM0	TM1	TM2	TM3
1	×	×	×	×	×	×	TE0	TE1	TE2	TE3	TM0	TM1	TM2	TM3
2	×	×	×	×	✓	✓	TE1	TE0	TE3	TE2	TM1	TM0	TM3	TM2
3	×	×	×	✓	×	✓	TE3	TE2	TE1	TE0	TM3	TM2	TM1	TM0
4	×	×	×	✓	✓	×	TE2	TE3	TE0	TE1	TM2	TM3	TM0	TM1
5	×	×	✓	×	×	×	TE0	TE1	TE3	TE2	TM0	TM1	TM3	TM2
6	×	×	✓	×	✓	✓	TE1	TE0	TE2	TE3	TM1	TM0	TM2	TM3
7	×	×	✓	✓	×	✓	TE2	TE3	TE1	TE0	TM2	TM3	TM1	TM0
8	×	×	✓	✓	✓	×	TE3	TE2	TE0	TE1	TM3	TM2	TM0	TM1
9	×	✓	×	×	×	×	TE0	TE3	TE2	TE1	TM0	TM3	TM2	TM1
10	×	✓	×	×	✓	✓	TE1	TE2	TE3	TE0	TM1	TM2	TM3	TM0
11	×	✓	×	✓	×	✓	TE3	TE0	TE1	TE2	TM3	TM0	TM1	TM2
12	×	✓	×	✓	✓	×	TE2	TE1	TE0	TE3	TM2	TM1	TM0	TM3
13	×	✓	✓	×	×	×	TE0	TE2	TE3	TE1	TM0	TM2	TM3	TM1
14	×	✓	✓	×	✓	✓	TE1	TE3	TE2	TE0	TM1	TM3	TM2	TM0
15	×	✓	✓	✓	×	✓	TE2	TE0	TE1	TE3	TM2	TM0	TM1	TM3
16	×	✓	✓	✓	✓	×	TE3	TE1	TE0	TE2	TM3	TM1	TM0	TM2
17	✓	✓	×	×	×	×	TE0	TE3	TE1	TE2	TM0	TM3	TM1	TM2
18	✓	✓	×	×	✓	✓	TE1	TE2	TE0	TE3	TM1	TM2	TM0	TM3
19	✓	✓	×	✓	×	✓	TE3	TE0	TE2	TE1	TM3	TM0	TM2	TM1
20	✓	✓	×	✓	✓	×	TE2	TE1	TE3	TE0	TM2	TM1	TM3	TM0
21	✓	✓	✓	×	×	×	TE0	TE2	TE1	TE3	TM0	TM2	TM1	TM3
22	✓	✓	✓	×	✓	✓	TE1	TE3	TE0	TE2	TM1	TM3	TM0	TM2
23	✓	✓	✓	✓	×	✓	TE2	TE0	TE3	TE1	TM2	TM0	TM3	TM1
24	✓	✓	✓	✓	✓	×	TE2	TE0	TE3	TE1	TM3	TM1	TM2	TM0

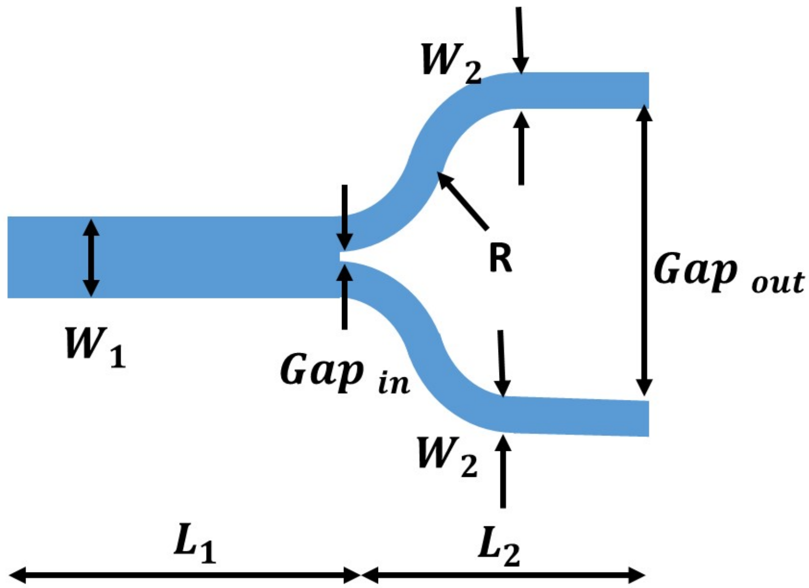

Fig. 4.10: Schematic view of Y branch.

at the input and Gap_{out} at the output. The width of the input waveguide, W_1, is greater than twice the width of the output arm, W_2 ($W_1 = 2 \times W_2 + Gap_{in}$). The Y branch is also optimized by an EME method. We optimized values for W_1, W_2, L_1, L_2, Gap_{in}, and Gap_{out} for the lowest insertion loss and crosstalk performance. Firstly, according to Fig. 4.5, the output arm (W_2) should be capable of accommodating four modes (TE_0, TE_1, TM_0, and TM_1) whereas the input arm (W_1) is built for eight modes (TE_0, TE_1, TE_2, TE_3, TM_0, TM_1, TM_2, and TM_3). According to the effective index as a function of the waveguide width shown in Fig. 3.6. We chose W_2 as 1.0 µm to ensure that the four propagating modes are in optimal condition, as described in Section 4.1. It is necessary to restrict the width of W_2 to ensure that only the desired mode is present in the output waveguide and prevent the excitation of other modes that would result in intermodal crosstalk. W_1 should be in the range of 1.8 µm to 2.2 µm. When the width is less than 1.8 µm, the cut-off condition of TM_2, the TM_2 mode is unstable because its effective index is close to that of the cladding material. However, when the width increases to 2.2 µm, most TE modes are close to a saturated status which means as the width of the waveguide increases, the change in the effective index of the mode is negligible. The smaller the value of Gap_{in}, the better the coupling between the two waveguides, as well as the IL and XT performance. Taking the fabrication limitation into consideration, Gap_{in} is set at 70 nm since the minimum feature size at ANT is 60 nm. The radius of S bends is chosen as 1000 µm to prevent further propagation loss as simulated in Fig 3.7. The Gap_{out} should be more than 2.0 µm to open the output ports and avoid modal coupling between the two arms. Gap_{out} is determined by three optimized variables R, L_2, and W_2. For a specific S-bend region, a minimum gap of 2.47 µm is required to guarantee optimal values for W_2 and L_2. The value of L_2 is optimized based on normalized transmission with respect to propagation length. For improved transmission performance, the overall length of Y-branch is set as 100 µm. The simulated mode propagation for the overall structure of the eight modes is shown in Fig. 4.11.

Fig. 4.12 shows the results of IL and XT performance of the Y-branch 1 and Y-branch 6. The IL and XT performance of other Y-branches are included in Fig. 4.13 for comparison.

They are computed using Equation 3.1 (equation for IL calculation) and 3.2 (equation for crosstalk calculation). According to the simulation results, the IL values are as high as

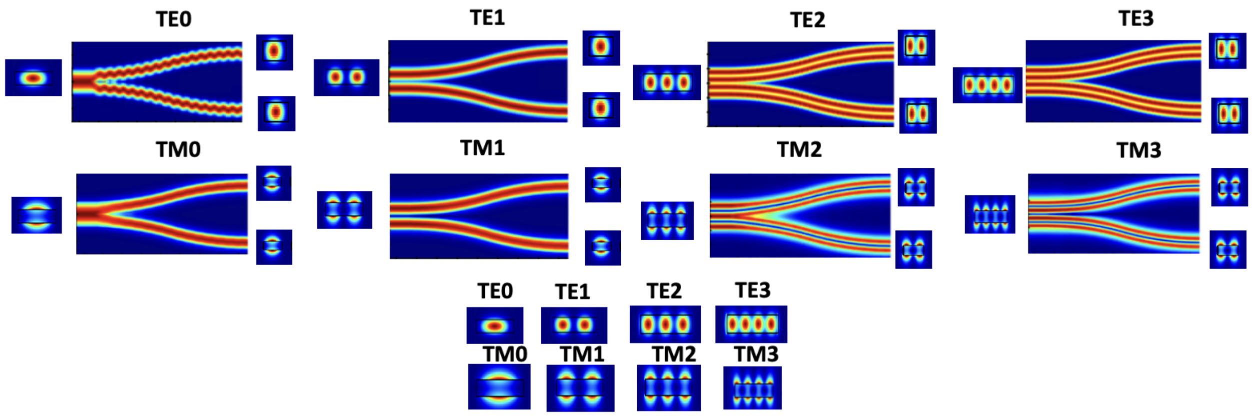

Fig. 4.11: Simulated mode propagation for Y-branch 1 in Lumerical Modes

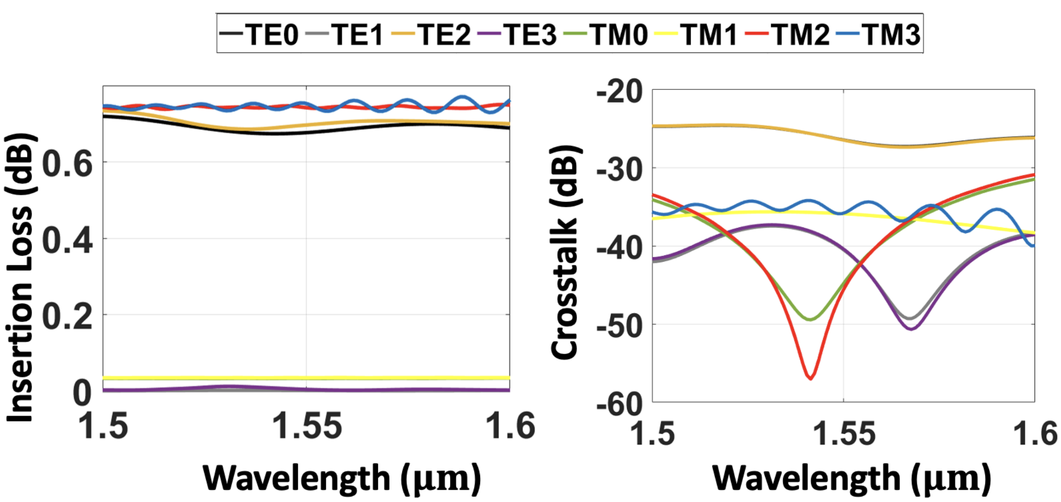

Fig. 4.12: Simulation results of the Y-Branch 1 and Y-Branch 6 which can accommodate 8 modes.

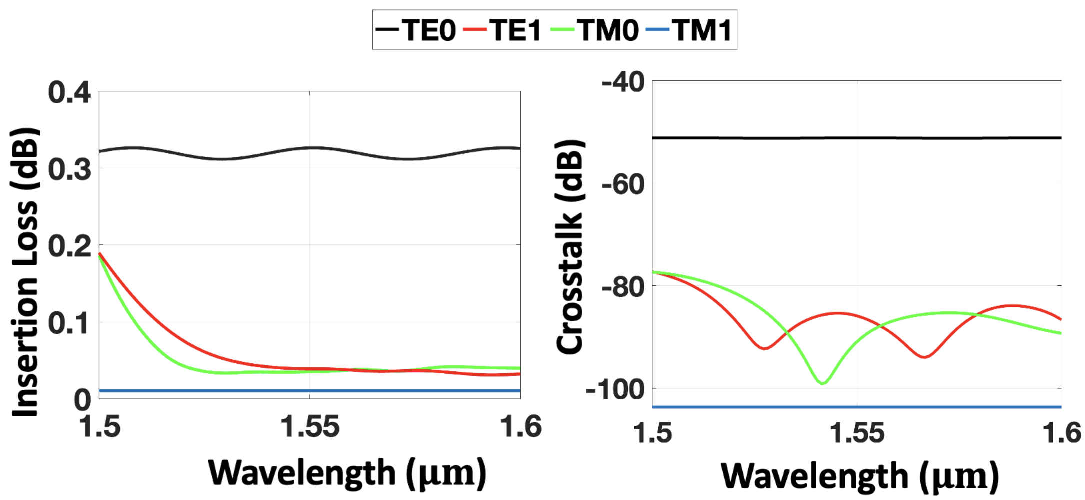

Fig. 4.13: Simulation results of the Y-Branch 2,3,4 and Y-Branch 5 which can accommodate 4 modes.

0.7 dB within the entire simulation bandwidth, from 1.5 µm to 1.6 µm. TM_3 has the largest IL because the width of the input port is small and close to its cut-off condition. According to Fig. 3.6, which describes the relationship between the gap and coupling strength, the waveguide gap has a significant impact on the IL, and if the gap between the waveguides can be decreased while maintaining fabricating precision, the IL performance will be considerably reduced. It is also not possible to simply increase the value of W_1 to avoid higher modes excitation, which contributes to worse XT performance. The XTs for all eight modes are within the range of -58 dB to -25 dB over the 100 nm optical bandwidth ranging from 1500 nm to 1600 nm. As shown in Fig. 4.12, the largest XT comes from TE_0 and TE_2 modes. This can be explained by the effective indices of all the four TE modes being close to each other at the width of 2.47 µm (Gap_{out}) according to Fig. 3.5 (describing the effective index of different modes with respect to waveguide width). It is easier for modes with comparable effective indices to realize reciprocal conversions and excitation, resulting in a greater crosstalk.

The overall IL is estimated as 5.6 dB. The main IL comes from Y-Branch and phase shifter. Among all the devices in the switching system, TM3 has the largest transmission loss because the waveguide width makes it harder for this mode to stabilize. The crosstalk of the whole system can be estimated as -15.66 dB, which is mainly affected by the crosstalk performance of the multiplexers discussed in Chapter 3 (Fig. 3.15).

4.3 Comparison and Conclusion

In Chapter 4, we proposed two optical switches with promising performance. A four-mode optical space switch that works for TE_0, TE_1, TM_0, and TM_1 is discussed in Section 4.1. It is based on the experimentally validated 3-dB coupler from Chapter 3. The estimated insertion loss is less than 9.0 dB with at most -16 dB crosstalk. The overall size of the device is relatively large (3.88×6200 µm^2). An eight-mode optical mode switch is discussed in Section 4.2. It has additional data channels and more extensive transmission throughout. Furthermore, the overall size of the device itself is smaller, estimated to (5×1000 µm^2). To realize the MDM system, a (de)multiplexer structure is required at both the beginning and end of the system, which would cause 50 $\times$270 µm^2) additional size. In conclusion, the IL is estimated as 5.6 dB for the entire system, and the mutliplexer's performance still restricts the crosstalk. These two proposed switches have their functions and could find their applications in the MDM-PDM systems.

Chapter 5

Future work and conclusion

The crosstalk performance of MDM system is limited essentially by the mode multiplexers which is required to convert the fundamental modes to higher modes in the MDM interconnects. By further optimizing the structure parameters of the multiplexer, we can improve the crosstalk performance of the whole system. A novel multiplexer design using inverse design provides enhanced performance with a compactable size [128]. In addition, both of the proposed optical switches in Section 4 suffer from the same drawback, namely their large size, which limits their more comprehensive application. In recent years, with the continuous increase in the number of modes carried by the devices, the device size has to be significantly increased to ensure low propagation loss and crosstalk. However, this solution conflicts with the high density and high performing requirements of photonic devices. Inverse design is a method that has been developed in recent years to achieve high density and high performance integrated silicon-based devices through the use of multiple algorithms. For the field of on-chip optical interconnects, inverse design can effectively reduce the size of integrated silicon-based devices while maintaining a high level of performance [118]. The concept of inverse design has greatly expanded the potential for designing new device structures, which can theoretically have a variety of sizes and shapes, and the diversity of structures has increased the capacity to generate devices with new functions. The inverse design of integrated photonic devices relies on intelligent algorithms that set the device parameters expected to be achieved and solve the device's structural composition in the reverse direction. The process requires training a model with specific judgment and generation capabilities, followed by inputting the expected performance parameters into the trained model, which then determines the corresponding device structure.

In recent years, several MDM components using inverse design have been reported, such as mode (de)multiplexing [112], multimode bends [30, 129], multimode crossing [112], multimode splitter [59, 130], mode exchanger [131], and multimode optical switch [132]. It is promising to improve the system size and transmission performance by utilizing inverse design on all the MDM-PDM building blocks. A three-channel (de)multiplexer with 50 nm channel spacing and 6.2 $\times$5.4 µm^2) footprint is designed with an energy constrained inverse design method in [128]. In addition, a mode insensitive phase shifter with a footprint of 4 $\times$4 µm^2) is experimentally demonstrated in [66]. Besides, by further optimizing the propagation length, the overall size of 3-dB coupler can be reduced to 3.88 $\times$1000 µm^2 with good performance of IL and XT. Thus, the footprint MDM-PDM system is promising to 16 $\times$6200 µm^2. Finally, the size of 3-dB coupler can be further shortened using subwavelength gratings(SWG) [133].

MDM-PDM optical interconnection has found its application in communication systems, particularly for short-distance optical links using few-mode fibers [134] and multi-core fibers [135]. Furthermore, the MDM technology is widely considered in quantum photonics [136], and nonlinear photonics [137]. These emerging applications make MDM-PDM silicon photonics increasingly desirable and promising. By combining inverse design technology, an enhanced MDM-PDM optical interconnect will have more applications in the future across a variety of fields.

Bibliography

[1] C. Williamson, "Internet traffic measurement," *IEEE Internet Computing*, vol. 5, no. 6, pp. 70–74, 2001.

[2] Cisco, "Cisco global cloud index, forecast and methodology, 2016–2021 white paper," 2018.

[3] F. Tariq, M. R. Khandaker, K.-K. Wong, M. A. Imran, M. Bennis, and M. Debbah, "A speculative study on 6g," *IEEE Wireless Communications*, vol. 27, no. 4, pp. 118–125, 2020.

[4] K. Ha, P. Pillai, G. Lewis, S. Simanta, S. Clinch, N. Davies, and M. Satyanarayanan, "The impact of mobile multimedia applications on data center consolidation," in *2013 IEEE International Conference On Cloud Engineering (IC2E)*, pp. 166–176, IEEE, 2013.

[5] A. N. Soloviev, P. V. Vasiliev, and L. A. Podkolzina, "Development and application of distributed computing system in inverse problems of fracture mechanics," *Advanced Engineering Research*, vol. 17, no. 4, pp. 89–96, 2018.

[6] J. W. Goodman, F. J. Leonberger, S.-Y. Kung, and R. A. Athale, "Optical interconnections for vlsi systems," *Proceedings of the IEEE*, vol. 72, no. 7, pp. 850–866,

1984.

[7] J. Bashir, E. Peter, and S. R. Sarangi, "A survey of on-chip optical interconnects," *ACM Computing Surveys (CSUR)*, vol. 51, no. 6, pp. 1–34, 2019.

[8] A. Biberman and K. Bergman, "Optical interconnection networks for high-performance computing systems," *Reports on Progress in Physics*, vol. 75, no. 4, p. 046402, 2012.

[9] J. Wang, *CMOS-Compatible Key Engineering Devices for High-Speed Silicon-Based Optical Interconnections.* Springer, 2018.

[10] C. Li, H. Wu, Y. Tan, S. Wang, and D. Dai, "Silicon-based on-chip hybrid (de) multiplexers," *Science China Information Sciences*, vol. 61, no. 8, pp. 1–14, 2018.

[11] K. C. Kao and G. A. Hockham, "Dielectric-fibre surface waveguides for optical frequencies," in *Proceedings of the Institution of Electrical Engineers*, vol. 113, pp. 1151–1158, IET, 1966.

[12] P. J. Winzer, D. T. Neilson, and A. R. Chraplyvy, "Fiber-optic transmission and networking: the previous 20 and the next 20 years," *Optics Express*, vol. 26, no. 18, pp. 24190–24239, 2018.

[13] R. A. Soref, "Silicon-based optoelectronics," *Proceedings of the IEEE*, vol. 81, no. 12, pp. 1687–1706, 1993.

[14] F. Kish, V. Lal, P. Evans, S. W. Corzine, M. Ziari, T. Butrie, M. Reffle, H.-S. Tsai, A. Dentai, J. Pleumeekers, *et al.*, “System-on-chip photonic integrated circuits,” *IEEE Journal of Selected Topics in Quantum Electronics*, vol. 24, no. 1, pp. 1–20, 2017.

[15] D. Allwood, R. Carline, N. Mason, C. Pickering, B. Tanner, and P. Walker, “Characterization of oxide layers on GaAs substrates,” *Thin Solid Films*, vol. 364, no. 1-2, pp. 33–39, 2000.

[16] J. Casady and R. W. Johnson, “Status of silicon carbide (SiC) as a wide-bandgap semiconductor for high-temperature applications: A review,” *Solid-State Electronics*, vol. 39, no. 10, pp. 1409–1422, 1996.

[17] T. J. Flack, B. N. Pushpakaran, and S. B. Bayne, “GaN technology for power electronic applications: a review,” *Journal of Electronic Materials*, vol. 45, no. 6, pp. 2673–2682, 2016.

[18] G. K. Celler and S. Cristoloveanu, “Frontiers of silicon-on-insulator,” *Journal of Applied Physics*, vol. 93, no. 9, pp. 4955–4978, 2003.

[19] G. Moore, “Moore’s law,” *Electronics Magazine*, vol. 38, no. 8, p. 114, 1965.

[20] W. Shi, W. Lv, T. Sun, and B. Zhang, “Optoelectronic platform and technology,” *Frontiers of Information Technology & Electronic Engineering*, vol. 20, no. 4, pp. 439–457, 2019.

[21] Y. He, Y. Zhang, H. Wang, L. Sun, and Y. Su, "Design and experimental demonstration of a silicon multi-dimensional (de) multiplexer for wavelength-, mode-and polarization-division (de) multiplexing," *Optics Letters*, vol. 45, no. 10, pp. 2846–2849, 2020.

[22] C. Pollock and M. Lipson, *Integrated photonics*, vol. 20. Springer, 2003.

[23] S. Berdagué and P. Facq, "Mode division multiplexing in optical fibers," *Applied Optics*, vol. 21, no. 11, pp. 1950–1955, 1982.

[24] D. Dai, J. Wang, and S. He, "Silicon multimode photonic integrated devices for on-chip mode-division-multiplexed optical interconnects (invited review)," *Progress In Electromagnetics Research*, vol. 143, pp. 773–819, 2013.

[25] T. Uematsu, Y. Ishizaka, Y. Kawaguchi, K. Saitoh, and M. Koshiba, "Design of a compact two-mode multi/demultiplexer consisting of multimode interference waveguides and a wavelength-insensitive phase shifter for mode-division multiplexing transmission," *Journal of Lightwave Technology*, vol. 30, no. 15, pp. 2421–2426, 2012.

[26] J. Xing, Z. Li, X. Xiao, J. Yu, and Y. Yu, "Two-mode multiplexer and demultiplexer based on adiabatic couplers," *Optics Letters*, vol. 38, no. 17, pp. 3468–3470, 2013.

[27] J. Wang, Y. Xuan, M. Qi, H. Huang, Y. Li, M. Li, X. Chen, Z. Sheng, A. Wu, and W. Li, "Broadband and fabrication-tolerant on-chip scalable mode-division multiplexing

based on mode-evolution counter-tapered couplers," *Optics Letters*, vol. 40, no. 9, pp. 1956–1959, 2015.

[28] H. Li, P. Wolf, X. Jia, J. A. Lott, and D. Bimberg, "Thermal analysis of high-bandwidth and energy-efficient 980 nm vcsels with optimized quantum well gain peak-to-cavity resonance wavelength offset," *Applied Physics Letters*, vol. 111, no. 24, p. 243508, 2017.

[29] D. Guo and T. Chu, "Silicon mode (de) multiplexers with parameters optimized using shortcuts to adiabaticity," *Optics Express*, vol. 25, no. 8, pp. 9160–9170, 2017.

[30] H. Xu, D. Dai, and Y. Shi, "Silicon integrated nanophotonic devices for on-chip multi-mode interconnects," *Applied Sciences*, vol. 10, no. 18, p. 6365, 2020.

[31] Y. Ding, J. Xu, F. Da Ros, B. Huang, H. Ou, and C. Peucheret, "On-chip two-mode division multiplexing using tapered directional coupler-based mode multiplexer and demultiplexer," *Optics Express*, vol. 21, no. 8, pp. 10376–10382, 2013.

[32] W. Jiang, F. Cheng, J. Xu, and H. Wan, "Compact and low-crosstalk mode (de) multiplexer using a triple plasmonic-dielectric waveguide-based directional coupler," *Journal of the Optical Society of America B*, vol. 35, no. 10, pp. 2532–2540, 2018.

[33] J. P. Nath, N. Dhingra, G. J. Saxena, and E. K. Sharma, "Compact mode division (de) multiplexer based on collaterally coupled SOI waveguides," *IEEE Photonics Technology Letters*, vol. 32, no. 10, pp. 595–598, 2020.

[34] W. Chen, P. Wang, T. Yang, G. Wang, T. Dai, Y. Zhang, L. Zhou, X. Jiang, and J. Yang, "Silicon three-mode (de) multiplexer based on cascaded asymmetric y junctions," *Optics Letters*, vol. 41, no. 12, pp. 2851–2854, 2016.

[35] C. Li and D. Dai, "Low-loss and low-crosstalk multi-channel mode (de) multiplexer with ultrathin silicon waveguides," *Optics Letters*, vol. 42, no. 12, pp. 2370–2373, 2017.

[36] D. Dai, C. Li, S. Wang, H. Wu, Y. Shi, Z. Wu, S. Gao, T. Dai, H. Yu, and H.-K. Tsang, "10-channel mode (de) multiplexer with dual polarizations," *Laser & Photonics Reviews*, vol. 12, no. 1, p. 1700109, 2018.

[37] C. Li, D. Liu, and D. Dai, "Multimode silicon photonics," *Nanophotonics*, vol. 8, no. 2, pp. 227–247, 2019.

[38] W. Jiang, "Ultra-compact and fabrication-tolerant mode multiplexer and demultiplexer based on angled silicon waveguides," *Optics Communications*, vol. 425, pp. 141–145, 2018.

[39] M. Greenberg and M. Orenstein, "Multimode add-drop multiplexing by adiabatic linearly tapered coupling," *Optics Express*, vol. 13, no. 23, pp. 9381–9387, 2005.

[40] J. B. Driscoll, C. P. Chen, R. R. Grote, B. Souhan, J. I. Dadap, A. Stein, M. Lu, K. Bergman, and R. M. Osgood, "A 60 gb/s mdm-wdm si photonic link with¡ 0.7 db power penalty per channel," *Optics Express*, vol. 22, no. 15, pp. 18543–18555, 2014.

[41] J. Wang, M. Qi, Y. Xuan, H. Huang, Y. Li, M. Li, X. Chen, Q. Jia, Z. Sheng, and A. Wu, "Ultrabroadband silicon-on-insulator polarization beam splitter based on cascaded mode-sorting asymmetric y-junctions," *IEEE Photonics Journal*, vol. 6, no. 6, pp. 1–8, 2014.

[42] W. Chen, P. Wang, and J. Yang, "Optical mode interleaver based on the asymmetric multimode y junction," *IEEE Photonics Technology Letters*, vol. 26, no. 20, pp. 2043–2046, 2014.

[43] B.-T. Lee and S.-Y. Shin, "Mode-order converter in a multimode waveguide," *Optics Letters*, vol. 28, no. 18, pp. 1660–1662, 2003.

[44] A. L. Low, Y. S. Yong, A. H. You, S. F. Chien, and C. F. Teo, "A five-order mode converter for multimode waveguide," *IEEE Photonics Technology Letters*, vol. 16, no. 7, pp. 1673–1675, 2004.

[45] J. Wang, P. Chen, S. Chen, Y. Shi, and D. Dai, "Improved 8-channel silicon mode demultiplexer with grating polarizers," *Optics Express*, vol. 22, no. 11, pp. 12799–12807, 2014.

[46] H. Qiu, H. Yu, T. Hu, G. Jiang, H. Shao, P. Yu, J. Yang, and X. Jiang, "Silicon mode multi/demultiplexer based on multimode grating-assisted couplers," *Optics Express*, vol. 21, no. 15, pp. 17904–17911, 2013.

[47] J. M. Castro, D. F. Geraghty, S. Honkanen, C. M. Greiner, D. Iazikov, and T. W. Mossberg, "Demonstration of mode conversion using anti-symmetric waveguide bragg gratings," *Optics Express*, vol. 13, no. 11, pp. 4180–4184, 2005.

[48] D. Ohana and U. Levy, "Mode conversion based on dielectric metamaterial in silicon," *Optics Express*, vol. 22, no. 22, pp. 27617–27631, 2014.

[49] T.-Y. Lin, F.-C. Hsiao, Y.-W. Jhang, C. Hu, and S.-Y. Tseng, "Mode conversion using optical analogy of shortcut to adiabatic passage in engineered multimode waveguides," *Optics Express*, vol. 20, no. 21, pp. 24085–24092, 2012.

[50] M. Teng, K. Kojima, T. Koike-Akino, B. Wang, C. Lin, and K. Parsons, "Broadband soi mode order converter based on topology optimization," in *2018 Optical Fiber Communications Conference and Exposition (OFC)*, pp. 1–3, IEEE, 2018.

[51] C. Burtscher, D. Seyringer, and M. Lucki, "Study of the optical properties of 1$\times$ 16 splitter based on y-branch and mmi approaches," in *2016 18th International Conference on Transparent Optical Networks (ICTON)*, pp. 1–4, IEEE, 2016.

[52] M.-S. Rouifed, C. G. Littlejohns, G. X. Tina, H. Qiu, J. S. Penades, M. Nedeljkovic, Z. Zhang, C. Liu, D. J. Thomson, and G. Z. Mashanovich, "Ultra-compact mmi-based beam splitter demultiplexer for the nir/mir wavelengths of 1.55 μm and 2 μm," *Optics Express*, vol. 25, no. 10, pp. 10893–10900, 2017.

[53] N. Najeeb, Y. Zhang, C. J. Mellor, and T. M. Benson, “Design, fabrication and demonstration of a 1 × 20 multimode interference splitter for parallel biosensing applications,” in *Journal of Physics: Conference Series*, vol. 679, p. 012027, IOP Publishing, 2016.

[54] Y. Zhang, S. Yang, A. E.-J. Lim, G.-Q. Lo, C. Galland, T. Baehr-Jones, and M. Hochberg, “A compact and low loss Y-junction for submicron silicon waveguide,” *Optics Express*, vol. 21, no. 1, pp. 1310–1316, 2013.

[55] Y. Luo, Y. Yu, M. Ye, C. Sun, and X. Zhang, “Integrated dual-mode 3 dB power coupler based on tapered directional coupler,” *Scientific Reports*, vol. 6, no. 1, pp. 1–7, 2016.

[56] J. R. Ong, T. Y. Ang, E. Sahin, B. Pawlina, G. Chen, D. Tan, S. T. Lim, and C. E. Png, “Broadband silicon polarization beam splitter with a high extinction ratio using a triple-bent-waveguide directional coupler,” *Optics Letters*, vol. 42, no. 21, pp. 4450–4453, 2017.

[57] Y. Wang, L. Xu, H. Yun, M. Ma, A. Kumar, E. El-Fiky, R. Li, N. Abadíacalvo, L. Chrostowski, N. A. Jaeger, *et al.*, “Polarization-independent mode-evolution-based coupler for the silicon-on-insulator platform,” *IEEE Photonics Journal*, vol. 10, no. 3, pp. 1–10, 2018.

[58] H. Shiran, O. Liboiron-Ladouceur, *et al.*, "Dual-mode broadband compact 2× 2 optical power splitter using sub-wavelength metamaterial structures," *Optics Express*, vol. 29, no. 15, pp. 23864–23876, 2021.

[59] H. Xie, Y. Liu, Y. Wang, Y. Wang, Y. Yao, Q. Song, J. Du, Z. He, and K. Xu, "An ultra-compact 3-db power splitter for three modes based on pixelated meta-structure," *IEEE Photonics Technology Letters*, vol. 32, no. 6, pp. 341–344, 2020.

[60] L. Han, B. P.-P. Kuo, N. Alic, and S. Radic, "Ultra-broadband multimode 3-dB optical power splitter using an adiabatic coupler and a Y-branch," *Optics Express*, vol. 26, no. 11, pp. 14800–14809, 2018.

[61] Y. Liu, Z. Wang, Y. Liu, X. Wang, X. Guo, D. Li, Y. Yao, Q. Song, J. Du, Z. He, *et al.*, "Ultra-compact mode-division multiplexed photonic integrated circuit for dual polarizations," *Journal of Lightwave Technology*, vol. 39, no. 18, pp. 5925–5932, 2021.

[62] K. Chen, J. Yan, S. He, and L. Liu, "Broadband optical switch for multiple spatial modes based on a silicon densely packed waveguide array," *Optics Letters*, vol. 44, no. 4, pp. 907–910, 2019.

[63] H. Yang, Y. Kuan, T. Xiang, Y. Zhu, X. Cai, and L. Liu, "Broadband polarization-insensitive optical switch on silicon-on-insulator platform," *Optics Express*, vol. 26, no. 11, pp. 14340–14345, 2018.

[64] R. Takakura, M. Jizodo, A. Fujino, T. Tanaka, and K. Hamamoto, “Proposal of optical mode switch,” *Japanese Journal of Applied Physics*, vol. 53, no. 8S2, p. 08MB10, 2014.

[65] R. B. Priti, H. P. Bazargani, Y. Xiong, and O. Liboiron-Ladouceur, “Mode selecting switch using multimode interference for on-chip optical interconnects,” *Optics Letters*, vol. 42, no. 20, pp. 4131–4134, 2017.

[66] G. Zhang, D.-X. Xu, Y. Grinberg, and O. Liboiron-Ladouceur, “Efficient mode exchanger-based silicon photonic switch enabled by inverse design,” *Optics Express*, vol. 30, no. 12, pp. 20543–20553, 2022.

[67] C. Sun, W. Wu, Y. Yu, G. Chen, X. Zhang, X. Chen, D. J. Thomson, and G. T. Reed, “De-multiplexing free on-chip low-loss multimode switch enabling reconfigurable inter-mode and inter-path routing,” *Nanophotonics*, vol. 7, no. 9, pp. 1571–1580, 2018.

[68] W. Shen, J. Du, K. Xu, and Z. He, “On-chip selective dual-mode switch for 2-μm wavelength high-speed optical interconnection,” *IEEE Photonics Technology Letters*, vol. 33, no. 10, pp. 483–486, 2021.

[69] K. T. Ahmmed, H. P. Chan, and B. Li, “Multi-function mode processing device for mode division multiplexing optical networks,” *IEEE Photonics Technology Letters*, vol. 33, no. 2, pp. 101–104, 2020.

[70] P. Guo, W. Hou, L. Guo, Z. Ning, M. S. Obaidat, and W. Liu, "WDM-MDM silicon-based optical switching for data center networks," in *ICC 2019-2019 IEEE International Conference on Communications (ICC)*, pp. 1–6, IEEE, 2019.

[71] H. Jia, S. Yang, T. Zhou, S. Shao, X. Fu, L. Zhang, and L. Yang, "WDM-compatible multimode optical switching system-on-chip," *Nanophotonics*, vol. 8, no. 5, pp. 889–898, 2019.

[72] B. Bhandari, C.-S. Im, O. R. Sapkota, and S.-S. Lee, "Highly efficient broadband silicon nitride polarization beam splitter incorporating serially cascaded asymmetric directional couplers," *Optics Letters*, vol. 45, no. 21, pp. 5974–5977, 2020.

[73] B. Shen, P. Wang, R. Polson, and R. Menon, "An integrated-nanophotonics polarization beamsplitter with 2.4× 2.4 μm 2 footprint," *Nature Photonics*, vol. 9, no. 6, pp. 378–382, 2015.

[74] G. Larisch, P. Moser, J. A. Lott, and D. Bimberg, "Impact of photon lifetime on the temperature stability of 50 Gb/s 980 nm VCSELs," *IEEE Photonics Technology Letters*, vol. 28, no. 21, pp. 2327–2330, 2016.

[75] L. Liu, Q. Deng, and Z. Zhou, "Manipulation of beat length and wavelength dependence of a polarization beam splitter using a subwavelength grating," *Optics Letters*, vol. 41, no. 21, pp. 5126–5129, 2016.

[76] Y. Xu and J. Xiao, "Compact and high extinction ratio polarization beam splitter using subwavelength grating couplers," *Optics Letters*, vol. 41, no. 4, pp. 773–776, 2016.

[77] C. Li and D. Dai, "Compact polarization beam splitter for silicon photonic integrated circuits with a 340-nm-thick silicon core layer," *Optics Letters*, vol. 42, no. 21, pp. 4243–4246, 2017.

[78] L. Xu, Y. Wang, E. El-Fiky, D. Mao, A. Kumar, Z. Xing, M. G. Saber, M. Jacques, and D. V. Plant, "Compact broadband polarization beam splitter based on multimode interference coupler with internal photonic crystal for the soi platform," *Journal of Lightwave Technology*, vol. 37, no. 4, pp. 1231–1240, 2019.

[79] H. Xu, D. Dai, and Y. Shi, "Ultra-broadband and ultra-compact on-chip silicon polarization beam splitter by using hetero-anisotropic metamaterials," *Laser & Photonics Reviews*, vol. 13, no. 4, p. 1800349, 2019.

[80] F. Zhang, J. Zheng, Y. Song, W. Liu, P. Xu, and A. Majumdar, "Ultra-broadband and compact polarizing beam splitter in silicon photonics," *OSA Continuum*, vol. 3, no. 3, pp. 560–567, 2020.

[81] C. Li, M. Zhang, J. E. Bowers, and D. Dai, "Ultra-broadband polarization beam splitter with silicon subwavelength-grating waveguides," *Optics Letters*, vol. 45, no. 8, pp. 2259–2262, 2020.

[82] J. M. Luque-González, A. Herrero-Bermello, A. Ortega-Moñux, M. Sánchez-Rodríguez, A. V. Velasco, J. H. Schmid, P. Cheben, Í. Molina-Fernández, and R. Halir, "Polarization splitting directional coupler using tilted subwavelength gratings," *Optics Letters*, vol. 45, no. 13, pp. 3398–3401, 2020.

[83] A. Herrero-Bermello, A. Dias-Ponte, J. M. Luque-González, A. Ortega-Moñux, A. V. Velasco, P. Cheben, and R. Halir, "Experimental demonstration of metamaterial anisotropy engineering for broadband on-chip polarization beam splitting," *Optics Express*, vol. 28, no. 11, pp. 16385–16393, 2020.

[84] S. Z. Ahmed, I. Ahmed, M. B. Mia, N. Jaidye, and S. Kim, "Ultra-high extinction ratio polarization beam splitter with extreme skin-depth waveguide," *Optics Letters*, vol. 46, no. 9, pp. 2164–2167, 2021.

[85] H. Wu, Y. Tan, and D. Dai, "Ultra-broadband high-performance polarizing beam splitter on silicon," *Optics Express*, vol. 25, no. 6, pp. 6069–6075, 2017.

[86] W. Deng, L. Chen, S. Yuan, Y. Wang, R. Wang, Z. Wang, Y. Yu, X. Wu, and X. Zhang, "Silicon-based integrated terahertz polarization beam splitters," *Journal of Lightwave Technology*, vol. 40, no. 1, pp. 170–178, 2022.

[87] S. Chen, Y. Shi, S. He, and D. Dai, "Low-loss and broadband 2× 2 silicon thermo-optic mach–zehnder switch with bent directional couplers," *Optics Letters*, vol. 41, no. 4, pp. 836–839, 2016.

[88] Y. Yao, Z. Cheng, J. Dong, and X. Zhang, “Performance of integrated optical switches based on 2d materials and beyond,” *Frontiers of Optoelectronics*, vol. 13, no. 2, pp. 129–138, 2020.

[89] F. Horst, W. M. Green, S. Assefa, S. M. Shank, Y. A. Vlasov, and B. J. Offrein, “Cascaded mach-zehnder wavelength filters in silicon photonics for low loss and flat pass-band wdm (de-) multiplexing,” *Optics Express*, vol. 21, no. 10, pp. 11652–11658, 2013.

[90] S. Han, W. Liu, and Y. Shi, “Ultra-broadband dual-polarization power splitter based on silicon subwavelength gratings,” *IEEE Photonics Technology Letters*, vol. 33, no. 15, pp. 765–768, 2021.

[91] X. Chen, W. Liu, Y. Zhang, and Y. Shi, “Polarization-insensitive broadband 2× 2 3-db power splitter based on silicon-bent directional couplers,” *Optics Letters*, vol. 42, no. 19, pp. 3738–3740, 2017.

[92] D. Dai, Z. Wang, J. Peters, and J. E. Bowers, “Compact polarization beam splitter using an asymmetrical mach–zehnder interferometer based on silicon-on-insulator waveguides,” *IEEE Photonics Technology Letters*, vol. 24, no. 8, pp. 673–675, 2012.

[93] Z. Xiao, X. Luo, P. H. Lim, P. Prabhathan, S. T. Silalahi, T.-Y. Liow, J. Zhang, and F. Luan, “Ultra-compact low loss polarization insensitive silicon waveguide splitter,” *Optics Express*, vol. 21, no. 14, pp. 16331–16336, 2013.

[94] H. Li, W. Chen, P. Wang, S. Dai, Y. Liu, Q. Fu, J. Li, Y. Li, T. Dai, H. Yu, *et al.*, "Compact and low-loss 1× 3 polarization-insensitive optical power splitter using cascaded tapered silicon waveguides," *Optics Letters*, vol. 45, no. 19, pp. 5596–5599, 2020.

[95] X. Deng, L. Yan, H. Jiang, X. Feng, W. Pan, and B. Luo, "Polarization-insensitive and tunable silicon mach-zehnder wavelength filters with flat transmission passband," *IEEE Photonics Journal*, vol. 10, no. 3, pp. 1–7, 2018.

[96] H. Okayama, Y. Onawa, D. Shimura, H. Yaegashi, and H. Sasaki, "Polarization rotation bragg grating using si wire waveguide with non-vertical sidewall," *Optics Express*, vol. 22, no. 25, pp. 31371–31378, 2014.

[97] D. Liu and D. Dai, "Silicon-based polarization-insensitive optical filter with dual-gratings," *Optics Express*, vol. 27, no. 15, pp. 20704–20710, 2019.

[98] H. Xu, L. Liu, and Y. Shi, "Polarization-insensitive four-channel coarse wavelength-division (de) multiplexer based on mach–zehnder interferometers with bent directional couplers and polarization rotators," *Optics Letters*, vol. 43, no. 7, pp. 1483–1486, 2018.

[99] S. Agashe, K.-T. Shiu, and S. Forrest, "Compact polarization-insensitive ingaasp-inp 2× 2 optical switch," *IEEE Photonics Technology Letters*, vol. 17, no. 1, pp. 52–54, 2004.

[100] S.-H. Kim, K. Tanizawa, Y. Shoji, G. Cong, K. Suzuki, K. Ikeda, H. Ishikawa, S. Namiki, and H. Kawashima, "Compact 2× 2 polarization-diversity si-wire switch," *Optics Express*, vol. 22, no. 24, pp. 29818–29826, 2014.

[101] H. Fukuda, K. Yamada, T. Tsuchizawa, T. Watanabe, H. Shinojima, and S. ichi Itabashi, "Silicon photonic circuit with polarization diversity," *Optics Express*, vol. 16, pp. 4872–4880, Mar 2008.

[102] K. Tanizawa, K. Suzuki, S. Suda, K. Ishii, J. Kurumida, G. Cong, T. Inoue, K. Ikeda, S. Namiki, and H. Kawashima, "Off-chip polarization-diversity 4 × 4 Si-wire optical switch with digital DGD compensation," *IEEE Photonics Technology Letters*, vol. 28, no. 4, pp. 457–460, 2015.

[103] K. Suzuki, K. Tanizawa, S. Suda, H. Matsuura, T. Inoue, K. Ikeda, S. Namiki, and H. Kawashima, "Silicon-photonics polarization-insensitive broadband strictly-non-blocking 8×8 blade switch," in *2017 Optical Fiber Communications Conference and Exhibition (OFC)*, pp. 1–3, IEEE, 2017.

[104] X. Wang and K. S. Chiang, "Polarization-insensitive mode-independent thermo-optic switch based on symmetric waveguide directional coupler," *Optics Express*, vol. 27, no. 24, pp. 35385–35393, 2019.

[105] W. Liang, W. Chen, P. Wang, S. Dai, B. Zhang, Y. Zhou, J. Li, Y. Li, Q. Fu, and T. Dai, "Non-volatile polarization-insensitive $1\times$ 2 silicon optical switch using phase-change materials," *Optics Communications*, vol. 479, p. 126407, 2021.

[106] S. Han, T. J. Seok, K. Yu, N. Quack, R. S. Muller, and M. C. Wu, "50x50 polarization-insensitive silicon photonic mems switches: design and experiment," in *ECOC 2016-Post Deadline Paper; 42nd European Conference on Optical Communication*, pp. 1–3, VDE, 2016.

[107] J. Du, W. Shen, J. Liu, Y. Chen, X. Chen, and Z. He, "Mode division multiplexing: from photonic integration to optical fiber transmission," *Chinese Optics Letters*, vol. 19, no. 9, p. 091301, 2021.

[108] X. Han, Y. Jiang, A. Frigg, H. Xiao, P. Zhang, T. G. Nguyen, A. Boes, J. Yang, G. Ren, and Y. Su, "Mode and polarization-division multiplexing based on silicon nitride loaded lithium niobate on insulator platform," *Laser & Photonics Reviews*, vol. 16, no. 1, p. 2100529, 2022.

[109] W. Jiang, J. Miao, and T. Li, "Compact silicon 10-mode multi/demultiplexer for hybrid mode-and polarisation-division multiplexing system," *Scientific Reports*, vol. 9, no. 1, pp. 1–15, 2019.

[110] Y. Zhang, R. Zhang, Q. Zhu, Y. Yuan, and Y. Su, "Architecture and devices for silicon photonic switching in wavelength, polarization and mode," *Journal of Lightwave Technology*, vol. 38, no. 2, pp. 215–225, 2020.

[111] C. Sun, Y. Yu, and X. Zhang, "Ultra-compact waveguide crossing for a mode-division multiplexing optical network," *Optics letters*, vol. 42, no. 23, pp. 4913–4916, 2017.

[112] W. Chang, L. Lu, X. Ren, D. Li, Z. Pan, M. Cheng, D. Liu, and M. Zhang, "Ultra-compact mode (de) multiplexer based on subwavelength asymmetric y-junction," *Optics express*, vol. 26, no. 7, pp. 8162–8170, 2018.

[113] S. Wu, X. Mu, L. Cheng, S. Mao, and H. Fu, "State-of-the-art and perspectives on silicon waveguide crossings: A review," *Micromachines*, vol. 11, no. 3, p. 326, 2020.

[114] P. Sun and R. M. Reano, "Submilliwatt thermo-optic switches using free-standing silicon-on-insulator strip waveguides," *Optics express*, vol. 18, no. 8, pp. 8406–8411, 2010.

[115] H. Qiu, Y. Liu, C. Luan, D. Kong, X. Guan, Y. Ding, and H. Hu, "Energy-efficient thermo-optic silicon phase shifter with well-balanced overall performance," *Optics Letters*, vol. 45, no. 17, pp. 4806–4809, 2020.

[116] M. Jacques, A. Samani, E. El-Fiky, D. Patel, Z. Xing, and D. V. Plant, "Optimization of thermo-optic phase-shifter design and mitigation of thermal crosstalk on the soi platform," *Optics express*, vol. 27, no. 8, pp. 10456–10471, 2019.

[117] G. Zhang, H. R. Mojaver, A. Das, and O. Liboiron-Ladouceur, "Mode insensitive switch for on-chip interconnect mode division multiplexing systems," *Optics Letters*, vol. 45, no. 4, pp. 811–814, 2020.

[118] S. Molesky, Z. Lin, A. Y. Piggott, W. Jin, J. Vucković, and A. W. Rodriguez, "Inverse design in nanophotonics," *Nature Photonics*, vol. 12, no. 11, pp. 659–670, 2018.

[119] K. Suzuki, T. Yamada, O. Moriwaki, H. Takahashi, and M. Okuno, "Polarization-insensitive mzi switch composed of an ln phase shifter array and silica-based plc-integrated polarization beam splitter," in *Optical Fiber Communication Conference*, p. OWI7, Optica Publishing Group, 2008.

[120] K. H. R. Mojaver, G. Zhang, and O. Liboiron-Ladouceur, "Design of silicon photonic mode-sensitive thermo-optic phase shifter based on subwavelength grating structures," in *2022 IEEE Photonics Conference (IPC)*, pp. 1–2, IEEE, 2022.

[121] W. Li, L. Xu, J. Zhang, D. Mao, Y. D'Mello, Z. Wei, and D. V. Plant, "Broadband polarization-insensitive thermo-optic switches on a 220-nm silicon-on-insulator platform," *IEEE Photonics Journal*, 2022.

[122] R. Imansyah, T. Tanaka, L. Himbele, H. Jiang, and K. Hamamoto, "Electrically controlled optical-mode switch for fundamental mode and first order mode," *Japanese Journal of Applied Physics*, vol. 55, no. 8S3, p. 08RB06, 2016.

[123] Y. Xiong, R. B. Priti, and O. Liboiron-Ladouceur, "High-speed two-mode switch for mode-division multiplexing optical networks," *Optica*, vol. 4, no. 9, pp. 1098–1102, 2017.

[124] T. A. Ramadan and R. M. Osgood, "Adiabatic couplers: design rules and optimization," *Journal of Lightwave Technology*, vol. 16, no. 2, p. 277, 1998.

[125] T. Van Vaerenbergh, S. Hooten, M. Jain, P. Sun, Q. Wilmart, A. Seyedi, Z. Huang, M. Fiorentino, and R. Beausoleil, "Wafer-level testing of inverse-designed and adjoint-inspired dual layer si-sin vertical grating couplers," *Journal of Physics: Photonics*, vol. 4, no. 4, p. 044001, 2022.

[126] Y. Wang, X. Wang, J. Flueckiger, H. Yun, W. Shi, R. Bojko, N. A. Jaeger, and L. Chrostowski, "Focusing sub-wavelength grating couplers with low back reflections for rapid prototyping of silicon photonic circuits," *Optics express*, vol. 22, no. 17, pp. 20652–20662, 2014.

[127] A. Das, H. R. Mojaver, G. Zhang, and O. Liboiron-Ladouceur, "Scalable siph-inp hybrid switch based on low-loss building blocks for lossless operation," *IEEE Photonics Technology Letters*, vol. 32, no. 21, pp. 1401–1404, 2020.

[128] G. Zhang, D.-X. Xu, Y. Grinberg, and O. Liboiron-Ladouceur, “Compact, broadband cwdm demultiplexer using energy constrained inverse design,” in *2022 Conference on Lasers and Electro-Optics (CLEO)*, pp. 1–2, IEEE, 2022.

[129] H. Xie, Y. Liu, W. Li, J. Du, Y. Yao, Q. Song, and K. Xu, “Demonstration of an ultra-compact bend for four modes based on pixelated meta-structure,” in *2020 Optical Fiber Communications Conference and Exhibition (OFC)*, pp. 1–3, IEEE, 2020.

[130] W. Chang, X. Ren, Y. Ao, L. Lu, M. Cheng, L. Deng, D. Liu, and M. Zhang, “Inverse design and demonstration of an ultracompact broadband dual-mode 3-db power splitter,” *Optics Express*, vol. 26, no. 18, pp. 24135–24144, 2018.

[131] G. Zhang and O. Liboiron-Ladouceur, “Scalable and low crosstalk silicon mode exchanger for mode division multiplexing system enabled by inverse design,” *IEEE Photonics Journal*, vol. 13, no. 2, pp. 1–13, 2021.

[132] G. Zhang, D.-X. Xu, Y. Grinberg, and O. Liboiron-Ladouceur, “Topological inverse design of nanophotonic devices with energy constraint,” *Optics Express*, vol. 29, no. 8, pp. 12681–12695, 2021.

[133] N. Yang and J. Xiao, “A compact silicon-based polarization-independent power splitter using a three-guide directional coupler with subwavelength gratings,” *Optics Communications*, vol. 459, p. 125095, 2020.

[134] Y. Lai, Y. Yu, S. Fu, J. Xu, P. P. Shum, and X. Zhang, “Compact double-part grating coupler for higher-order mode coupling,” *Optics Letters*, vol. 43, no. 13, pp. 3172–3175, 2018.

[135] D. Melati, A. Alippi, A. Annoni, N. Peserico, and A. Melloni, “Integrated all-optical mimo demultiplexer for mode-and wavelength-division-multiplexed transmission,” *Optics Letters*, vol. 42, no. 2, pp. 342–345, 2017.

[136] A. Mohanty, M. Zhang, A. Dutt, S. Ramelow, P. Nussenzveig, and M. Lipson, “Quantum interference between transverse spatial waveguide modes,” *Nature Communications*, vol. 8, no. 1, pp. 1–7, 2017.

[137] L.-T. Feng, M. Zhang, X. Xiong, Y. Chen, H. Wu, M. Li, G.-P. Guo, G.-C. Guo, D.-X. Dai, and X.-F. Ren, “On-chip transverse-mode entangled photon pair source,” *Npj Quantum Information*, vol. 5, no. 1, pp. 1–7, 2019.